

**Search for Higgs Boson Pair Production
in the $hh \rightarrow b\bar{b}\tau^+\tau^-$ Channel
with the ATLAS Detector**

Ryosuke FUCHI

February 2016

**Search for Higgs Boson Pair Production
in the $hh \rightarrow b\bar{b}\tau^+\tau^-$ Channel
with the ATLAS Detector**

**Ryosuke FUCHI
Doctoral Program in Physics**

**Submitted to the Graduate School of
Pure and Applied Sciences
in Partial Fulfillment of the Requirements
for the Degree of Doctor of Philosophy in Science
at the
University of Tsukuba**

Abstract

We have searched for higgs boson pair production in proton-proton collisions in the $hh \rightarrow b\bar{b}\tau^+\tau^-$ decay channel with the ATLAS detector at the CERN Large Hadron Collider. We have analyzed proton-proton collision data corresponding to an integrated luminosity of 20.3 fb^{-1} at a center-of-mass energy of 8 TeV. The search is intended to examine possible hh production enhancement predicted in some of the Beyond-the-Standard-Model scenarios, but also is motivated to develop an analysis method applicable to future measurements of the higgs boson self-couplings predicted in the Standard Model (SM). As hh production mechanisms, we consider both the non-resonant case, where hh pairs are produced through the SM processes, and the resonant case, where a heavy higgs boson H decays into a hh pair, $H \rightarrow hh$. The final state objects $b\bar{b}\tau^+\tau^-$ are identified by requiring one or two b -tagged jets for b -quarks, and a pair of a lepton (= electron or muon) and a hadronic jet, consistent with leptonic and hadronic decays of a $\tau^+\tau^-$ pair. The invariant mass distributions of $m_{\tau^+\tau^-}$ and $m_{b\bar{b}\tau^+\tau^-}$ have been used as the final discriminants for non-resonant and resonant searches, respectively. No excesses over the expected backgrounds have been observed. We thus set a 95% CL upper limit on the non-resonant hh production cross section to be 1.60 pb with an expected sensitivity of 1.31 pb. Also, 95% CL upper limits on the resonant production cross section are placed, ranging from 4.2 pb for $m_H = 260 \text{ GeV}/c^2$ to 0.46 pb for $m_H = 1000 \text{ GeV}/c^2$.

Acknowledgments

I would like to thank everyone who has supported and encouraged me during my Ph.D program. I express my sincere gratitude to the all staff members of University of Tsukuba, in particular:

To Professor Fumihiko Ukegawa, who supervised and led me the correct way over five years, including my Master 's program. I will continue to use what I have learned from him in my future life.

To Professor Shinhong Kim, who always gave me so much precious advice in my studies and supported my research life.

To Kazuhiko Hara, who supported me, not only in my studies, but also all of my life. He encouraged me and gave me advice when I needed it.

To Yuji Takeuchi, Koji Sato, Hideki Okawa and Kenichi Takemasa who gave me much advice in my studies.

I would like to express my gratitude to Keita Hanawa, who is a researcher at University of Tokyo. This work would not have been possible without his help. I spent lots of time with him not only discussions of the research, but also socially. Also, my appreciation goes to his wife Mariko and their son, Motochika. They were close to my family and supported my life in France and Switzerland.

I am very grateful to all of members of Higgs pair production analysis group; Jahres Adelman, Andrew Daniells, Yaquan Fang, Jianming Qian, James Saxon, Xiaohu Sun, David Robert, Huijun Zhang and Nikolaos Konstantidis, Katharine Leney, Aleandro Nisati, Erez Etzion and Carl Bryan. My discussions with them and their advice were very important in my research.

I extend my appreciation to all of members in High Energy Physics Laboratory at University of Tsukuba. I discussed my studies and spent precious time with Kenji Kiuchi, Kazuki Nagata, Fumiaki Ito, Kota Kasahara, Shunsuke Honda and Mutsuto Hagihara in not only Tsukuba but also CERN. Also, thanks to my office colleagues Ren Senzaki, Koya Moriuchi, Mari Asano, Daisuke Sekigawa and Shunsuke Yagi.

I would like to thank all of the people that I met in CERN.

Soshi Tsuno supported me during my work on Tau Working Group.

My wife and I spent all the time, including holidays, in France and Switzerland with Naoki Kimura, Yuki Sakurai, Takashi Mitani, Tomoya Messi Iizawa and Toshiaki Kaji, and together we shared both the tough and fun times. I owe what I am to them.

Kazuya Mochiduki supported and encouraged me.

My office colleague, Stefan Guindon, always encouraged me with his best smile.

I express my thanks to Jeremie Bride and his warm family. They always supported me during my life in France.

I extend my appreciation to my close family, my father, my mother and my sister. Their support

always helped me. I cannot thank them enough.

Finally, I am so grateful to my wife, Midori. We shared not only the fun things, but also many tough things together. I cannot thank her enough and also extend my gratitude to her family for giving me so much support, too.

Contents

1	Introduction	1
1.1	The Higgs Boson	1
1.1.1	Electroweak Interactions	1
1.1.2	Discovery of Higgs Boson	5
1.2	Higgs Boson Pair Production	10
1.3	$hh \rightarrow b\bar{b}\tau^+\tau^-$ Final State	14
1.3.1	Advantages in $hh \rightarrow b\bar{b}\tau^+\tau^-$ Channel	14
1.3.2	Signature of τ Decay	15
2	LHC Accelerator and ATLAS Detector	17
2.1	The Large Hadron Collider	17
2.1.1	Proton Injection to The LHC	17
2.1.2	The LHC Parameters	18
2.2	The ATLAS Detector	18
2.2.1	The Inner Detectors	19
2.2.2	The Calorimeters	20
2.2.3	Muon Spectrometer	22
2.2.4	The Magnets	24
2.3	Trigger and Data Acquisition System	24
2.3.1	Lepton Triggers	24
3	Signal and Background Processes	29
3.1	Signal Processes	29
3.2	Background Processes	29
3.2.1	Single SM Higgs Production	29
3.2.2	Top Pair Production	30
3.2.3	Single-top Production	30
3.2.4	$Z^0 \rightarrow \tau^+\tau^- + \text{jets}$ Production	30
3.2.5	$Z^0 \rightarrow e^+e^-/\mu^+\mu^- + \text{jets}$ Production	30
3.2.6	Di-boson Production	30
3.2.7	$W(\rightarrow e\nu/\mu\nu) + \text{jets}$ Production	30
3.2.8	QCD-jet Production	31
4	Monte Carlo Simulation Samples and ATLAS Data	33
4.1	ATLAS Data	33
4.2	Monte Carlo Samples	33
4.2.1	Signal Samples	33
4.2.2	Background Samples	33
4.3	Sample for $Z^0 \rightarrow \tau^+\tau^-$ Estimation	34
4.3.1	$Z\mu^+\mu^-$ Event Selection	34

5	Object Reconstruction and Identification	37
5.1	Electron	37
5.1.1	Reconstruction	37
5.1.2	Identification	38
5.1.3	Energy Scale and Resolution	38
5.1.4	Object Selection	38
5.2	Muon	41
5.2.1	Reconstruction and Identification	41
5.2.2	Momentum Scale and Resolution	41
5.2.3	Object Selection	41
5.3	Jet	45
5.3.1	Reconstruction	45
5.3.2	Energy Scale and Resolution	46
5.3.3	b -Jets Identification	48
5.3.4	Object Selection	49
5.4	Tau	52
5.4.1	Leptonic Decay Tau	52
5.4.2	Hadronic Decay Tau	52
5.5	Missing Transverse Momentum	55
5.6	Object Assignment	55
5.7	Higgs Boson	56
5.7.1	$h \rightarrow b\bar{b}$ Reconstruction	56
5.7.2	$h \rightarrow \tau^+\tau^-$ Reconstruction	56
5.8	$b\bar{b}\tau^+\tau^-$ Reconstruction	58
6	Event Reconstruction and Selection	61
6.1	Event Pre-Selection	61
6.2	Analysis Categorization	70
6.3	Event Selection for Background Suppression	71
7	Background Estimation	77
7.1	Overview of The Methods	77
7.2	Fake Factor Method	77
7.2.1	Fake Factor Method	77
7.2.2	Control Region Definitions	78
7.2.3	Combined Fake Factor	79
7.2.4	Method Validation	80
7.3	Top Background	83
7.4	$Z^0 \rightarrow \tau^+\tau^-$ Background	85
7.5	Diboson and $Z^0 \rightarrow e^+e^-$ or $\mu^+\mu^-$ Background	85
7.6	The Events in Signal Region	85
8	Systematic Uncertainties	89
8.1	Theoretical Systematic Uncertainties	89
8.2	Experimental Systematic Uncertainties	90
8.2.1	Electron	90
8.2.2	Muon	90
8.2.3	Hadronic- τ	90
8.2.4	Jet	91
8.2.5	Missing Transverse Energy	92
8.2.6	Trigger	92

8.2.7	Luminosity	92
8.2.8	Fake Background	92
8.2.9	Estimation of $Z^0 \rightarrow \tau^+\tau^-$ +jets with Embedding Method	93
8.2.10	Estimation of Top Background	93
9	Results	95
9.1	Fit Method for The Background and Signal	95
9.2	Result of Non-Resonant Analysis	96
9.3	Result of Resonant Analysis	97
10	Combination with Other Analysis Channels	101
10.1	Result of Non-Resonant Analysis	101
10.2	Result of Resonant Analysis	101
11	Conclusions	105
A	Tau Identification Variables	107
B	$t\bar{t}$ Contamination in Embedding Sample	109
C	Other Analyses	113
C.1	$hh \rightarrow b\bar{b}\gamma\gamma$ analysis	113
C.2	$hh \rightarrow b\bar{b}b\bar{b}$ analysis	115
C.3	$hh \rightarrow WW\gamma\gamma$ analysis	117

List of Figures

1.1	Potential $V(\phi)$ in case of (a) before and (b) after symmetry breaking.	4
1.2	(a) $\gamma\gamma$ mass distribution of $h \rightarrow \gamma\gamma$ channel. (b) The local p_0 value for the $h \rightarrow ZZ^* \rightarrow 4l$, $h \rightarrow \gamma\gamma$ and $h \rightarrow WW^* \rightarrow e\nu\mu\nu$ channels combined. The SM Higgs boson mass hypothesis of $m_H = 126.5$ GeV is used. The data statistics is corresponding to $4.6-4.8 \text{ fb}^{-1}$ and $5.8-5.9 \text{ fb}^{-1}$ at $\sqrt{s} = 7$ and 8 TeV, respectively. The observed (solid) local p_0 as a function of m_H in the low mass range. The dashed curve shows the expected local p_0 under the hypothesis of a SM Higgs boson signal at that mass with its $\pm 1\sigma$ band. The horizontal dashed lines indicate the p -values corresponding to significance of 1 to 6σ . [1]	6
1.3	(a) The mass of di-tau system reconstructed by MMC described in Section 5.7.2 for the MVA based analysis and, all lep-lep, lep-had and had-had channels are combined by weighted by $\ln(1 + S/B)$. (b) Observed (solid red) and expected (dashed red) p_0 values for a given m_h . All channels are combined in the cut-based analysis (CBA). The expected p_0 values are given for the background-only hypothesis. The corresponding observed and expected p_0 values for the multivariate analysis (MVA) are indicated for $m_H = 125$ GeV by a full and open star respectively. [4]	7
1.4	The result from $h \rightarrow b\bar{b}$ analysis. Observed (solid) and expected (dashed) 95% CL cross-section upper limits normalized to the SM higgs boson production cross section for given mass m_h with full data set collected in 2011 and 2012 and including all analysis channels.	7
1.5	The observed signal strengths normalized by the SM prediction and uncertainties for different Higgs boson decay channels and their combination for $m_h = 125.36$ GeV.	8
1.6	Observed and expected limits for alternative spin-parity hypotheses assuming a $J^P = 0^+$ signal are shown with the black and blue points, respectively.	9
1.7	Higgs boson trilinear-self-coupling.	10
1.8	Some generic Feynman diagrams contributing to Higgs pair production at hadron colliders. [12] The capital "H" stands for standard model higgs in these diagrams.	11
1.9	The ratio of the cross sections compared with standard model at a given $\frac{\lambda_{hhh}}{\lambda_{SM}^{hhh}}$ at $\sqrt{s} = 8$ TeV. [12]	12
1.10	di-higgs production cross sections in femt barn given at a given $\frac{\lambda_{hhh}}{\lambda_{SM}^{hhh}}$ at $\sqrt{s} = 14$ TeV. [12]	12
1.11	The cross sections times branching ratio of 2HDM heavy scalar higgs in units of picobarn for $\sqrt{s} = 8$ TeV pp collision for given mass. The configurations are, Upper left: $\tan\beta = 1$, $\cos(\beta - \alpha) = -0.32$ = for Type 1 2HDM. Upper right: $\tan\beta = 1$, $\cos(\beta - \alpha) = -0.11$ for Type 2 2HDM. Lower left: $\tan\beta = 10$, $\cos(\beta - \alpha) = -0.43$ for Type 1 2HDM. Lower right: $\tan\beta = 10$, $\cos(\beta - \alpha) = -0.02$ for Type 2 2HDM, where α represents the mixing of h and H [15].	13
1.12	The feynman diagrams of tau lepton decay (a) leptonically and (b) hadronically.	15
2.1	The proton injection to the LHC. [18]	18
2.2	The ATLAS Detector.	19

2.3	Illustration of Inner Detector. It is composed of PIXEL, SCT and TRT [19].	20
2.4	Calorimeters	21
2.5	The illustration of LAr EM calorimeter. [20]	22
2.6	Muon spectrometer.	23
2.7	The layout of the magnet system. [22]	24
2.8	Illustration of the trigger system. [33]	25
2.9	The calorimeter trigger tower. [58]	26
2.10	A schematic picture showing a quarter-section of the muon system. [59]	27
3.1	di-higgs production of leading order for non-resonant production, (a) self-coupling and (b) Yukawa coupling.	29
5.1	Electron identification efficiencies for each working point [38], calculated as function of (a) electron E_T , (b) electron η , and (c) number of event vertices. The data (full mars) and MC (open marks) are compared.	39
5.2	The invariant mass distribution $m_{e^+e^-}$ in $Z^0 \rightarrow e^+e^-$ events, compared to MC templates. The templates of $m_{e^+e^-}$ for different, (a) α values, and (c) c values. The χ^2 distributions as a function of, (b) α , and (d) c	40
5.3	Top: Invariant mass distribution of di-electron in $Z^0 \rightarrow e^+e^-$. Calibrated data (blue point), uncorrected MC (dashed black line), and MC (solid black line) are shown. Bottom: Ratio of the "data/MC" and "uncorrected MC/MC" [39].	40
5.4	Muon reconstruction by (a) Combined, (b) Segment-Tagged, (c) Stand-Alone, and (d) Calorimeter Tagged Muons.	42
5.5	Efficiency of CB muon, measured with tag-and-probe method using $Z^0 \rightarrow \mu^+\mu^-$ events, as a function of pseudorapidity [40].	43
5.6	Resonant mass of $Z^0 \rightarrow \mu^+\mu^-$ reconstructed with Combined Muon. [41]	43
5.7	Ratio data/MC of the fitted mean mass $\langle m_{\mu^+\mu^-} \rangle$ in (Top) $Z^0 \rightarrow \mu^+\mu^-$, (Middle) $\Upsilon \rightarrow \mu^+\mu^-$, and (Bottom) $J\psi \rightarrow \mu^+\mu^-$. [41]	44
5.8	Dimuon invariant mass resolution for CB muons for $Z^0 \rightarrow \mu^+\mu^-$ as a function of leading muon η . [41]	44
5.9	Reconstructed cluster with topological clustering. (left) starting from a seed (= $7\sigma_{\text{noise}}$), all neighbors with ($> 2\sigma$) and their adjacent cells are added. Finally cells with yellow colored construct a cluster. (right) No cluster is constructed for the seed $>4\sigma$	45
5.10	The jet reconstructions with (a) k_T , (b)Cambridge/Aachen and (c)anti- k_T are shown for the parton-level event generated with 10^4 soft "ghosts". [44]	47
5.11	The scheme of calibration of the LCW jet. [46]	48
5.12	Energy response as a function of η for LCW scale. [46]	48
5.13	The energy response after applying JES calibration as a function of jet (a) p_T and (b) η [46].	49
5.14	The relative jet response as a function of η [46]. The black solid line shows the derived intercalibration factors.	50
5.15	The ratio of response for Z^0 +jet, γ +jet and multi-jet balance studies [46].	51
5.16	Illustration of bottom quark decay [73].	51
5.17	Signal and background distribution of (a) f_{cent} for 1-prong, (b) N_{track}^{iso} for 1-prong, (c) R_{track} for 3-prong and (d) $m_{\Pi^0+track}$ for 3-prong. These variables are input into the tau identification BDT algorithm. [42]	53
5.18	The tau identification efficiencies for (a)1-prong and (b)3-prong. [42]	54
5.19	The tau energy response curves as a given E_{LC}^T for (a)1-prong and (b)3-prong. [42]	55

5.20	bb mass distribution for $m_H = 300$ GeV resonant sample. The black and red lines correspond to one and two b -tagged category, respectively. The merged one is shown with green line. The blue line stands for the bb mass reconstructed from correct two b -jets by using truth information.	56
5.21	Example of the probability distributions as a function of $\Delta\theta_{3D}$ and τ momenta for (a) 1-prong hadronic decay (b) 3-prong hadronic decay (c) leptonic decay.	57
5.22	$\tau^+\tau^-$ mass distribution reconstructed by MMC for $Z^0 \rightarrow \tau^+\tau^-$, $h \rightarrow \tau^+\tau^-$ and $H \rightarrow b\bar{b}\tau^+\tau^-$ at 300 GeV resonant.	58
5.23	The $m_{b\bar{b}\tau^+\tau^-}$ distributions reconstructed by three ways.	59
6.1	Distributions of (a) transverse momentum of τ_{had} , (b) transverse momentum of electron, (c) Missing Energy, and (d) transverse mass of electron and E_T^{miss} in the electron+ τ_{had} channel in the pre-selection level. The data yields well agree on the background model. The shade area shows the statistical and systematical errors combined of the background modeling.	62
6.2	Distributions of (a) number of jets, (b) number of b -jets, (c) transverse momentum of leading jet, and (d) transverse momentum of sun-leading jet in the electron+ τ_{had} channel in the pre-selection level. The data yields well agree on the background model. The shade area shows the statistical and systematical errors combined of the background modeling.	63
6.3	Distributions of (a) invariant mass of two b -jets $m_{b\bar{b}}$, (b) transverse momentum of di-tau system, (c) invariant mass of electron and τ_{had} . $m_{\tau^+\tau^-}$ reconstructed by MMC, and (d) invariant mass of two b -jets and electron and τ_{had} . $m_{b\bar{b}\tau^+\tau^-}$ in the electron+ τ_{had} channel in the pre-selection level. The data yields well agree on the background model. The shade area shows the statistical and systematical errors combined of the background modeling.	64
6.4	Distributions of (a) E_T^ϕ centrality, (b) Δp_T of electron and τ_{had} (c) invariant mass of τ_{had} and additional jet, and (d) invariant mass of τ_{had} . additional jet and b -jet in the electron+ τ_{had} channel in the pre-selection level. The data yields well agree on the background model. The shade area shows the statistical and systematical errors combined of the background modeling.	65
6.5	Distributions of (a) transverse momentum of τ_{had} , (b) transverse momentum of muon, (c) Missing Energy, and (d) transverse mass of muon and E_T^{miss} in the muon+ τ_{had} channel in the pre-selection level. The data yields well agree on the background model. The shade area shows the statistical and systematical errors combined of the background modeling.	66
6.6	Distributions of (a) number of jets, (b) number of b -jets, (c) transverse momentum of leading jet, and (d) transverse momentum of sun-leading jet in the muon+ τ_{had} channel in the pre-selection level. The data yields well agree on the background model. The shade area shows the statistical and systematical errors combined of the background modeling.	67
6.7	Distributions of (a) invariant mass of two b -jets $m_{b\bar{b}}$, (b) transverse momentum of di-tau system, (c) invariant mass of muon and τ_{had} . $m_{\tau^+\tau^-}$ reconstructed by MMC, and (d) invariant mass of two b -jets and muon and τ_{had} . $m_{b\bar{b}\tau^+\tau^-}$ in the muon+ τ_{had} channel in the pre-selection level. The data yields well agree on the background model. The shade area shows the statistical and systematical errors combined of the background modeling.	68

6.8	Distributions of (a) E_T^ϕ centrality, (b) Δp_T of muon and τ_{had} (c) invariant mass of τ_{had} and additional jet, and (d) invariant mass of τ_{had} , additional jet and b -jet in the muon+ τ_{had} channel in the pre-selection level. The data yields well agree on the background model. The shade area shows the statistical and systematical errors combined of the background modeling.	69
6.9	Number of events as function of p_T of di-tau system (a) 1 b -tagged and (b) 2 b -tagged categories.	71
6.10	MET ϕ centrality distribution of $m_H = 300$ GeV signal(red) and W^\pm +jets(blue).	73
6.11	$m_{\tau_{\text{jet}}}$ vs $m_{\tau_{\text{jet}}, b\text{-jet}}$ in 2D plane for (a) $t\bar{t}$ background and (b) 300 GeV signal.	74
6.12	$\Delta p_T(l, \tau_{\text{had}})$ distribution in 10 GeV bin for resonant signal of $m_H = 260$ GeV (red) and $t\bar{t}$ background (blue).	74
7.1	Fraction of partons in jet events as function of tau selection criteria.	78
7.2	Fake factors for various processes for (a) 1 prong and (b) 3 prong.	79
7.3	Kinematics distributions of (a) transverse momentum of τ_{had} , (b) transverse momentum of di-tau system, (c) invariant mass $m_{\tau^+\tau^-}$ reconstructed by MMC, and (d) invariant mass $m_{b\bar{b}\tau^+\tau^-}$ in same sign events for one b -tagged category. Background model enhanced fake background well agrees with same sign data. The shaded area indicates statistical and systematic uncertainty which includes ones of b -tag and fake estimation.	81
7.4	Kinematics distributions of (a) transverse momentum of τ_{had} , (b) transverse momentum of di-tau system, (c) invariant mass $m_{\tau^+\tau^-}$ reconstructed by MMC, and (d) invariant mass $m_{b\bar{b}\tau^+\tau^-}$ in same sign events for two b -tagged category. Background model enhanced fake background in same sign well agrees data. The shaded area indicates statistical and systematic uncertainty which includes ones of b -tag and fake estimation.	82
7.5	Kinematics distributions of (a) transverse momentum of transverse momentum of τ_{had} . (b) transverse momentum of di-tau system, (c) invariant mass $m_{\tau^+\tau^-}$ reconstructed by MMC, and (d) invariant mass $m_{b\bar{b}\tau^+\tau^-}$ in top control region. Background model enhanced $t\bar{t}$ background in same sign well agrees data.	84
7.6	The $m_{\tau^+\tau^-}$ distribution reconstructed from MMC method after the non-resonant search selections in each of categories, (a) one b -tagged and $p_T^{\tau^+\tau^-} < 100$ GeV, (b) one b -tagged and $p_T^{\tau^+\tau^-} > 100$ GeV, (c) two b -tagged and $p_T^{\tau^+\tau^-} < 100$ GeV, and (d) two b -tagged and $p_T^{\tau^+\tau^-} > 100$ GeV.	87
7.7	The $m_{b\bar{b}\tau^+\tau^-}$ distribution reconstructed from constrained mass method after the resonant search selections in each of categories, (a) one b -tagged and $p_T^{\tau^+\tau^-} < 100$ GeV, (b) one b -tagged and $p_T^{\tau^+\tau^-} > 100$ GeV, (c) two b -tagged and $p_T^{\tau^+\tau^-} < 100$ GeV, and (d) two b -tagged and $p_T^{\tau^+\tau^-} > 100$ GeV.	88
8.1	Uncertainties on the JES as a function of the jet $ \eta $ in $p_T = 35$ GeV [49].	91
8.2	Relative jet response $1/c$ as a function of jet η in the p_T slice from 25 GeV to 40 GeV [49].	92
9.1	Observed (solid line) and expected (dashed line) 95% CL limits as a function of resonant mass for category combination. Green and yellow bands represent the ± 1 and 2σ deviation.	98
9.2	Observed (solid line) and expected (dashed line) local significance, p_0 , as a function of resonant mass for category combination, assuming signal cross section is 1 pb.	99
10.1	The observed and expected 95% CL upper limits on $\sigma(gg \rightarrow H) \times BR(H \rightarrow hh)$. $hh \rightarrow b\bar{b}\tau^+\tau^-, \gamma\gamma WW, \gamma\gamma b\bar{b}, b\bar{b}b\bar{b}$ are combined.	103

10.2	(a) hMSSM scenario and (b) low-tb-high scenario. [67]	103
B.1	Top two plots show embedding(blue) and $t\bar{t}$ contamination(black) in resonant mass distribution of two b-tagged jet category for resonant search. Bottom plot shows embedding(blue) and $t\bar{t}$ contamination(black) in MMC distribution of two b-tagged jet category for non-resonant search.	111
C.1	Left: Invariant mass of diphoton $m_{\gamma\gamma}$ for non-resonant search (Upper) signal region, and (Lower) fewer than two b tags control region. The fitted curve is also used in the upper plot. Right: Invariant mass $m_{b\bar{b}\gamma\gamma}$ for resonant search (Upper) signal region, and (Lower) fewer than two b tags control region. The fitted curve is also used in the upper plot. [68].	114
C.2	The 95% CL upper limits for resonant production cross section times branching ratio of hh . [68]	114
C.3	Resolved analysis: Invariant masses of two dijet system in 2D plane (a), and four jets m_{4j} (b). Boosted analysis: Invariant masses of two fat jets in 2D plane (c), and two fat jets m_{2J} (d).	116
C.4	The 95% CL upper limits for resonant production cross section times branching ratio of hh . [69]	117
C.5	The invariant mass of diphoton in the signal region. [67].	118
C.6	The 95% CL upper limits for resonant production cross section times branching ratio of hh [67].	118

List of Tables

1.1	The total Higgs pair production cross section in the main channels at the LHC (in fb) for given c.m. energies(in TeV) with $M_H = 125$ GeV. [12]	10
1.2	The branching ratios of di-higgs decay combinations $hh \rightarrow XXY$ in percent are shown. $hh \rightarrow b\bar{b}\tau^+\tau^-$ has the third largest branching ratio 7.1 % which is shown in bold.	14
1.3	The branching ratio of $\tau^+\tau^-$	15
2.1	The beam parameters for pp collision in LHC 2012 Run.	18
2.2	The coverage and total thickness of EM calorimeter.	21
2.3	The hadronic-calorimeter.	22
2.4	The single lepton trigger used for the 2012 data analysis.	25
4.1	List of MC generators and parton distribution functions used for the signal and background processes. The light Higgs boson h is assumed to have a mass of 125.36 GeV.	34
5.1	The variables performed as a input of the BDT to reject the jets.	52
6.1	Efficiencies of pre-selections evaluated for different $H \rightarrow hh$ masses for 260 to 1000 GeV.	61
6.2	Signal and background yields per 20.3 fb^{-1} at $\sqrt{s} = 8$ TeV.	70
6.3	Analysis categories.	70
6.4	Signal deficiencies for all selections for OneB and Low $p_T^{\tau^+\tau^-}$ category for non-resonant and various resonant masses from 260 to 1000 GeV.	73
6.5	Signal deficiencies for all selections for OneB and High $p_T^{\tau^+\tau^-}$ category for non-resonant and various resonant masses from 260 to 1000 GeV.	73
6.6	Signal deficiencies for all selections for TwoB and High $p_T^{\tau^+\tau^-}$ category for non-resonant and various resonant masses from 260 to 1000 GeV.	75
6.7	Signal deficiencies for all selections for TwoB and Low $p_T^{\tau^+\tau^-}$ category for non-resonant and various resonant masses from 260 to 1000 GeV.	75
6.8	The numbers of events passing event selections per 20.3 fb^{-1} at $\sqrt{s} = 8$ TeV.	75
7.1	Fraction of the different processes contributing to the fake background.	80
7.2	Number of events in the OneB category of the $e\tau_h$ and $\mu\tau_h$ channels combined for non-resonant search, assuming signal cross section of 1 pb. Various background processes are estimated with the methods described in Section 7. Both statistical (first number) and systematic (second number) uncertainties are given.	85
7.3	Number of events in the TwoB category of the $e\tau_h$ and $\mu\tau_h$ channels combined for non-resonant search, assuming signal cross section of 1 pb. Various background processes are estimated with the methods described in Section 7. Both statistical (first number) and systematic (second number) uncertainties are given.	86

7.4	Number of events in the OneB category of the $e\tau_h$ and $\mu\tau_h$ channels combined for resonant search, assuming signal cross section of 1 pb. Various background processes are estimated with the methods described in Section 7. Both statistical (first number) and systematic (second number) uncertainties are given.	86
7.5	Number of events in the TwoB category of the $e\tau_h$ and $\mu\tau_h$ channels combined for resonant search, assuming signal cross section of 1 pb. Various background processes are estimated with the methods described in Section 7. Both statistical (first number) and systematic (second number) uncertainties are given.	86
8.1	Summary of theory uncertainties for the background process normalizations.	89
8.2	The uncertainty for fake background.	92
9.1	Observed and expected 95% confidence level upper limits (UL) for non-resonant search.	96
9.2	Observed and expected local significance, p_0 , in non-resonant search, for each categories, assuming signal cross section is 1 pb.	96
9.3	The effect of the most important sources of uncertainty on the signal strength parameter, for the non-resonant signal.	97
9.4	Observed and expected 95% confidence level upper limits (UL) for each mass point for the 1b-tag and 2-btag combined.	97
9.5	Observed and expected local significance, p_0 , for each mass point for the combination, assuming signal cross section is 1 pb.	98
9.6	The effect of the most important sources of uncertainty on the signal strength parameter, for the resonant 260 GeV signal.	100
9.7	The effect of the most important sources of uncertainty on the signal strength parameter, for the resonant 400 GeV signal.	100
9.8	The effect of the most important sources of uncertainty on the signal strength parameter, for the resonant 500 GeV signal.	100
9.9	The effect of the most important sources of uncertainty on the signal strength parameter, for the resonant 1000 GeV signal.	100
10.1	The expected and observed 95% CL upper limits on the cross sections of non-resonant $gg \rightarrow hh$ production at $\sqrt{s} = 8$ TeV from individual analyses and their combinations. SM values are assumed for the h decay branching ratios. The cross-section limits normalized to the SM value are also included.	101
10.2	The mass ranges used for the search in each channel.	102
10.3	The expected and observed 95% CL upper limits on $\sigma(gg \rightarrow H) \times \text{BR}(H \rightarrow hh)$ in pb at $\sqrt{s} = 8$ TeV from individual analyses and their combinations. The SM branching ratios are assumed same for the light Higgs boson decay.	102
B.1	The event yields comparison on each selections of $t\bar{t}$ di-tau with $Z^0 \rightarrow \tau^+\tau^-$ in one b -tagged jet category.	109
B.2	The event yields comparison on each selections of $t\bar{t}$ di-tau with $Z^0 \rightarrow \tau^+\tau^-$ in two b -tagged jets category.	110

Chapter 1

Introduction

1.1 The Higgs Boson

1.1.1 Electroweak Interactions

Quantum Electrodynamics (QED)

The dynamics of charged fermions and electromagnetic interactions are described by Quantum Electrodynamics (QED), which is an abelian gauge theory with $U(1)_{EM}$ group symmetry. For the spinor ψ , the Dirac equation is given as

$$(i\gamma^\mu \partial_\mu)\psi = 0 \quad (1.1)$$

where γ^μ stands for gamma matrix.

The replacement of differential operator ∂_μ to covariant derivative D_μ as:

$$\partial_\mu \rightarrow D_\mu = \partial_\mu + iqA_\mu \quad (1.2)$$

then Equation 1.1 is to be:

$$(i\gamma^\mu D_\mu)\psi = 0 \quad (1.3)$$

This shows the dynamics of the Dirac particle in the electromagnetic potential. The given Lagrangian of QED defined as:

$$\mathcal{L}_{\text{QED}} = \bar{\psi}(i\gamma^\mu D_\mu - m)\psi - \frac{1}{4}F_{\mu\nu}F^{\mu\nu} \quad (1.4)$$

is invariant under $U(1)_{EM}$ local gauge transformation of ψ :

$$\psi \rightarrow \psi' = e^{-i\chi(x)}\psi \quad (1.5)$$

if following gauge transformation is performed

$$A_\mu \rightarrow A'_\mu = A_\mu - \partial_\mu\chi, \quad (1.6)$$

where $\bar{\psi} = \psi^\dagger\gamma^0$ and $F_{\mu\nu} = \partial_\mu A_\nu - \partial_\nu A_\mu$.

If the particle associated with A_μ has the mass, the mass term has to be added to Equation 1.4:

$$\mathcal{L}_{\text{mass}} = \frac{1}{2}M^2 A^\mu A_\nu. \quad (1.7)$$

This term is however not gauge invariant. This means the mass of gauge field has to be zero. Here the gauge field A_μ represents the photon.

Weak Interactions

The weak isospin triplet of $SU(2)_L$ is represented by three W fields. If the numbers $i = 1, 2, 3$ are assigned to W bosons like W^i , then the charged W bosons W^+ and W^- bosons are represented as:

$$W_\mu^\pm = \frac{1}{\sqrt{2}}(W_\mu^1 \mp iW_\mu^2) . \quad (1.8)$$

The weak interaction works to only left-handed fermions ψ_L . The $SU(2)$ doublet fermions and singlet fermions are assigned for the left- and right-handed fermions, respectively:

$$\text{Left - handed : } \psi_L = \begin{pmatrix} \nu_L \\ e_L \end{pmatrix}, \begin{pmatrix} u_L \\ d_L \end{pmatrix} \quad \text{Right - handed : } \psi_R = (e_R), (u_R), (d_R) \quad (1.9)$$

for the first generation leptons and quarks.

The local gauge transformation of $SU(2)_L$ state is given as:

$$\begin{aligned} \psi_L \rightarrow \psi'_L &= \exp\left(\frac{i}{2}\tau^i\chi_i(x)\right)\psi_L \\ W_\mu^i \rightarrow W_\mu'^i &= W_\mu^i - \frac{1}{g}\partial_\mu\chi^i + \epsilon_{ijk}\chi^jW_\mu^k \end{aligned} \quad (1.10)$$

where τ^i is the Pauli matrix. The covariant derivatives D_μ is introduced as:

$$\partial_\mu \rightarrow D_\mu = \partial_\mu + \frac{ig}{2}W_\mu(x)\chi \quad (1.11)$$

where g is the weak coupling constant, ϵ_{ijk}^i is antisymmetric symbol. The Lagrangian for weak interaction is:

$$\mathcal{L}_W = \bar{\psi}_L(i\gamma^\mu D_\mu - m)\psi_L - \frac{1}{4}W_{\mu\nu}^iW_i^{\mu\nu} \quad (1.12)$$

where $W_{\mu\nu}^i = \partial_\mu W_\nu^i - \partial_\nu W_\mu^i + ig\epsilon_{ijk}^iW_\mu^jW_\nu^k$. The mass terms such as $m\psi\psi$ for fermions and $m_W^2W_\mu W^\mu$ for W bosons are forbidden, in order to require the gauge invariant. Thus, $SU(2)$ forbids the mass term of fermions and bosons.

Electroweak unification

In the Standard Model (SM), Electromagnetic and Weak interactions are unified to the Electroweak interaction by $SU(2)_L \times U(1)_Y$. Three W^i bosons and the B field having weak hypercharge of $U(1)_Y$ are taking up the electroweak interaction. The neutral state W^3 is mixing with the B field. Z^0 and γ are the physical particles constructed from this mixing.

$$\begin{aligned} A_\mu &= B_\mu \cos \theta_w + W_\mu^3 \sin \theta_w \\ Z_\mu &= -B_\mu \sin \theta_w + W_\mu^3 \cos \theta_w . \end{aligned} \quad (1.13)$$

The mixing angle is called as ‘‘Weinberg angle’’ (θ_w) representing the ratio of the coupling constants of the $SU(2)$ and $U(1)_Y$.

$$\tan \theta_w = \frac{g'}{g} . \quad (1.14)$$

The Lagrangian of electroweak is given as:

$$\mathcal{L}_{EW} = i\bar{\psi}_L\gamma^\mu D_{L\mu}\psi_L + i\bar{\psi}_R\gamma^\mu D_{R\mu}\psi_R - \frac{1}{4}W_{\mu\nu}^iW_i^{\mu\nu} - \frac{1}{4}B_{\mu\nu}B^{\mu\nu} \quad (1.15)$$

where $B_{\mu\nu} = \partial_\mu B_\nu - \partial_\nu B_\mu$.

Here, $D_{L\mu}$ and $D_{R\mu}$ are covariant derivatives as introduced to satisfy gauge invariance under $SU(2)_L \times U(1)_Y$.

$$D_{L\mu} = \partial_\mu + \frac{i}{2}g\tau_i W^i_\mu + \frac{i}{2}g'Y B_\mu \quad (1.16)$$

$$D_{R\mu} = \partial_\mu + \frac{i}{2}g'Y B_\mu \quad (1.17)$$

where Y stands for a hypercharge operator. B boson interacts to not only left-handed but also right-handed components of the fermion fields through hypercharge. The mass terms are forbidden, in order to be gauge invariant. This inconsistency with the experimental result is resolved by Brout-Englert-Higgs (BEH) mechanism described later.

Electroweak symmetry breaking

The Lagrangian with one complex scalar field added into gauge field is given as:

$$\mathcal{L} = -\frac{1}{4}B_{\mu\nu}B^{\mu\nu} - \frac{1}{4}W_{\mu\nu}W^{\mu\nu} + (D_\mu\phi)^\dagger(D^\mu\phi) - V(\phi) \quad (1.18)$$

where $D_\mu = \partial_\mu - ieA_\mu$, and $V(\phi)$ is the potential of ϕ described as:

$$V(\phi) = \mu^2\phi^\dagger\phi + \lambda(\phi^\dagger\phi)^2. \quad (1.19)$$

Here, ϕ stands for the scalar field of $SU(2)_L$ group, written as:

$$\phi = \begin{pmatrix} \phi^+ \\ \phi^0 \end{pmatrix} = \frac{1}{\sqrt{2}} \begin{pmatrix} \phi_1 + i\phi_2 \\ \phi_3 + i\phi_4 \end{pmatrix} \quad (1.20)$$

The $\lambda \geq 0$ on Equation 1.19 is required to stabilize the field. The shape of potential is split to two types based on the sign of μ^2 . They are shown in Figure 1.1.

- $\mu^2 > 0$
The shape of this potential is corresponding to (a) in Figure 1.1. In this case, the minimum potential (vacuum) is given when $\phi = 0$, and μ^2 is corresponding to the mass of the field.
- $\mu^2 < 0$
The shape of this potential is corresponding to (b) in Figure 1.1. The vacuum state is given on the condition of:

$$(\phi^1)^2 + (\phi^2)^2 + (\phi^3)^2 + (\phi^4)^2 = \frac{\mu^2}{\lambda} \quad (1.21)$$

$$\text{lead from } \frac{\partial V}{\partial \phi} = 0 \quad (1.22)$$

There are four freedoms of ϕ^1, ϕ^2, ϕ^3 and ϕ^4 . Here what only ϕ^3 has non-zero value “ v ” and others have zero is assumed, then ϕ_{vacuum} is to be:

$$\phi_{\text{vacuum}} = \frac{1}{\sqrt{2}} \begin{pmatrix} 0 \\ v \end{pmatrix}, \quad (1.23)$$

and the value v is,

$$v = \sqrt{\frac{-\mu^2}{\lambda}}. \quad (1.24)$$

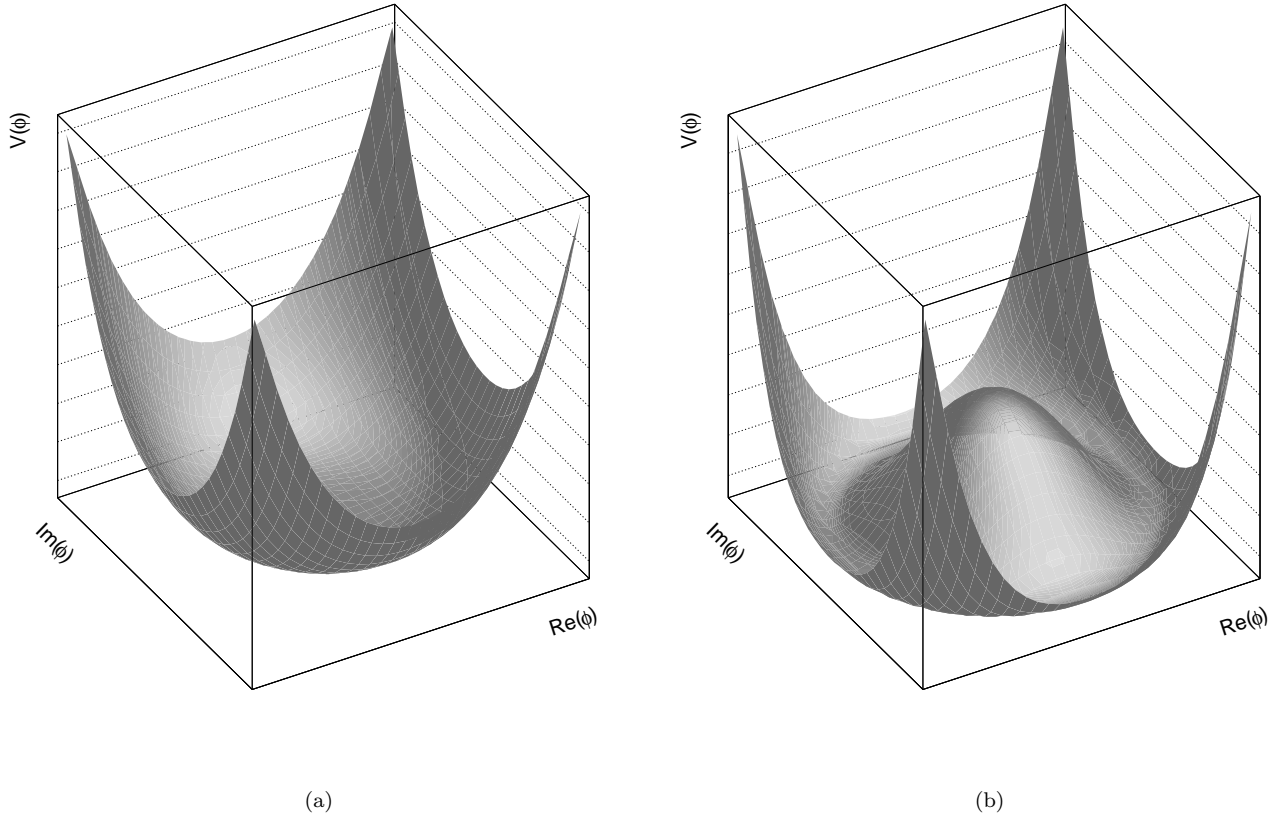


Figure 1.1: Potential $V(\phi)$ in case of (a) before and (b) after symmetry breaking.

The v value is called as vacuum expectation value. The vacuum state is degenerate up to infinity on the circle satisfying $|\phi| = v/\sqrt{2}$. The rotational symmetry among four comparable fields ϕ^1, ϕ^2, ϕ^3 and ϕ^4 is broken by choosing only one field (ϕ^3) as the vacuum state.

Higgs field

The complex scalar field is re-written by introducing χ^i with three components and higgs field h , to consider the expansion around the stable state.

$$\phi = \frac{1}{\sqrt{2}} \exp\left(\frac{i}{2} \tau_i \chi^i\right) \begin{pmatrix} 0 \\ v + h \end{pmatrix}. \quad (1.25)$$

The following gauge transformation removes the three freedoms of χ from Lagrangian.

$$\phi \rightarrow \phi' = U(\chi) \phi \quad (1.26)$$

$$\text{, where } U(\chi) = \exp\left(-\frac{i}{2} \tau_i \chi^i\right). \quad (1.27)$$

$$\phi = \frac{1}{\sqrt{2}} \begin{pmatrix} 0 \\ v + h \end{pmatrix}. \quad (1.28)$$

After the symmetry breaking, the Equation 1.28 is assigned into the Lagrangian. Then Lagrangian is to be:

$$\begin{aligned} \mathcal{L} = & \left| \partial_\mu h + i \frac{1}{2\sqrt{2}}(v+h) \begin{pmatrix} gW_\mu^1 - igW_\mu^2 \\ -gW_\mu^3 + g'B_\mu \end{pmatrix} \right|^2 \\ & - \frac{1}{4}W_{\mu\nu}^i W_i^{\mu\nu} - \frac{1}{4}B_{\mu\nu}B^{\mu\nu} - \frac{\mu^2}{2}(v+h)^2 - \frac{\lambda}{4}(v+h)^4 \end{aligned} \quad (1.29)$$

After a calculation, following two terms are shown in the equation:

$$\begin{aligned} & \frac{g^2 v^2}{8} ((W_\mu^1)^2 + (W_\mu^2)^2), \\ & \frac{v^2}{8} (gW_\mu^3 - g'B_\mu)^2 \end{aligned} \quad (1.30)$$

These correspond to the mass terms of W^\pm and Z^0 bosons. The mixing of W^3 and B leads the fields of Z_μ^0 and photon A_μ as already described in Equation 1.13. Furthermore from the mass term of h^2 , the mass of higgs boson associated with the higgs field is given as:

$$m_h = \sqrt{-2\mu^2}. \quad (1.31)$$

And the term of h^3 is to be:

$$\lambda v h^3. \quad (1.32)$$

This represents the higgs trilinear-self-coupling. The one of the freedoms of four complex scalar fields is assigned to higgs field h and three freedoms are absorbed by spin-freedom of the gauge bosons.

1.1.2 Discovery of Higgs Boson

The higgs boson has been discovered with ATLAS and CMS experiments at LHC in 2012 [1, 2]. Figure 1.2 (a) and (b) show the mass distribution of $h \rightarrow \gamma\gamma$ channel and local p_0 value of the standard model higgs boson search in the $h \rightarrow ZZ^* \rightarrow 4l$, $h \rightarrow \gamma\gamma$ and $h \rightarrow WW^* \rightarrow e\nu\mu\nu$ channels combined with the amount of the data collected in 2011 and 2012 of 4.6-4.8 fb⁻¹ and 5.8-5.9 fb⁻¹ at the center-of-mass energy $\sqrt{s} = 7$ and 8 TeV, respectively. The p -value, which is the probability that the observed event excess is explained by the background only, corresponds to a significance of 6σ around the mass of $m_h = 125$ GeV.

After the discovery, measurements of the higgs boson, i.e. mass m_h , couplings to gauge bosons and fermions, and spin and parity quantum numbers are performed in the ATLAS experiment.

The result using the full dataset of 2011 and 2012 corresponding to 4.7 fb⁻¹ at $\sqrt{s} = 7$ TeV and 20.3 fb⁻¹ at $\sqrt{s} = 8$ TeV sets the mass of higgs to be $m_h = 125.36 \pm 0.37$ (stat) ± 0.18 (syst) GeV from the $h \rightarrow \gamma\gamma$ and $h \rightarrow ZZ^* \rightarrow 4l$ channels combined [3]. The discovery of the higgs boson was made through analyses of the bosonic decay modes. The $h \rightarrow \tau^+\tau^-$ has been reported the first evidence of higgs Yukawa coupling [4]. The mass distribution and the local p_0 value are shown in the Figure 1.3. $h \rightarrow b\bar{b}$ channel is also analyzed as well as $h \rightarrow \tau^+\tau^-$ channel. The observed and expected 95% CL limit is shown in the Figure 1.4. The signal strength normalized by the SM higgs production measured using the full dataset of 2011 and 2012 and combination of all production modes and decay channels is $\mu = 1.18^{+0.15}_{-0.14}$ as shown in Figure 1.5 [5].

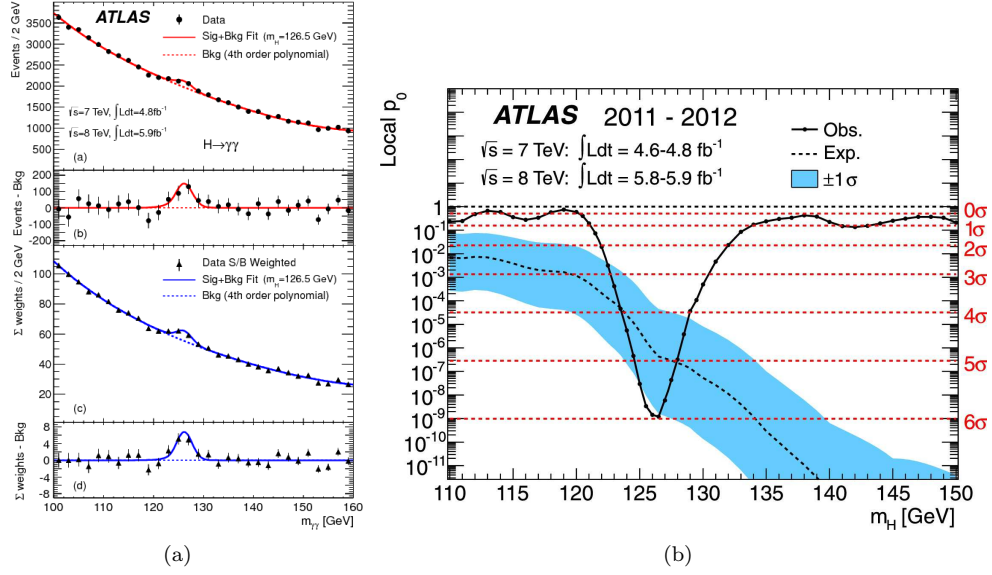


Figure 1.2: (a) $\gamma\gamma$ mass distribution of $h \rightarrow \gamma\gamma$ channel. (b) The local p_0 value for the $h \rightarrow ZZ^* \rightarrow 4l$, $h \rightarrow \gamma\gamma$ and $h \rightarrow WW^* \rightarrow e\nu\mu\nu$ channels combined. The SM Higgs boson mass hypothesis of $m_H = 126.5$ GeV is used. The data statistics is corresponding to $4.6\text{-}4.8 \text{ fb}^{-1}$ and $5.8\text{-}5.9 \text{ fb}^{-1}$ at $\sqrt{s} = 7$ and 8 TeV, respectively. The observed (solid) local p_0 as a function of m_H in the low mass range. The dashed curve shows the expected local p_0 under the hypothesis of a SM Higgs boson signal at that mass with its $\pm 1\sigma$ band. The horizontal dashed lines indicate the p -values corresponding to significance of 1 to 6 σ . [1]

The spin-parity of $J^P = 0^-, 1^+, 1^-, 2^+$ assumptions are excluded at confidence levels more than 97.8% obtained from $h \rightarrow \gamma\gamma$, $h \rightarrow ZZ^* \rightarrow 4l$ and $h \rightarrow WW^* \rightarrow l\nu l\nu$ channels using corresponding dataset of 20.7 fb^{-1} at $\sqrt{s} = 8$ TeV (only $h \rightarrow ZZ^* \rightarrow 4l$ of 4.6 fb^{-1} at $\sqrt{s} = 7$ TeV is included) [6]. It is shown in Figure 1.6. Thus Higgs boson is consistent with 0^+ spin-parity state.

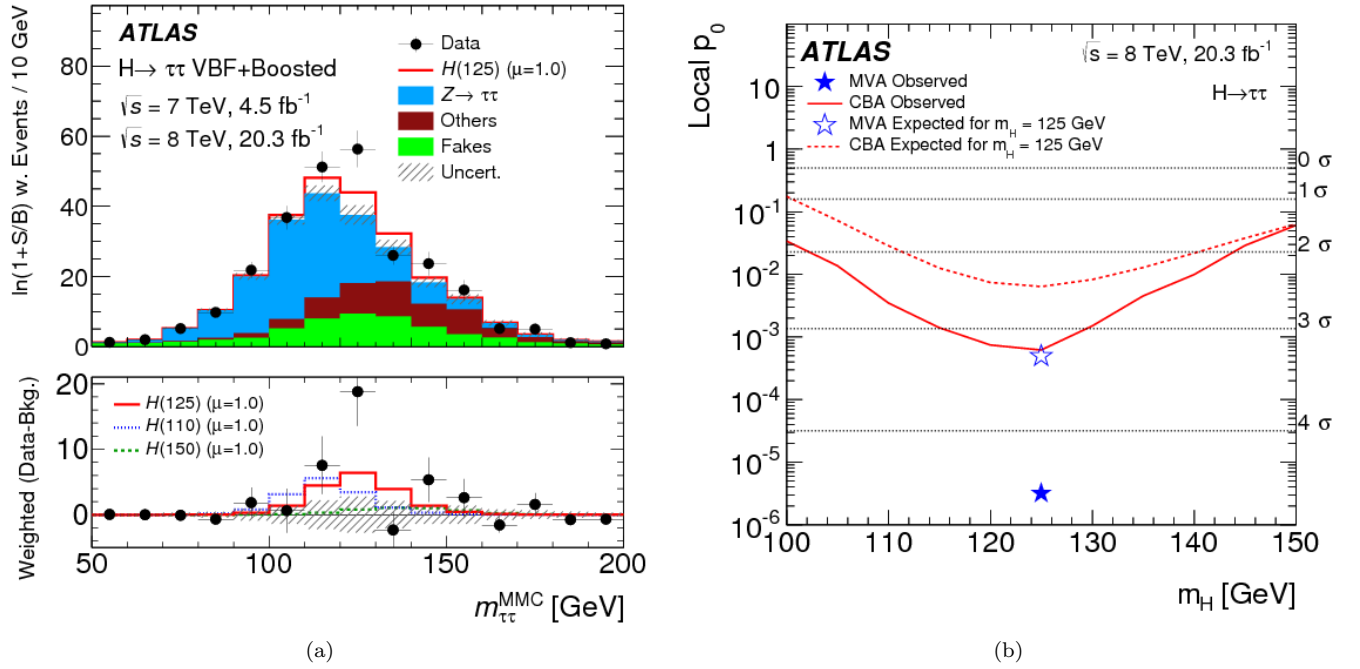


Figure 1.3: (a) The mass of di-tau system reconstructed by MMC described in Section 5.7.2 for the MVA based analysis and, all lep-lep, lep-had and had-had channels are combined by weighted by $\ln(1 + S/B)$. (b) Observed (solid red) and expected (dashed red) p_0 values for a given m_h . All channels are combined in the cut-based analysis (CBA). The expected p_0 values are given for the background-only hypothesis. The corresponding observed and expected p_0 values for the multivariate analysis (MVA) are indicated for $m_H = 125$ GeV by a full and open star respectively. [4]

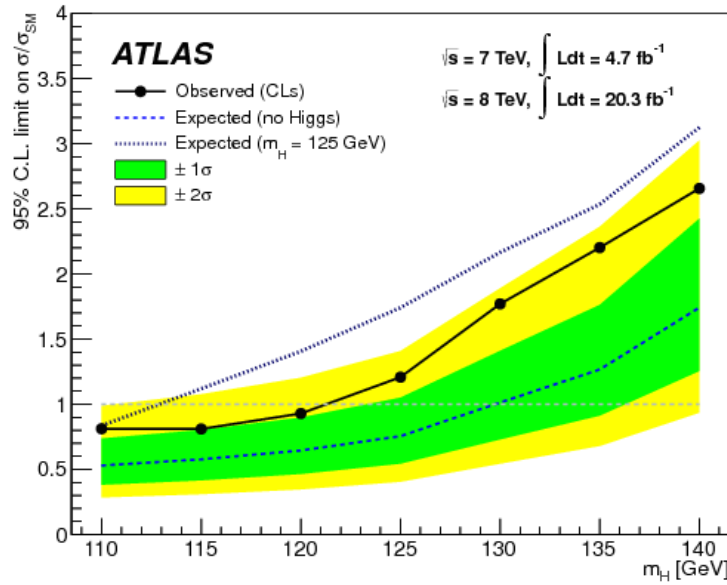


Figure 1.4: The result from $h \rightarrow b\bar{b}$ analysis. Observed (solid) and expected (dashed) 95% CL cross-section upper limits normalized to the SM higgs boson production cross section for given mass m_h with full data set collected in 2011 and 2012 and including all analysis channels.

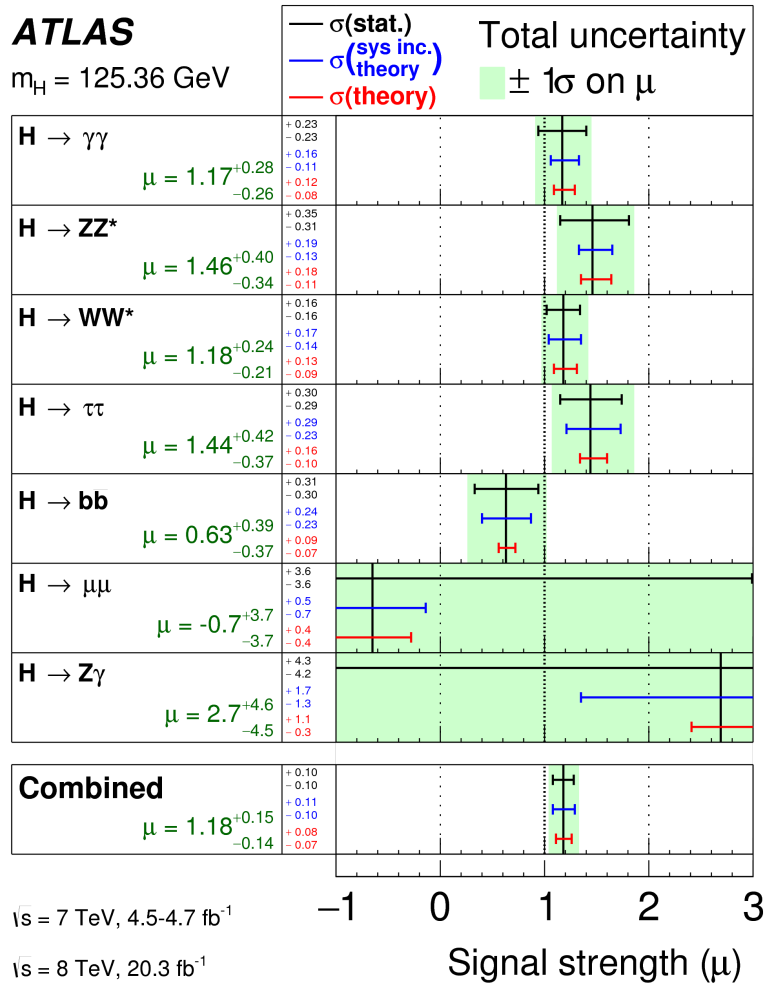


Figure 1.5: The observed signal strengths normalized by the SM prediction and uncertainties for different Higgs boson decay channels and their combination for $m_h = 125.36 \text{ GeV}$.

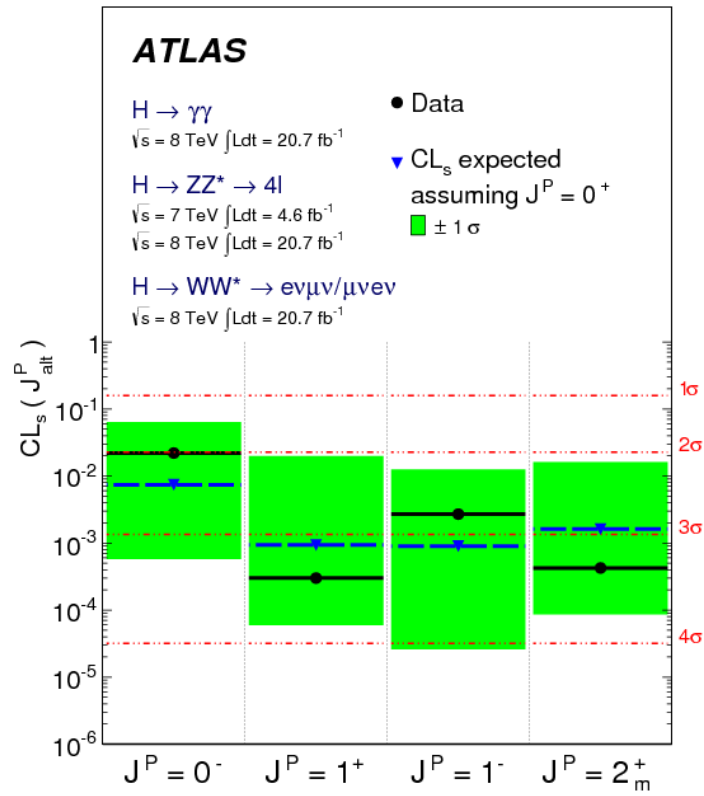


Figure 1.6: Observed and expected limits for alternative spin-parity hypotheses assuming a $J^P = 0^+$ signal are shown with the black and blue points, respectively.

1.2 Higgs Boson Pair Production

Higgs Boson Pair Production within the Standard Model

After the higgs boson discovery, the significant progress has been made in measuring the coupling strength of the higgs boson to vector bosons and to fermions as well as studying the spin-parity of higgs boson. To examine whether the observed higgs boson is truly the SM higgs is very important, and to search for beyond the standard model (BSM) is carried out in newly discovered higgs boson production and decay. The sign of the BSM has not been observed from any one of the current results. The one of the remaining and most interesting confirmations about higgs boson is the self-coupling among higgs bosons. The electroweak symmetry breaking leads the existence

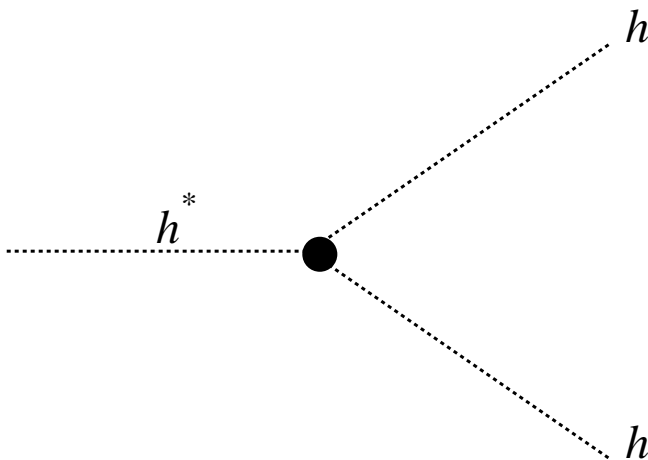


Figure 1.7: Higgs boson trilinear-self-coupling.

of higgs boson, which is described in Section 1.1 in framework of the SM. Since it predicts higgs self-coupling as well, its measurement is essential in testing the BEH mechanism. The self-coupling leads the higgs boson pair production (di-higgs) as shown in Figure 1.7. The processes of di-higgs production in the SM are shown in Figure 1.8 [12]. The di-higgs production measurement is a direct test of the BEH mechanism. However, since di-higgs production cross-section in the SM prediction is quit small as summarized in Table 1.2 [12], the current amount of data provided by the LHC collision does not have a potential to discover di-higgs production in the SM as found from the studies of [7–11]. However it is significantly meaningful to quantify the sensitivity even

Table 1.1: The total Higgs pair production cross section in the main channels at the LHC (in fb) for given c.m. energies(in TeV) with $M_H = 125$ GeV. [12]

\sqrt{s} [TeV]	$\sigma_{gg \rightarrow hh}^{NLO}$ [fb]	$\sigma_{qq' \rightarrow hhqq'}^{NLO}$ [fb]	$\sigma_{q\bar{q} \rightarrow Whh}^{NNLO}$ [fb]	$\sigma_{q\bar{q} \rightarrow Zhh}^{NNLO}$ [fb]	$\sigma_{q\bar{q}/gg \rightarrow t\bar{t}hh}^{LO}$ [fb]
8	8.16	0.49	0.21	0.14	0.21
14	33.89	2.01	0.57	0.42	1.02
33	207.29	12.05	1.99	1.68	7.91
100	1417.83	79.55	8.00	8.27	77.82

for the current amount of data and to develop the analysis methods for future measurements.

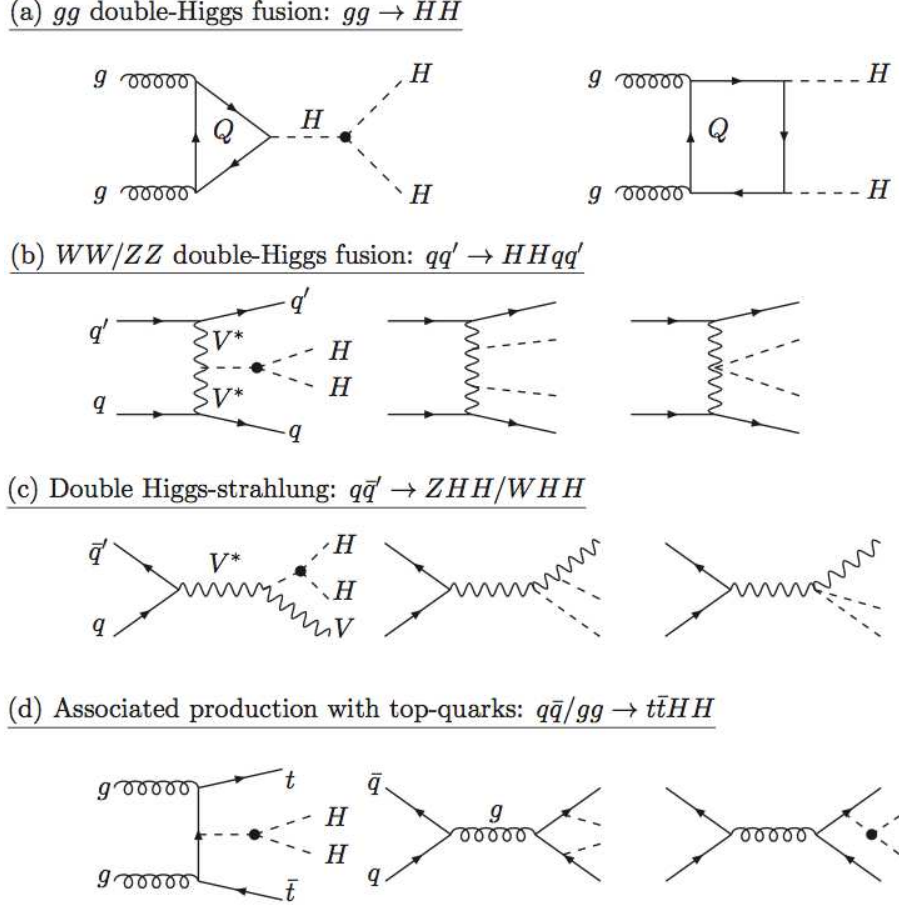


Figure 1.8: Some generic Feynman diagrams contributing to Higgs pair production at hadron colliders. [12] The capital "H" stands for standard model higgs in these diagrams.

Higgs Boson Pair Production in the Beyond Standard Model

The cross-section in the standard model is quite small at $\sqrt{s} = 8$ TeV pp collision, however BSM can potentially enhance the cross-section. If the trilinear-self-coupling λ_{hhh} shown in Figure 1.7 does not exist or is negative, then higgs pair production in other processes is enhanced. Figure 1.9 shows the ratio of the cross sections compared with the standard model predictions at given $\lambda_{hhh}/\lambda_{hhh}^{SM}$ [12].

If λ_{hhh} is -5 times with respect to the SM prediction, the rate of $qq' \rightarrow hhqq'$ is enhanced to about 40 times. This value is not so far from the analysis sensitivity achievable for the $\sqrt{s} = 8$ TeV Run1 data. Furthermore the production cross section is enhanced in the Run2 thanks to upgrade the center-of-mass energy to $\sqrt{s} = 13$ and 14 TeV. If $\lambda_{hhh}/\lambda_{hhh}^{SM} = -5$ is assumed, the cross section of $qq' \rightarrow hhqq'$ is about 800 fb (Figure 1.10). Searching this process in Run1 itself is worthwhile, as well as it is very important from the point of the development and study of the analysis method for Run2.

The existence or non-existence of additional higgs boson is also one of the important questions for the higgs boson physics. The "Two-Higgs-Doublet-Model (2HDM)" is one of the simplest expansion of the Higgs sector. This resonant can decay into di-higgs, consequence the cross section

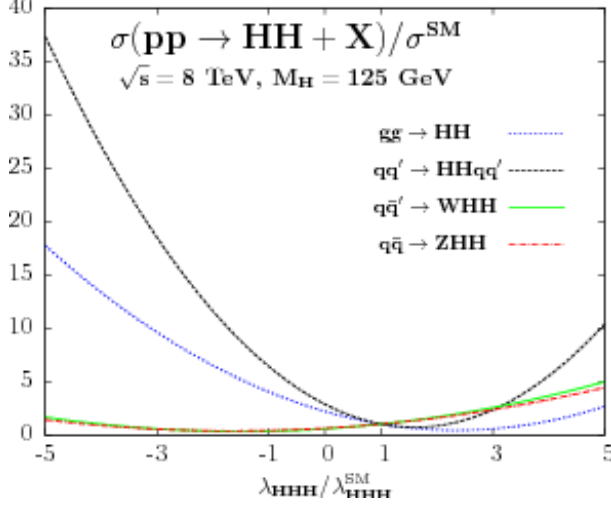


Figure 1.9: The ratio of the cross sections compared with standard model at a given $\frac{\lambda_{hhh}}{\lambda_{hhh}^{SM}}$ at $\sqrt{s} = 8$ TeV. [12]

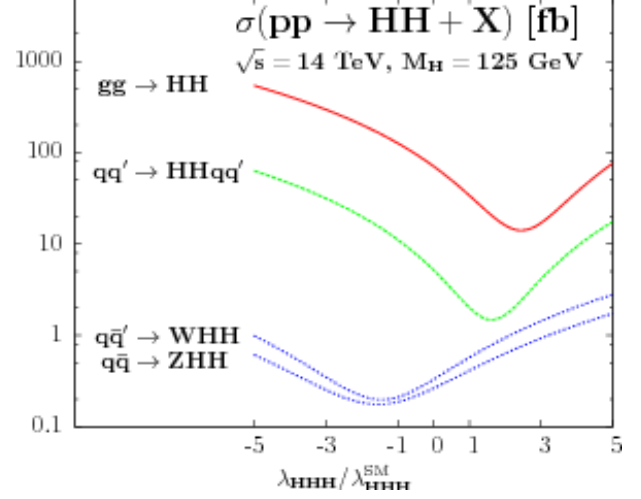


Figure 1.10: di-higgs production cross sections in femtobarn given at a given $\frac{\lambda_{hhh}}{\lambda_{hhh}^{SM}}$ at $\sqrt{s} = 14$ TeV. [12]

of di-higgs is strongly enhanced. The cross sections times branching ratios of 2HDM heavy scalar higgs are shown on Figure 1.11 [12], where the units picobarn for $\sqrt{s} = 8$ TeV pp collision. The channel decaying to di-higgs from heavier state opens if the scalar mass m_H is greater than ~ 250 GeV ($= 2m_h$). The branching ratio decreases for m_H from 350 GeV which is corresponding to the $2 \times M_{top}$.

The 2HDM model requires two doublets of scalar fields.

$$\phi_i = \begin{pmatrix} \phi_i^+ \\ \frac{1}{\sqrt{2}}(v_i + \phi_i + i\chi_i) \end{pmatrix} \quad (i = 1, 2) \quad (1.33)$$

The higgs potential in the 2HDM is generally given as:

$$\begin{aligned} V(\phi_1, \phi_2) = & \frac{\lambda_1}{2}(\phi_1^\dagger \phi_1)^2 + \frac{\lambda_2}{2}(\phi_2^\dagger \phi_2)^2 + \lambda_3(\phi_1^\dagger \phi_1)(\phi_2^\dagger \phi_2) \\ & + \lambda_4(\phi_1^\dagger \phi_2)(\phi_2^\dagger \phi_1) + \frac{1}{2}(\lambda_5(\phi_1^\dagger \phi_2)^2 + h.c.) \\ & - \frac{1}{2}(m_{11}^2 \phi_1^\dagger \phi_1 + (m_{12}^2 \phi_1^\dagger \phi_2 + h.c.) + m_{22}^2 \phi_2^\dagger \phi_2) \end{aligned} \quad (1.34)$$

ϕ_1 and ϕ_2 get the vacuum expectation values v_1, v_2 respectively. β is defined as the ratio of v_1 and v_2 .

$$\tan \beta = v_2/v_1 \quad (1.35)$$

There are eight freedoms, but the number of freedoms decreases to five because three fields are absorbed as longitudinal polarization of gauge bosons. The rest of five fields are the neutral scalar fields h, H , pseudoscalar A and charged higgs fields H^\pm . The pseudoscalar field A and charged higgs fields are given as:

$$H^\pm = -\phi_1^\pm \sin \beta + \phi_2^\pm \cos \beta \quad (1.36)$$

$$A = -\chi_1 \sin \beta + \chi_2 \cos \beta \quad (1.37)$$

The light scalar field h can be regarded as to the observed Higgs boson.

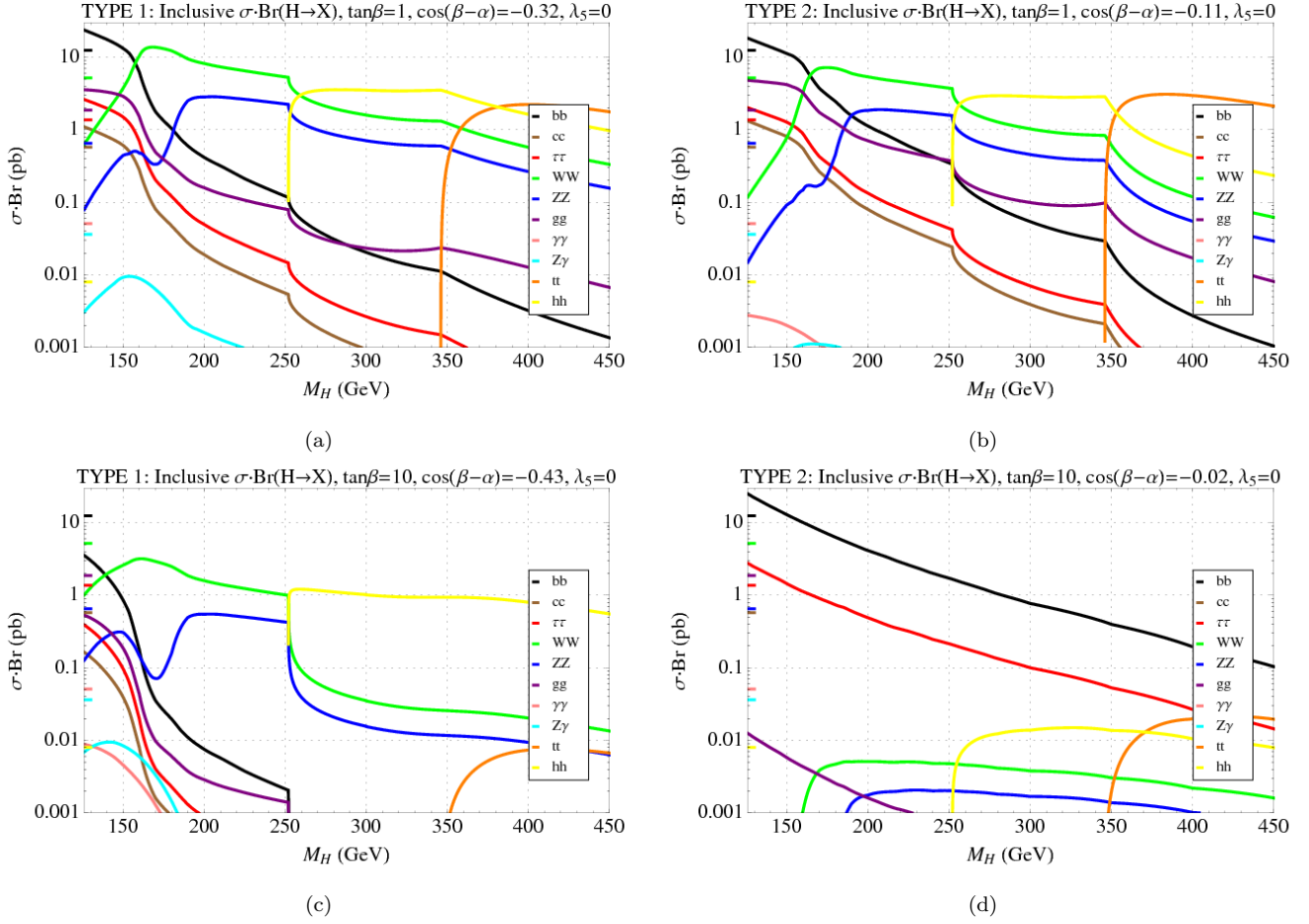


Figure 1.11: The cross sections times branching ratio of 2HDM heavy scalar higgs in units of picobarn for $\sqrt{s} = 8$ TeV pp collision for given mass. The configurations are, Upper left: $\tan\beta = 1$, $\cos(\beta - \alpha) = -0.32$ for Type 1 2HDM. Upper right: $\tan\beta = 1$, $\cos(\beta - \alpha) = -0.11$ for Type 2 2HDM. Lower left: $\tan\beta = 10$, $\cos(\beta - \alpha) = -0.43$ for Type 1 2HDM. Lower right: $\tan\beta = 10$, $\cos(\beta - \alpha) = -0.02$ for Type 2 2HDM, where α represents the mixing of h and H [15].

The physics of di-higgs is currently motivated within the BSM. It is split to two categories; one is the non-resonant model, and another is the resonant model.

- Non-resonant:
Enhancement of $qq' \rightarrow hhqq'$ led within BSM increasing the higgs trilinear-self-coupling described above is included in this category. Other models, composite model [13] and light colored scalars [14] could enhance the higgs pair production.
- Resonant Process:
The 2HDM heavy higgs described above is included in this category. Graviton [16], Radion (whose field is useful for stabilizing the graviton field) [17] and other resonant models could decay into higgs boson pair.

1.3 $hh \rightarrow b\bar{b}\tau^+\tau^-$ Final State

1.3.1 Advantages in $hh \rightarrow b\bar{b}\tau^+\tau^-$ Channel

The $hh \rightarrow b\bar{b}\tau^+\tau^-$ final state is examined as a di-higgs search in this analysis. This search channel has the following advantages:

- Large branching ratio:
 $hh \rightarrow b\bar{b}\tau^+\tau^-$ has third largest branching ratio 7.1 %. The branching ratio of the SM higgs pair in percent is summarized in Table 1.2.

Table 1.2: The branching ratios of di-higgs decay combinations $hh \rightarrow XXY Y$ in percent are shown. $hh \rightarrow b\bar{b}\tau^+\tau^-$ has the third largest branching ratio 7.1 % which is shown in bold.

	bb	WW	$\tau^+\tau^-$	ZZ	$\gamma\gamma$
bb	32	25	7.1	3.1	0.26
WW	-	5	2.8	1.2	0.1
$\tau^+\tau^-$	-	-	0.39	0.34	0.029
ZZ	-	-	-	0.076	0.013
$\gamma\gamma$	-	-	-	-	0.000053

- Clean signature:
The events containing one light lepton (electron or muon) is used in this analysis. This light lepton is provided from leptonic τ decay. This requirement suppresses the jets background processes, giving clean signature.
- Reconstructable invariant mass:
The standard model higgs boson mass should be powerful discriminant between signal and background. Both invariant masses of $b\bar{b}$ and $\tau^+\tau^-$ are reconstructable. For example, $hh \rightarrow b\bar{b}b\bar{b}$ channel has three $b\bar{b}$ combinations and this degrades the mass resolution. Therefore, $b\bar{b}\tau^+\tau^-$ mass is also reconstructable.
- Triggerable:
The single lepton trigger which shows a great performance can be used as an efficient event trigger.

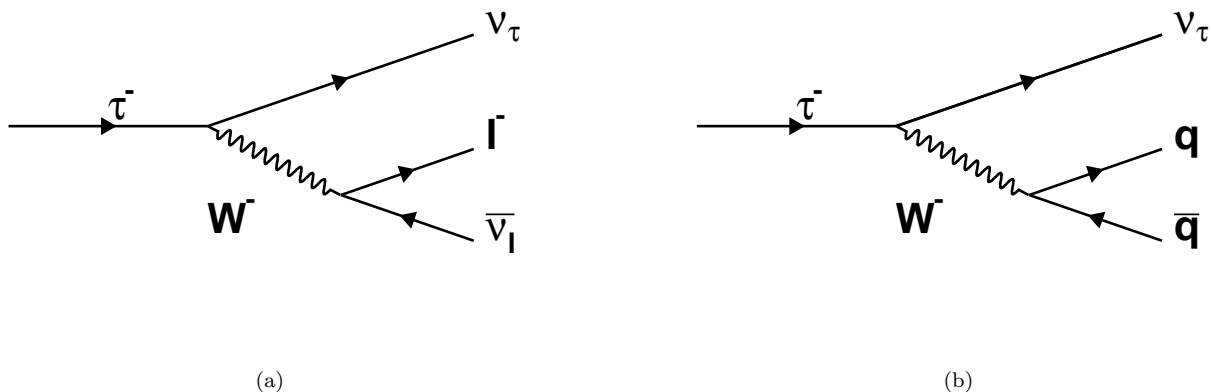


Figure 1.12: The feynman diagrams of tau lepton decay (a) leptonically and (b) hadronically.

1.3.2 Signature of τ Decay

The observable objects of $hh \rightarrow b\bar{b}\tau^+\tau^-$ are divided into three main classes based on τ decay modes, leptonic or hadronic decays. The difference of these decay modes, leptonic or hadronic decay, represented by the decay of the W^\pm boson from τ decay. In the leptonic decay W^\pm boson decays into light lepton (Figure 1.12(a)), and hadronic decay stands for what W^\pm boson decays hadronically (Figure 1.12(b)). The two decay modes of τ pair decay give three combinations, (1) both τ decay hadronically (di-lepton), (2) one of them decays leptonically and another decays hadronically (semi-lepton) and (3) both τ decay leptonically (all-hadronic). The semi-lepton channel was chosen in this analysis for the following reasons:

- Large branching ratio:
Table 1.3 shows the decay branching ratio of τ pair decay categories in percent. The semi-lepton mode has the highest branching ratio 46%.

Table 1.3: The branching ratio of $\tau^+\tau^-$.

di-lepton	semi-lepton	all-hadronic
12%	46%	42%

- Clean signature:
Since energetic jets have certain probability of identified as a lepton (fake lepton), the backgrounds including jets can be suppressed by requiring a light lepton in the final state.

Chapter 2

LHC Accelerator and ATLAS Detector

The proton-proton collision is provided by the Large Hadron Collider (LHC), and the data was collected with the ATLAS detector. In this section, the LHC, ATLAS detector and their operations are described.

2.1 The Large Hadron Collider

The Large Hadron Collider (LHC) at CERN is located on the border of France and Switzerland, being the currently largest and most powerful particle collider in the world. The LHC is composed of superconducting magnets aligned along a 27 km circumference tunnel originally constructed for the LEP collider. The main operation of the LHC is proton-proton collision, but heavy ions are used as well. This section focuses on the proton-proton collision which is used in our analysis. Thanks to the heavier proton's mass compared with electrons, energy loss by synchrotron radiation, which is proportional to $1/m^4$ (Equation (2.1)), can be suppressed, therefore proton beam can reach very high energy.

$$\Delta E = \frac{4\pi\alpha\hbar c\beta^3\gamma^4}{3R} \propto \left(\frac{E}{m}\right)^4 \times \frac{1}{R} \quad (2.1)$$

where $\beta = v/c$, $\gamma = (1 - \beta^2)^{-\frac{1}{2}}$. The maximum design center of mass energy is $\sqrt{s} = 14$ TeV. The LHC has been operated at $\sqrt{s} = 7$ TeV and $\sqrt{s} = 8$ TeV, in 2010-2011 and 2012, respectively. In 2015, $\sqrt{s} = 13$ TeV has been reached after finishing the shutdown in 2013. The LHC is planning to upgrade to $\sqrt{s} = 14$ TeV in near future.

2.1.1 Proton Injection to The LHC

The proton beam is accelerated piecemeal in several machines. Figure 2.1 shows the chain of proton injection to the LHC. The protons, which are provided from hydrogen gas stripped with their electrons by using electric field, are accelerated to energy of 50 MeV by the linear accelerator (Linac2). Then the proton beam is injected to the Proton Synchrotron Booster (PSB), accelerated up to 1.4 GeV and sent into the Proton Synchrotron (PS). In the PS, the beam reaches 25 GeV, and is transferred into the Super Proton Synchrotron (SPS) to be accelerated up to 450 GeV, before injection into the two beam pipes of the LHC. The beams circulating in the pipes are accelerated to their maximum energy and collided at the detectors. The strong magnetic field is needed for bending high energy protons.

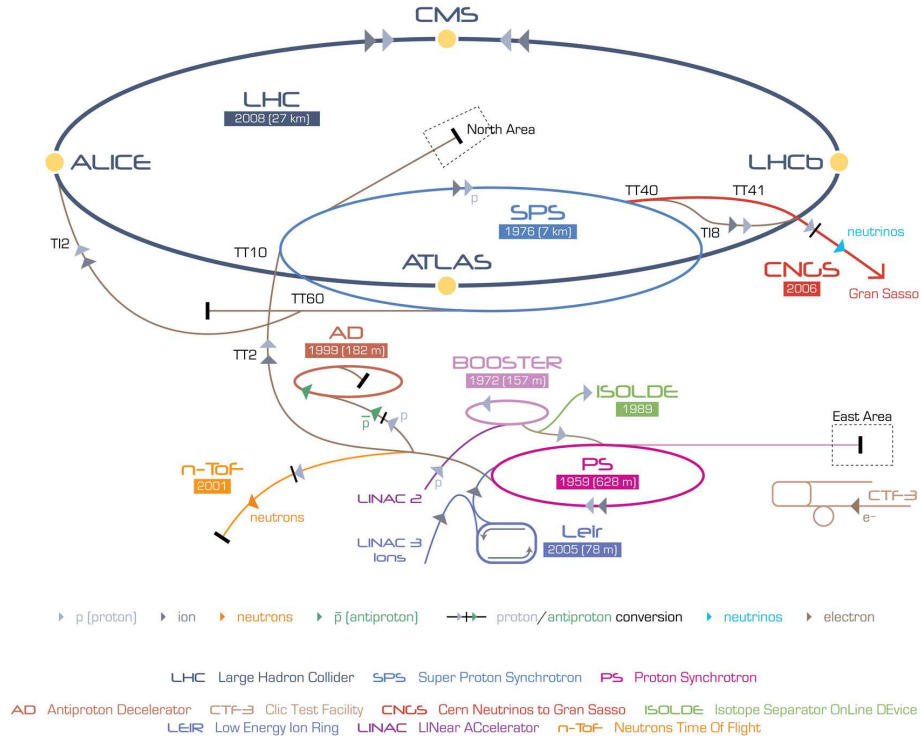


Figure 2.1: The proton injection to the LHC. [18]

2.1.2 The LHC Parameters

Table 2.1 shows the LHC beam configuration parameters of design value and 2012 Run.

Table 2.1: The beam parameters for pp collision in LHC 2012 Run.

	Design value	2012 Run value
Center of Mass Energy [TeV]	14	8
Bunch spacing [ns]	25	50
Number of proton bunches	2808	1380
Number of particles per bunch	1.15×10^{11}	1.7×10^{11}
Peak luminosity [$\text{cm}^{-2}\text{s}^{-1}$]	1.0×10^{34}	7.7×10^{33}
Dipoles magnetic fields [T]	8.33	4.76
Bunch length [cm]	7.55	≥ 9
Transverse beam size at IP [μm]	16.7	19
Crossing angle at IP [μrad]	285	290

2.2 The ATLAS Detector

The data is collected with the ATLAS detector (Fig 2.2). The ATLAS detector is composed of several sub-detectors. In this section, descriptions of each detectors are given.

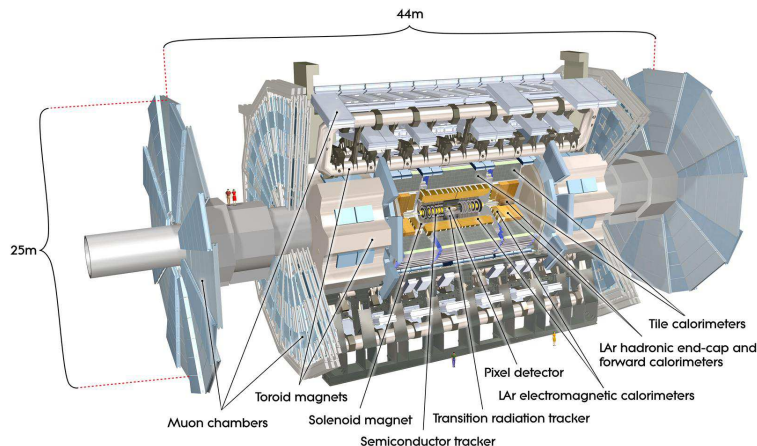


Figure 2.2: The ATLAS Detector.

2.2.1 The Inner Detectors

The Inner Detector is in a cylindrical shape with the overall size is 1150 mm, 7024 mm in length, as shown in Figure 2.3. The solenoid magnet described later is surrounding the Inner Detector. The Inner Detectors occupy the innermost region of ATLAS detector, composed radially of Pixel Detector (PIXEL), Semiconductor Tracker (SCT) and Transition Radiation Tracker (TRT). This detects the hit positions of charged particles and measure momenta and impact parameters, which are used to reconstruct the vertex position of the event. The features of the sub-detectors are that PIXEL and SCT provide fine-granularity measurements thanks to high-precision semiconductor detectors, and that TRT gives many tracking points thanks to large detector size. The high precision track reconstruction in both ϕ and z is achievable by combination of three, four and 36 tracking points at PIXEL, SCT and TRT, respectively, within pseudorapidity $|\eta| < 2.5$. Here η is defined as:

$$\eta = -\ln \left(\tan \left(\frac{\theta}{2} \right) \right) \quad (2.2)$$

where θ is polar angle from the proton beam with the original at the collision point. The momentum resolution of Inner Detector is

$$\sigma_{pT/p} \sim 0.05\% p_T \oplus 1\% \quad (2.3)$$

The details of sub-detectors are described following:

PIXEL detector (PIXEL)

The PIXEL is located at the place closest to the collision point. The detector sensors are aligned cylindrically around the beam axis in the barrel region and perpendicular to the beam axis in the end-cap regions. The high granularity measurement is required because of high particle density. The PIXEL provides precision tracking within the coverage of $|\eta| < 2.5$. The pixel layers are segmented in $R - \phi$ and in z , and the sensor size is $50 \times 400 \mu\text{m}$ in $R - \phi \times z$. The total readout channels is 80.4 million. The spatial resolutions are $10 \mu\text{m}$ and $115 \mu\text{m}$ in $R - \phi$ and in z , respectively.

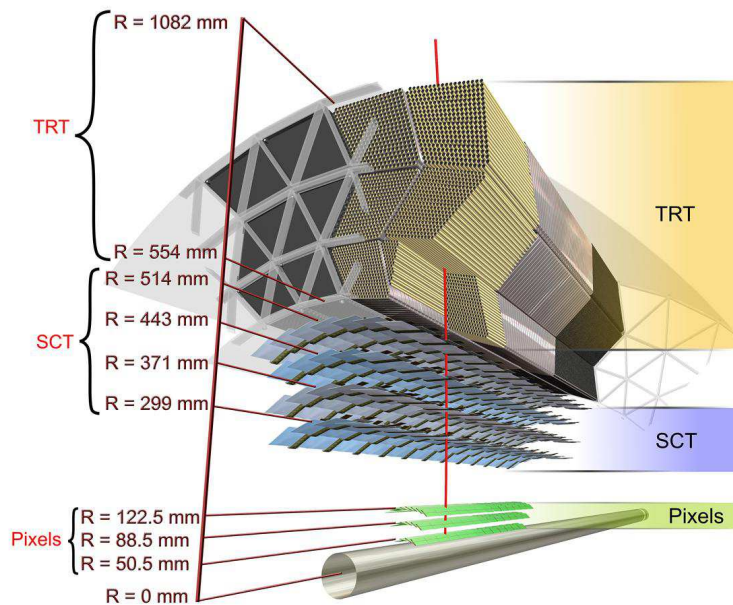


Figure 2.3: Illustration of Inner Detector. It is composed of PIXEL, SCT and TRT [19].

Semiconductor Tracker (SCT)

The SCT is located at the second innermost area of the inner detector. There are eight layers of silicon microstrip sensors. The detector uses small-angle stereo strips of 40 mrad to measure both coordinates giving four space points. The typical space resolutions of the space point are $17 \mu\text{m}$ and $580 \mu\text{m}$ in $R - \phi$ and z , respectively. The number of readout channels is 6.3 million.

Transition Radiation Tracker (TRT)

The TRT is located at the outermost area of the inner detector. The coverage is $|\eta| < 1.0$ and $1.0 < |\eta| < 2.0$ in the barrel and end-cap regions, respectively. The TRT is composed of straw-shaped drift tubes. The TRT is the detector operated using the principle of transition radiation¹. The proportional relation of the transition radiation yield to the Lorentz boost factor γ enables to identify electrons from mesons, since γ is sensitive to incident particle's mass. The straws with length of 144 cm are parallel with the beam axis in the barrel region, and the straws with length of 37 cm are aligned radially in the end-cap regions. The number of read out channels is about 351,000.

2.2.2 The Calorimeters

The calorimeters are used for the energy measurement of electrons, photons and hadrons. An illustration of the calorimeters is shown in Figure 2.4 [19]. The calorimeter should have appropriate amount of material, since the particles measured with calorimeters have to be absorbed within the calorimeter. The calorimeter system of ATLAS detector is so-called sampling type calorimeter, where the structure is composed of absorbers and sensors. The energy of particles is measured by

¹Transition radiation: The phenomena that relativistic charged particles crossing ununiform materials emit photons.

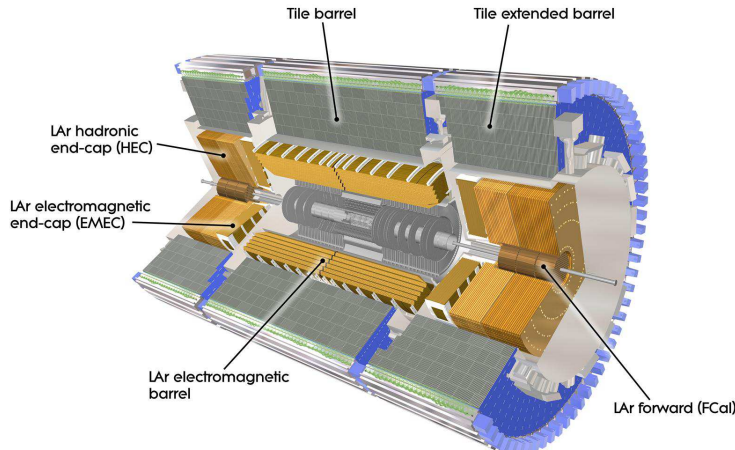


Figure 2.4: Calorimeters

sampling the particle shower generated by interaction with absorber. The calorimeter is composed of electromagnetic- and hadronic-calorimeter. These calorimeters cover the range of $|\eta| < 4.9$.

Electromagnetic Calorimeter

The EM calorimeter is a lead-LAr sampling type calorimeter, lead and liquid Argon are used for absorbers and active media, respectively. Accordion-shaped kapton electrodes are characteristic. This shape allows complete ϕ symmetry without azimuthal cracks hence producing insensitive area. The EM calorimeter is segmented in the depth direction into three sections. An illustration is shown in Figure 2.5. The EM calorimeter is classified into two parts based on the η region, barrel ($|\eta| < 1.475$) and end-cap ($1.375 < |\eta| < 3.2$) regions. The total thickness is designed as > 22 and > 24 radiation lengths (X_0) in the barrel and end-cap regions, respectively, as summarized in Table 2.2.

Table 2.2: The coverage and total thickness of EM calorimeter.

	barrel	end-cap
$ \eta $ coverage	$ \eta < 1.475$	$1.375 < \eta < 3.2$
Total thickness	$> 22 X_0$	$> 24 X_0$

Hadronic Calorimeter

The hadronic calorimeter is divided into three parts, Tile calorimeter (Tile HCAL), LAr hadronic End-cap Calorimeter (HEC) and LAr forward calorimeter (FCal).

- Tile calorimeter:
Tile HCAL is placed outside of the EM calorimeter envelope. The coverage is $|\eta| < 1.7$. The steel and scintillating tiles are used as absorbers and active media, respectively. The photomultiplier tubes are used for readout via wavelength shifting fibers coupled to scintillating tiles.

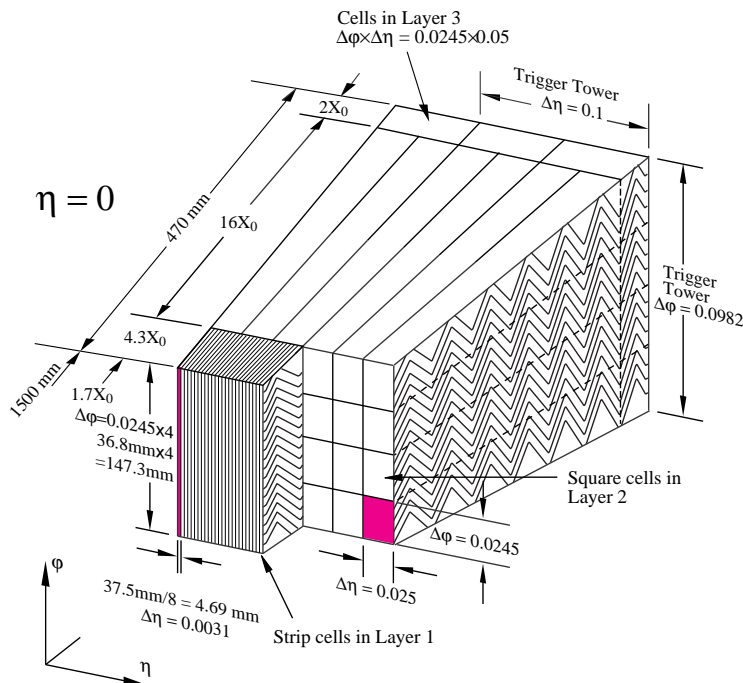


Figure 2.5: The illustration of LAr EM calorimeter. [20]

Table 2.3: The hadronic-calorimeter.

	Tile HCal	HEC	FCal
$ \eta $ coverage	$ \eta < 1.7$	$1.5 < \eta < 3.2$	$3.1 < \eta < 4.9$
absorbers	steel	copper	tungsten
active media	scintillating tile	LAr	LAr

- LAr hadronic End-cap calorimeter:
HEC is placed behind the end-cap EM calorimeter. The coverage is $1.5 < |\eta| < 3.2$. The copper is used as absorbers, and LAr is shared with EM calorimeter acting as active media.
- LAr forward calorimeter:
HEC covers higher η region, $3.1 < |\eta| < 4.9$. This enhances uniformity of full coverage of the calorimeter outermost reducing in addition background from radiations in the muon spectrometer.

2.2.3 Muon Spectrometer

The muon spectrometer measures the trajectory and momentum of the muons. The muon spectrometer is located outermost of the ATLAS detector, since muons have small interaction with materials and tiny energy loss in the calorimeters. The muon spectrometer is shown in Figure 2.6 [19]. The coverage is $|\eta| < 2.7$. The muon spectrometer is composed of three detectors, Monitored Drift Tube (MDT), Cathode-Strip Chamber, Resistive Plate Chamber (RPC) and Thin Gap Chamber (TGC). The MDT and CSC perform precise tracking measurement, and the RPC and TGC perform as trigger chamber. The muon spectrometer measures the momentum from the curvature of the track bent by toroidal magnets.

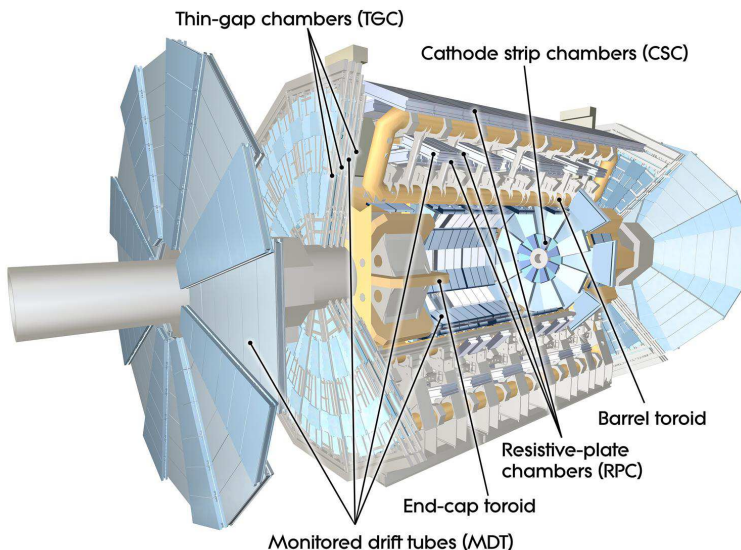


Figure 2.6: Muon spectrometer.

Monitored Drift Tube Chamber (MDT)

The MDT performs precise measurement of the track coordinates. The MDT is located in both barrel and end-cap regions, covers $|\eta| < 2.7$ ($|\eta| < 2.0$ for innermost layer). The MDT consists of drift tubes, where a mixture of Argon and the carbon dioxide with the ratio of 97 and 3 % is filled. The diameters are $30 \mu\text{m}$, $50 \mu\text{m}$ for tubes and central tungsten wires.

Cathode Strip Chambers (CSC)

Similar to MDT, the CSC gives precise tracking measurement. In the innermost layer, the count rate of MDT is exceeds its limit. The CSC is installed in the region $2.0 < |\eta| < 2.7$ replacing of MDT, because the CSC has higher rate resistance than MDT. The CSC is composed of multiwire proportional chambers with cathode strip readout. A gas mixture of Ar, CO_2 and CF_4 with the ratio of 40, 50 and 10% is filled in the CSC. The position resolution is about $60 \mu\text{m}$, and the muon momentum resolution is 2.5% at 100 GeV.

Resistive Plate Chamber (RPC)

The RPC is the detector for the triggers in the barrel region, covering the region $|\eta| < 1.05$. The fast response enables quick trigger process. The RPC is a gaseous detector utilizing as the basic unit a narrow gas gap formed by 2 mm thick two parallel resistive Bakelite plates, separated by insulating spacers. The gas $\text{C}_2\text{H}_2\text{F}_4$ with small mixture of C_4H_{10} and SF_6 is filled in the RPC.

Thin gap chamber (TGC)

The TGC is the detector for the triggers in the end-cap region, covering the region $1.05 < |\eta| < 2.7$ ($1.05 < |\eta| < 2.4$ for the triggering). TGC is multiwire proportional chambers with narrow gaps of wires and strips enabling faster response. The gaps are 1.8 mm and 1.4 mm for wire pitch and cathode-cathode distance, respectively. A gas mixture of 55% CO_2 and 45% $\text{n-C}_5\text{H}_{12}$ is filled in the TGC for the purpose of quenching.

2.2.4 The Magnets

The solenoid and toroid magnets are used in the ATLAS detector. The magnet system is shown in Figure 2.7 [21].

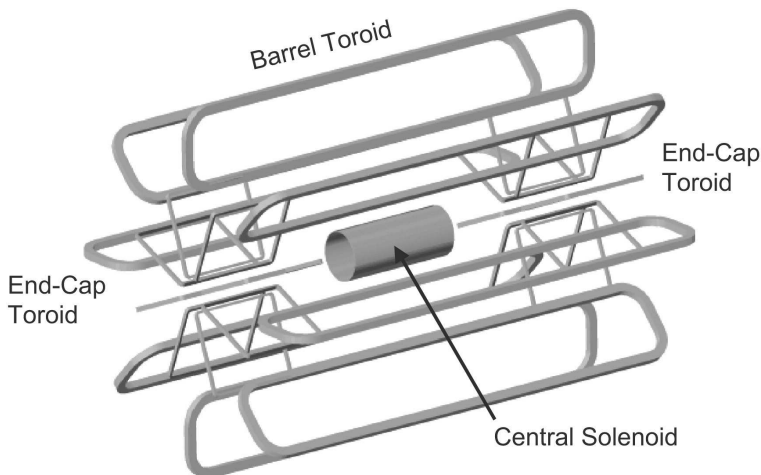


Figure 2.7: The layout of the magnet system. [22]

- The solenoid magnet:
The solenoid magnet is installed parallel to the beam axis designed to provide an axial magnetic field of 2 T for the inner detector. This strong magnetic field enables us to measure momentum of the charged particles. The material thickness is 0.66 radiation lengths, and this value is designed to be as low as possible located in front of the calorimeters for the desired calorimeter performance. The diameters of the magnet are 2.46 m (inner diameter: ID) and 2.56 m (outer diameter: OD), with the axial length 5.8 m.
- The toroid magnet:
The toroid magnets are installed outside of the calorimeters. The eight toroid magnets are aligned to be symmetry in the ϕ direction. The magnetic fields are 0.5 T and 1.0 T in the barrel and end-cap regions, respectively. The size of the toroid magnet is 25.3 m in length and the diameters are 9.4 m (ID) and 20.1 m (OD), respectively.

2.3 Trigger and Data Acquisition System

In this section, the trigger system is described. The LHC provides the pp bunch collision in 20 MHz frequency, and it is impossible to record all collision data because of limit of the computer resource. Therefore we have to select the interesting events recorded as the data by applying tight selections. This scheme is called as the trigger system. Trigger is required to decrease the event rate to 700 Hz in Run1 [32]. The trigger system is split to three levels, Level1(L1), Level2(L2) and Event Filter(EF). In order to decrease the event rate dramatically from 20 MHz to 70 kHz at L1, L1 is hardware based trigger. The Region of Interest (RoI) which is the interesting position information is defined at L1, and it is sent to L2. The more precise algorithm is applied at L2 and EF, and the rate is finally decreased to 700 Hz.

2.3.1 Lepton Triggers

In this section, the lepton triggers, electron trigger and muon trigger, are described. The lowest unrescaled single lepton trigger is used in this analysis. They are summarized in Table 2.4. The

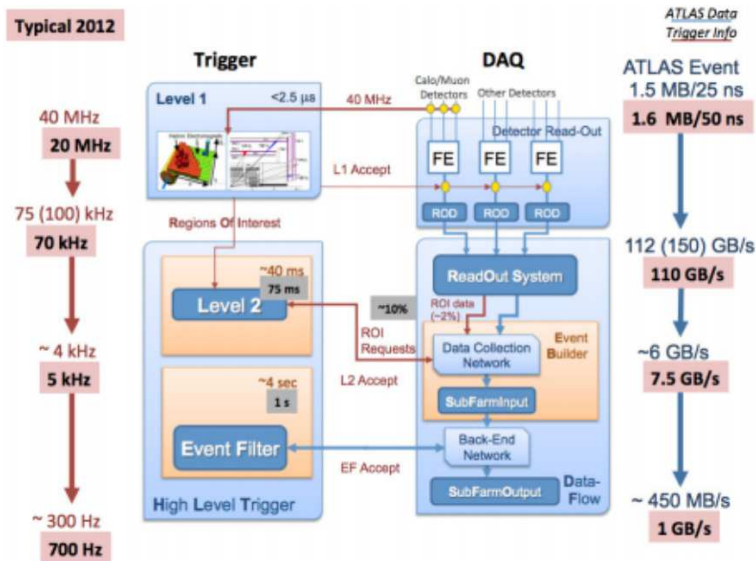


Figure 2.8: Illustration of the trigger system. [33]

thresholds of transverse momentum are 24 GeV and isolation is required for both electron and muon triggers.

Table 2.4: The single lepton trigger used for the 2012 data analysis.

	Trigger Chain	Level1 Trigger	Period
Electron	EF_e24vhi_medium1	EM18VH	A - L
Muon	EF_mu24i_tight	MU15	A - L

Electron Trigger

The events including high p_T electrons within $|\eta| < 2.5$ are acquired by the electron trigger. The trigger system is split into three levels, L1, L2 and EF.

- **Level1 Trigger:**
The hardware-based trigger is performed in L1. The trigger tower composed of electromagnetic and hadronic-calorimeters shown in Figure 2.9 are used for identification of electromagnetic objects. The granularity of the tower cells corresponds to $\Delta\eta \times \Delta\phi = 0.1 \times 0.1$. The towers measure the transverse energy E_T in the cells, and electromagnetic objects are selected if E_T sum deposited in the electromagnetic calorimeter is greater than the threshold.
- **Level2 Trigger and Event Filter:**
The L2 and EF are software-based triggers. Fast calorimeter energy and tracking reconstruction algorithms are used in L2. The calorimeter reconstruction algorithm is similar to offline algorithm, but only the highest E_T cell located in the middle calorimeter layer is used as seed cluster. The track reconstruction is performed to satisfy tighter timing requirements. The EF uses the same reconstruction algorithm as offline algorithm.

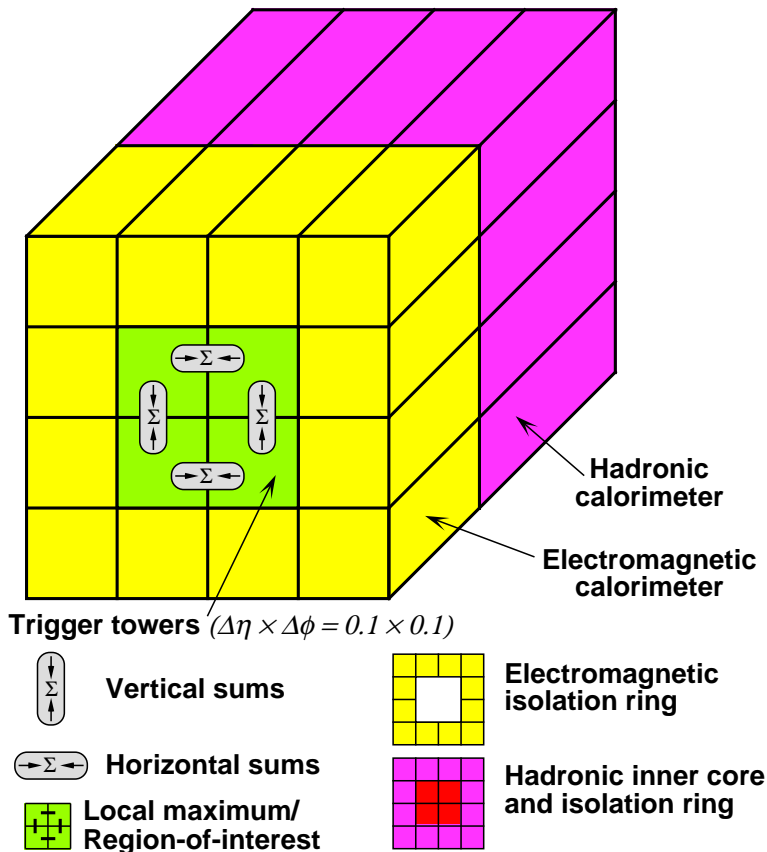


Figure 2.9: The calorimeter trigger tower. [58]

Muon Trigger

The events having high p_T muons within $|\eta| < 2.4$ are acquired by the muon trigger. Similar to the electron trigger, the trigger system is split into three levels, L1, L2 and EF.

- **Level1 Trigger:**
The hardware-based trigger is performed in L1. The hits patterns of thin gap chambers (TGC) and resistive plate chambers (RPC) shown in Figure 2.10 are used for identification of muon objects. The RPC and TGC are located in the barrel and endcap regions and the geometric coverages of the L1 triggers are about 99% and 80%, respectively. The p_T of muons are coarsely measured by the hit patterns of RPC and TGC.
- **Level2 and Event Filter:**
The software-based trigger is performed in L2 and EF. A refined algorithm is used in L2. Fast fitting is performed for the trajectory of the muon candidate within the RoI seeded by L1, and p_T is reconstructed using simple parametrised functions to achieve required resolution within the given limited short time. The L2 stand-alone-muon is combined with a track measured by inner detectors.
The EF uses the same reconstruction algorithm with isolation requirement added.

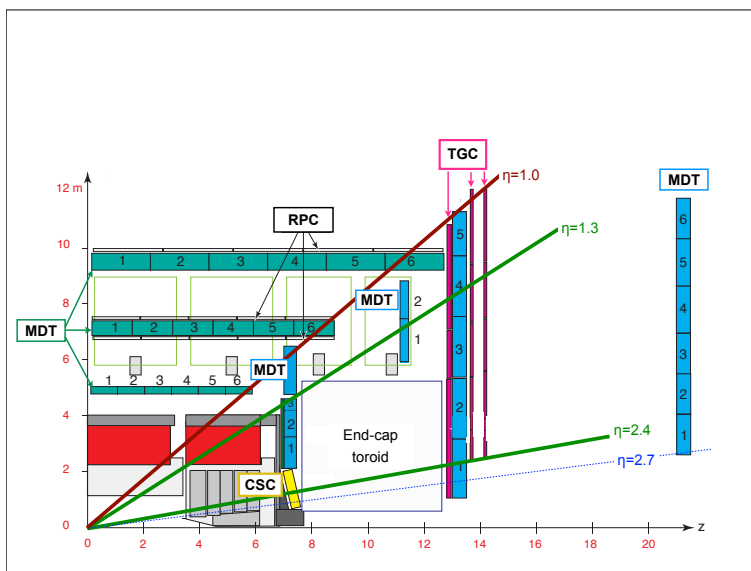


Figure 2.10: A schematic picture showing a quarter-section of the muon system. [59]

Chapter 3

Signal and Background Processes

3.1 Signal Processes

We search for the non-resonant and resonant higgs pair production. For the non-resonant search, $gg \rightarrow hh$ is shown on Figure 3.1 is considered as a signal. And the cross section of $gg \rightarrow hh$ of 9.9 ± 1.3 fb [66] is assumed in this analysis. For the resonant search, the heavy scalar H produced with the gluon fusion (ggF) is assumed to have a narrow decay width of 10 MeV which is much smaller resolution compared with experimental one. The production of H through ggF can be given by replacement of the non-resonant production Figure 3.1 (a) to the H . The standard model higgs mass of $m_h = 125.4$ GeV is assumed in this analysis. We identify di-higgs production from

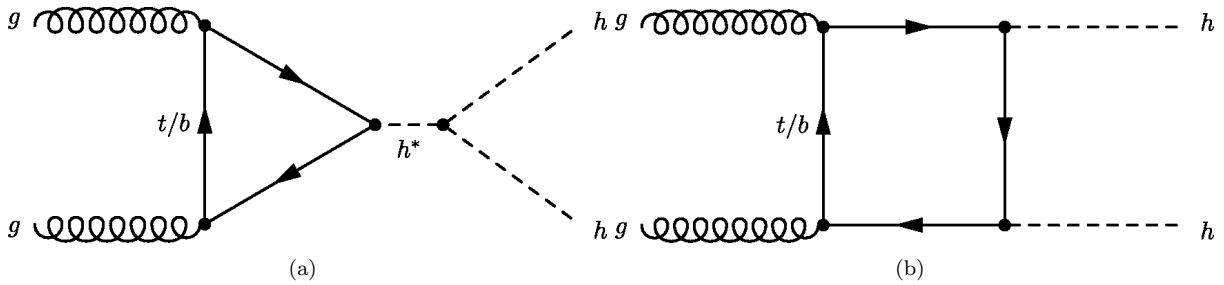


Figure 3.1: di-higgs production of leading order for non-resonant production, (a) self-coupling and (b) Yukawa coupling.

their decay into $b\bar{b}\tau^+\tau^-$ final states, with $\tau^+\tau^-$ reconstructed from lepton+hadron decay.

3.2 Background Processes

3.2.1 Single SM Higgs Production

The single higgs can be a background in this analysis. The considerable productions and higgs decay modes are ggF and vector-boson fusion (VBF) production, the single higgs production associated with vector-boson (Wh/Zh) and $t\bar{t}$ production ($t\bar{t}h$). For the decay the higgs is required to decay into τ - or b -pair except for ggF and VBF productions where the higgs is considered to decay into τ -pair, because the final state should have only one lepton in this analysis. All of these backgrounds are estimated by MC simulation.

3.2.2 Top Pair Production

Top pair production ($t\bar{t} \rightarrow W^+bW^-\bar{b}$) is one of the main backgrounds in this analysis. This process can have real Missing- E_t , electrons, muons or τ leptons in the final state if one of the W bosons decays leptonically. This is estimated from real data and MC simulation combined relying on distributions of existing real taus. The events including real τ are estimated by MC simulation. The events which do not include real τ can also contribute if a jet is mis-identified as a tau. The “jet $\rightarrow\tau$ fake factor method” described in 7.2 is used for the estimation. The contribution of mis-identified lepton events is found to be negligible, so it is not considered in this analysis.

3.2.3 Single-top Production

The contribution from single-top production via t- or s- channel production or in associated with a W boson (t-channel, s-channel and Wt production) is also estimated from mixture of fake factor method or MC simulation depending on the case that the tau candidate is real tau or fake tau of the misidentified jet. A considerable contribution is in events where an electron or muon is from W^\pm boson and tau is a mis-identified jet or another leptonic decay of associated W boson in Wt production.

3.2.4 $Z^0 \rightarrow \tau^+\tau^- + \text{jets}$ Production

The estimation of $Z^0 \rightarrow \tau^+\tau^- + \text{jets}$ is a key point of this analysis because this process is one of the main backgrounds. The event yield of $Z + \text{jets}$ MC simulation was normalized to the data in control region (CR). The signal contamination in the CR was estimated carefully because of large branching ratio of $h \rightarrow \tau^+\tau^-$. Therefore a data driven method was developed where $Z^0 \rightarrow \mu^+\mu^-$ data distribution was used in this method. This process is well understood, signal-free environment is obtained owing to small rate of $h \rightarrow \mu^+\mu^-$ and kinematics in similar to $Z^0 \rightarrow \tau^+\tau^-$ except for the difference in mass of muon and tau. The muons of $Z^0 \rightarrow \mu^+\mu^-$ events are replaced to simulated τ leptons with an embedding technique described in 4.3.

3.2.5 $Z^0 \rightarrow e^+e^-/\mu^+\mu^- + \text{jets}$ Production

$Z^0 \rightarrow e^+e^-/\mu^+\mu^- + \text{heavy flavor events}$ are considered as background process. In the case where one of the charged leptons associated jets is mis-identified as a hadronic- τ , the event is regarded as background. MC simulation is performed for the estimation of this background.

3.2.6 Di-boson Production

The production of pair of vector bosons, ZZ , WW and WZ can be background. In the case of ZZ , it has the same final state as signal $b\bar{b}\tau^+\tau^-$ if one of Z^0 bosons decays into b pair and another decays into τ pair. In case of WW and WZ , they can be background if the events have one or two fake light lepton, fake τ and b -jets. The MC simulation is performed for the estimation of this background.

3.2.7 $W(\rightarrow e\nu/\mu\nu) + \text{jets}$ Production

The production of W^\pm boson associated with jets is a significant background source, because of large cross section. In this process, light lepton from W^\pm boson decay, and jets mis-identified as a hadronic- τ are the background source. “fake factor method” is used for the estimation.

3.2.8 QCD-jet Production

QCD jets process can contribute as background, because of the large cross section. If one of the QCD jets is mis-identified as a light lepton (e or μ) and another jets is mis-identified as a hadronic- τ , it can be background. The leptons also can come from semi-leptonic decays of B and D hadrons. The “fake factor method” is used for the estimation.

Chapter 4

Monte Carlo Simulation Samples and ATLAS Data

This section describes the data collected with the ATLAS detector and Monte Carlo (MC) simulation samples.

4.1 ATLAS Data

The data used in this analysis were collected in 2012 with the ATLAS detector at the LHC in $\sqrt{s} = 8$ TeV proton-proton collision. The integrated luminosity corresponds to 20.3 fb^{-1} , where only good condition data which were recorded while all detector systems including LHC operated well, were included.

4.2 Monte Carlo Samples

In this section, MC samples are summarized for signal and background processes. The list of event generators are listed in Table 4.1.

4.2.1 Signal Samples

MADGRAPH5 [23] is used for both non-resonant and resonant di-higgs production. The SM DiHiggs model [24, 25] and the HeavyScalar model [26] are used for the non-resonant and resonant models, respectively. With the mass of SM higgs $m_h = 125$ GeV, its decay products were filtered to be only b -quarks and tau leptons pairs. For the resonant production, the decay width of heavy scalar H is set to 10 MeV which is much smaller than the experimental mass resolution and the setting is considered as arbitral.

4.2.2 Background Samples

- single higgs

The ggF and VBF productions are generated by POWHEG generator which calculates up to next-to-leading order (NLO) in QCD corrections. These samples include finite bottom and top-quark masses [27]. The calculated transverse momentum spectrum at next-to-next-to-leading order (NNLO) and next-to-next-to-leading logarithm (NNLL) in QCD corrections are used for higgs transverse momentum for ggF [28] Wh , Zh and $t\bar{t}h$ productions are generated by PYTHIA8 generator.

- electroweak
 Z +jets are generated by ALPGEN. $t\bar{t}$, single-top (s-channel, Wt) and di-boson are generated by POWHEG. single-top(t-channel) is generated by AcerMC. PYTHIA8 is used for parton showers, hadronization and underlying-event simulation. CT10 [29] and CTEQ6L1 [30] are used for parton distribution functions (PDFs).

Table 4.1: List of MC generators and parton distribution functions used for the signal and background processes. The light Higgs boson h is assumed to have a mass of 125.36 GeV.

Process	Event generator	PDF set
Background processes		
W/Z +jets	AlpGen + Pythia8	CTEQ6L1
Diboson: WW , WZ and Z^0Z	Powheg + Pythia8	CT10
$t\bar{t}$	Powheg + Pythia8	CT10
Single top: t -channel	AcerMC + Pythia8	CTEQ6L1
Single top: s -channel	Powheg + Pythia8	CT10
Single top: Wt	Powheg + Pythia8	CT10
$gg \rightarrow h$	Powheg + Pythia8	CT10
$qq \rightarrow qqh$	Powheg + Pythia8	CT10
$qq \rightarrow Vh$	Pythia8	CTEQ6L1
$qq/gg \rightarrow t\bar{t}h$	Pythia8	CTEQ6L1
Signal processes		
Non-resonant $gg \rightarrow hh$	MadGraph5 + Pythia8	CTEQ6L1
Resonant $gg \rightarrow H \rightarrow hh$	MadGraph5 + Pythia8	CTEQ6L1

4.3 Sample for $Z^0 \rightarrow \tau^+\tau^-$ Estimation

In embedding method [31], muons in $Z^0 \rightarrow \mu^+\mu^-$ data are replaced with simulated τ leptons. The τ -lepton kinematics are inherited from measured muon distributions and the τ decays are forced using the MC simulation.

4.3.1 $Z\mu^+\mu^-$ Event Selection

The $Z^0 \rightarrow \mu^+\mu^-$ data are selected by following selection.

- trigger: di-muon trigger with p_T threshold of 18 and 8 GeV and single muon trigger with p_T of 24 GeV.
- two muons: require exactly two muons as defined in Section 5.2.

- muon p_T : $p_T^\mu > 25$ GeV

- track isolation: track isolation of $\sum_{\text{tracks}}^{\Delta R \leq 0.2} p_{T,\text{track}}/p_{T,\mu} < 0.2$

- invariant mass of muons: $m_{\mu^+\mu^-} > 40$ GeV

Subtraction $t\bar{t}$ Contamination from Embedding Sample

The di-muon events selected as $Z^0 \rightarrow \mu^+\mu^-$ contain certain background, even if event selections described in 4.3.1 are applied. After all event selection applied as detailed in Section 6.3, $t\bar{t}$ contamination is not negligible, because one or two b -tagged jets are required in the event selection. The contamination is 2.3% and 26.6% for one and b -tagged jet(jets) categories described in Section 6.2, respectively. The details are described in Appendix B.

Chapter 5

Object Reconstruction and Identification

Particles are detected and measured by the detectors described in Section 2.2. These detector responses are used for the reconstruction and identification for the physics objects. The overview for them are described in this section.

5.1 Electron

5.1.1 Reconstruction

Electrons are reconstructed from energy clusters, measured by the electromagnetic calorimeter, associated with matched tracks in the inner detector.

The seed clusters with transverse energy of $E_T > 2.5$ GeV is searched by a sliding-window algorithm [34]. The window size used in the algorithm is 3×5 units with one unit corresponding to the middle layer granularity of 0.025×0.025 in the $\eta \times \phi$ space.

A loose track matching is performed as a next step. The reconstructed tracks in the inner detector with $E_T > 1$ GeV is extrapolated to the middle layer of the EM calorimeter and checked if it matches to the seed clusters with a loose threshold. The difference in the η direction between the track and the cluster position, $\Delta\eta$, is required as $|\Delta\eta| < 0.05$. The cluster is identified as an electron candidate, if at least one track is matched to the seed cluster. If several tracks are matched to the same cluster, such information of ϕ direction is also used, where the one with smallest ΔR , defined as $\Delta R = \sqrt{(\Delta\eta)^2 + (\Delta\phi)^2}$, is chosen. The electron tracks are refitted by an optimized electron track fitter with Gaussian Sum Filter algorithm [35] which is a non-linear generalization of the Kalman filter [36], after the loose track matching is applied, to achieve precise tracking in shorter calculation time.

The electron cluster is rebuilt within 3×7 (5×5) lateral towers in the barrel (end-cap) region to determine the cluster energy where four contributions are taken into account: energy deposit in the material in front of the EM calorimeter, energy deposit in the cluster, external energy deposit outside the cluster (lateral leakage) and energy deposit beyond the EM calorimeter (longitudinal leakage).

The information of both the final cluster and the best track matched to the seed cluster is used for the final calculation of the electron four momenta. Namely the energy and direction of the electron are given by the cluster energy and the track, respectively.

5.1.2 Identification

Certain contamination of fake electrons arises from hadrons, photon conversions and semi-leptonic decays of heavy flavors. In order to suppress such contamination, further electron identification is performed. The shower shape, strip layer, track quality and cluster-track matching variables are effective information to separate the fake contamination with real electrons. Loose, medium and tight working points are defined based on the identification efficiencies. The efficiencies are 95, 85 and 75 % for loose, medium and tight working points, respectively. The identification efficiencies measured using a tag-and-probe method [37] applied for $Z^0 \rightarrow e^+e^-$ and $J/\psi \rightarrow e^+e^-$ events are shown in Figure 5.1.

5.1.3 Energy Scale and Resolution

In order to correct for residual differences between MC and data distributions, the corrections on the electron energy scale and resolution, are evaluated. The energy scale corrections are derived by:

$$E^{\text{data}} = E^{\text{MC}}(1 + \alpha_i) \quad (5.1)$$

where E^{data} and E^{MC} are corresponding electron energies in the data and MC, α_i is the deviation from the optimal calibration, and i represents the electron η region bin. The energy resolution corrections are derived by:

$$\left(\frac{\sigma_E}{E}\right)^{\text{data}} = \left(\frac{\sigma_E}{E}\right)^{\text{MC}} \oplus c \quad (5.2)$$

The χ^2 minimization in two-dimensional parameters scan (α , c) gives the optimal value of α and c . The obtained α and c are shown in Figure 5.2. The $m_{e^+e^-}$ distribution after the corrections are shown in Figure 5.3. The total uncertainties in the energy scale and energy resolution are $<0.05\%$ and $<0.5\%$, respectively.

5.1.4 Object Selection

Electron candidates passing the following selections are defined as electron object.

- transverse momentum: $p_T > 15$ GeV
- pseudorapidity: $|\eta| < 1.37$ or $1.52 < |\eta| < 2.47$
- isolations:
 - calorimeter isolation
This requires that energy deposit in the electromagnetic and hadronic calorimeters in $\Delta R \equiv \sqrt{(\Delta\eta)^2 + (\Delta\phi)^2} = 0.2$ around the electron is less than 6% of the track p_T of the electron.
 - track isolation
This requires that sum of the p_T of additional tracks which have $p_T > 1$ GeV in $\Delta R = 0.4$ is less than 6% of the track p_T of the electron.

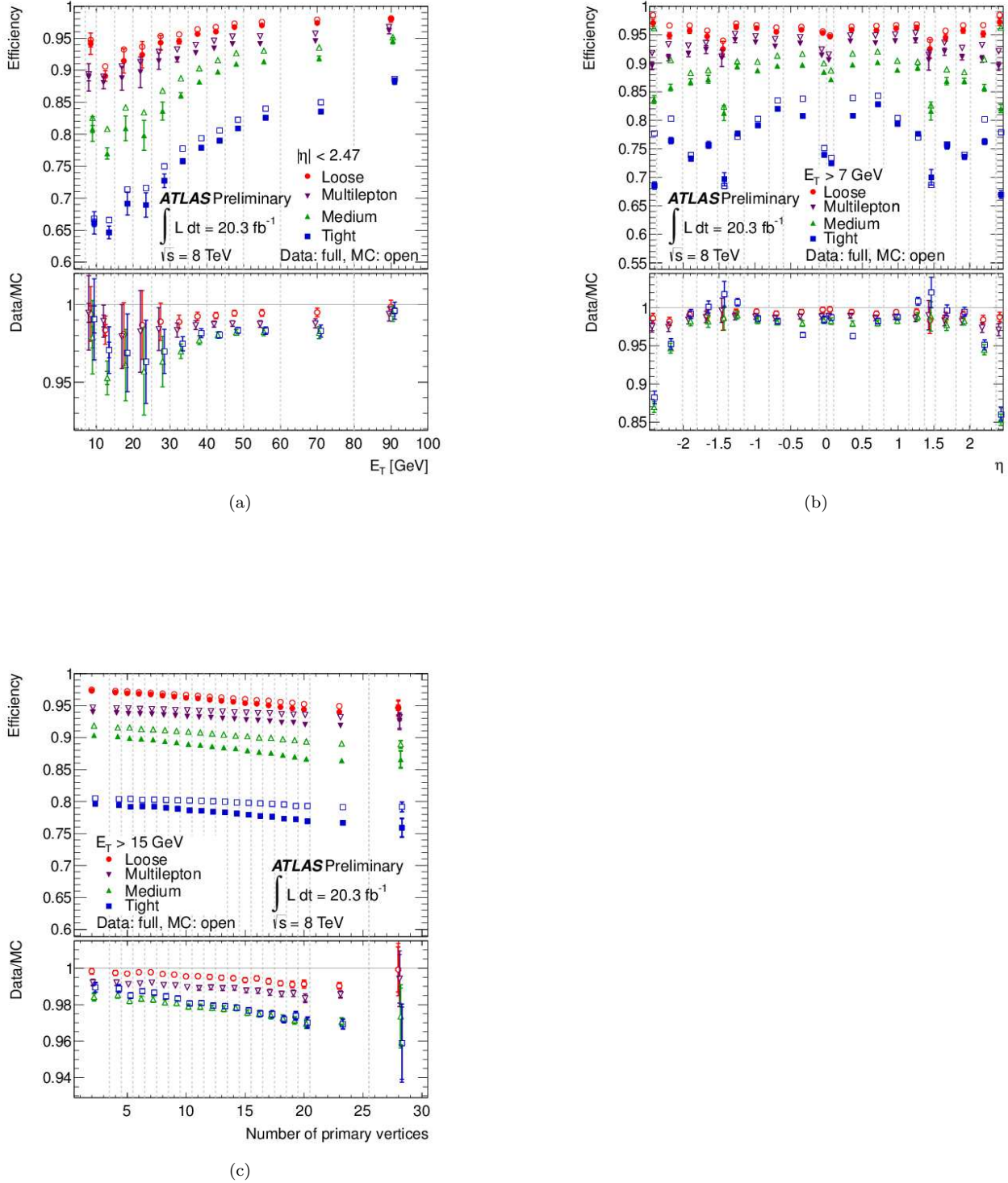


Figure 5.1: Electron identification efficiencies for each working point [38], calculated as function of (a) electron E_T , (b) electron η , and (c) number of event vertices. The data (full marks) and MC (open marks) are compared.

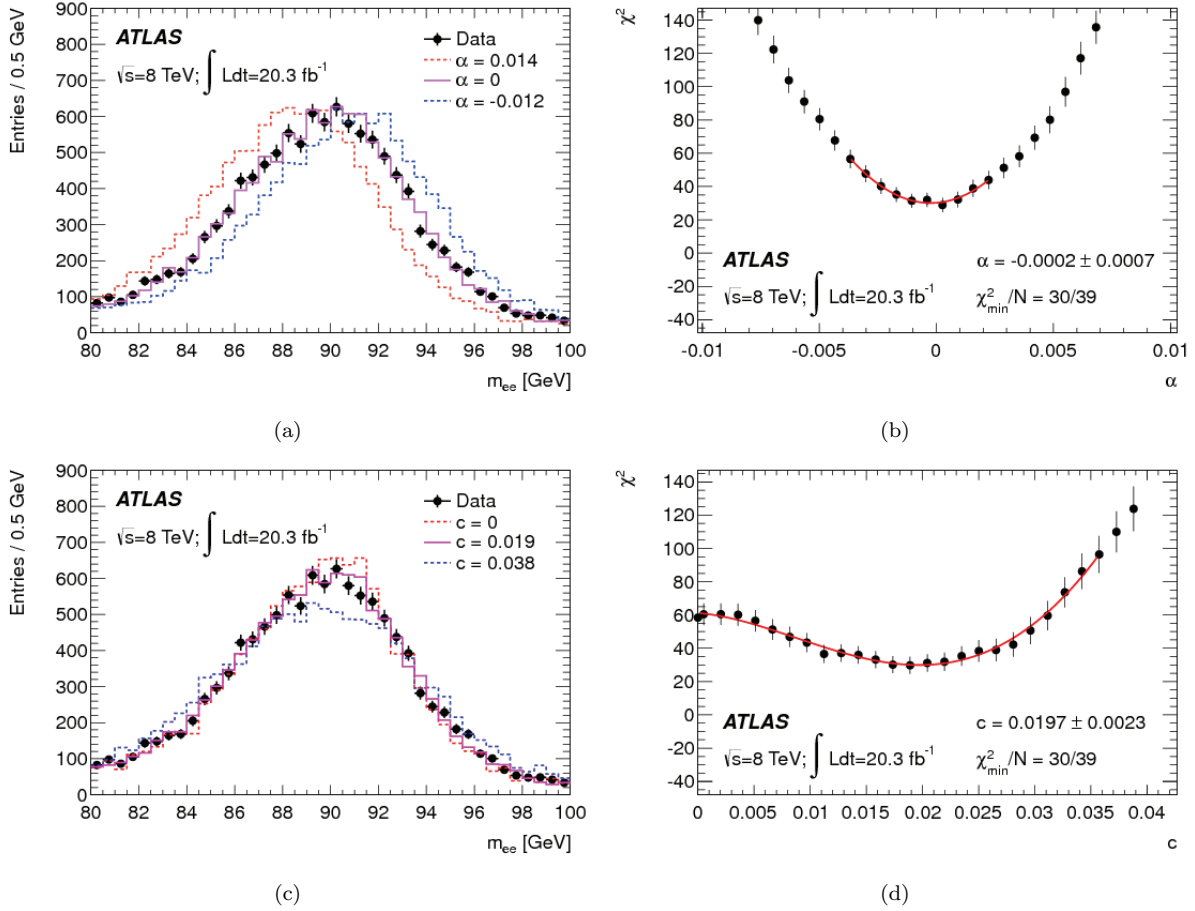


Figure 5.2: The invariant mass distribution $m_{e^+e^-}$ in $Z^0 \rightarrow e^+e^-$ events, compared to MC templates. The templates of $m_{e^+e^-}$ for different, (a) α values, and (c) c values. The χ^2 distributions as a function of, (b) α , and (d) c .

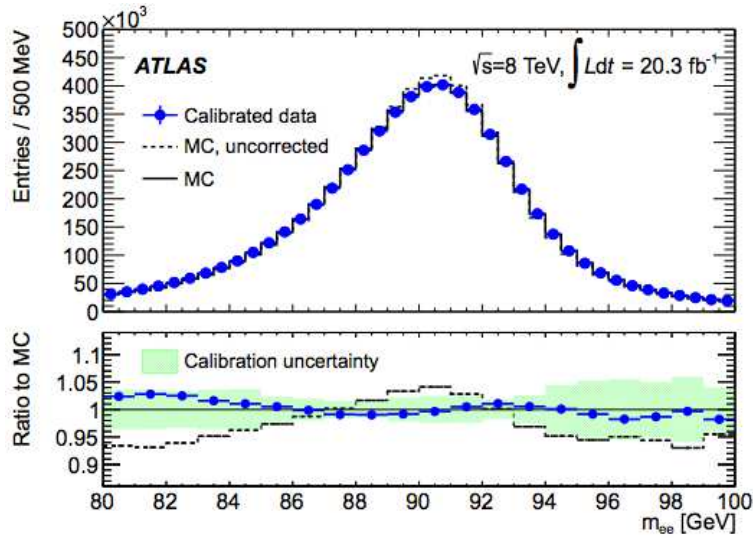


Figure 5.3: Top: Invariant mass distribution of di-electron in $Z^0 \rightarrow e^+e^-$. Calibrated data (blue point), uncorrected MC (dashed black line), and MC (solid black line) are shown. Bottom: Ratio of the "data/MC" and "uncorrected MC/MC" [39].

5.2 Muon

5.2.1 Reconstruction and Identification

Four type of muons, combined, stand-alone, segment tagged and calorimeter tagged muons.

- **Combined Muons (CB):**
Independent track reconstructions in inner detector and muon spectrometer are performed. In the case, a track measured in muon spectrometer is extrapolated and matched to a track measured in the inner detector, then it is reconstructed as Combined Muons shown in Figure 5.4 (a) [40]. Combined muon objects are most pure objects. CB is used for both physics analysis and overlap removal.
- **Segment Tagged Muons (ST):**
In the case, muon spectrometer measures at least one hits, and it is matched with a track extrapolated from inner detector, then it is reconstructed as a Segment Tagged muon, shown in Figure 5.4 (b) [40]. This allows to recover reconstruction efficiencies. ST is only used for object overlap removal.
- **Stand-Alone Muons (SA):**
In the case, a track reconstructed in the muon spectrometer but not reconstructed in the inner detector, then it is reconstructed as a Stand-Alone Muons, shown in Figure 5.4 (c) [40]. In order to use only high purity muon, SA is not included in this analysis.
- **Calorimeter Tagged Muons (CT):**
In the case, energy deposit in the calorimeter of a track reconstructed in the inner detector is compatible, then it is reconstructed as Calorimeter Tagged Muons, shown in Figure 5.4 (d) [40]. In order to use only high purity muon, CT is not included in this analysis.

The efficiencies are evaluated by tag-and-probe method using $\mu^+\mu^-$ events of data. The efficiency of CB muon is shown in the Figure 5.5.

5.2.2 Momentum Scale and Resolution

Since MC includes the best configuration of the detector geometry and material distribution, the corrections are needed. The large amount of data $Z^0 \rightarrow \mu^+\mu^-$, $J/\psi \rightarrow \mu^+\mu^-$ and $\Upsilon \rightarrow \mu^+\mu^-$ are used for the calibration of momentum scale and resolution. The di-muon mass resolution $\sigma(m_{\mu^+\mu^-})$ is given as:

$$\frac{\sigma(m_{\mu^+\mu^-})}{m_{\mu^+\mu^-}} = \frac{1}{2} \frac{\sigma(p_1)}{p_1} \oplus \frac{1}{2} \frac{\sigma(p_2)}{p_2} = \frac{1}{\sqrt{2}} \frac{\sigma(p)}{p} \quad (5.3)$$

where p_1 and p_2 correspond to the momenta of two muons. The mass scale and resolution are given by fitting of the invariant mass distributions. The distribution of mass of $Z^0 \rightarrow \mu^+\mu^-$ is shown in Figure 5.6. The Figure 5.7 and Figure 5.8 show the data/MC ratio of mass scale and resolution obtained from $Z^0 \rightarrow \mu^+\mu^-$, $J/\psi \rightarrow \mu^+\mu^-$ and $\Upsilon \rightarrow \mu^+\mu^-$ [41]. This factors estimated from this are applied to MC simulation samples. The systematic uncertainties are around 0.2% depending on the muon pseudorapidity.

5.2.3 Object Selection

Muons candidates passing following selections are defined as muon object.

- transverse momentum $p_T > 10$ GeV
- pseudorapidity $|\eta| < 2.5$

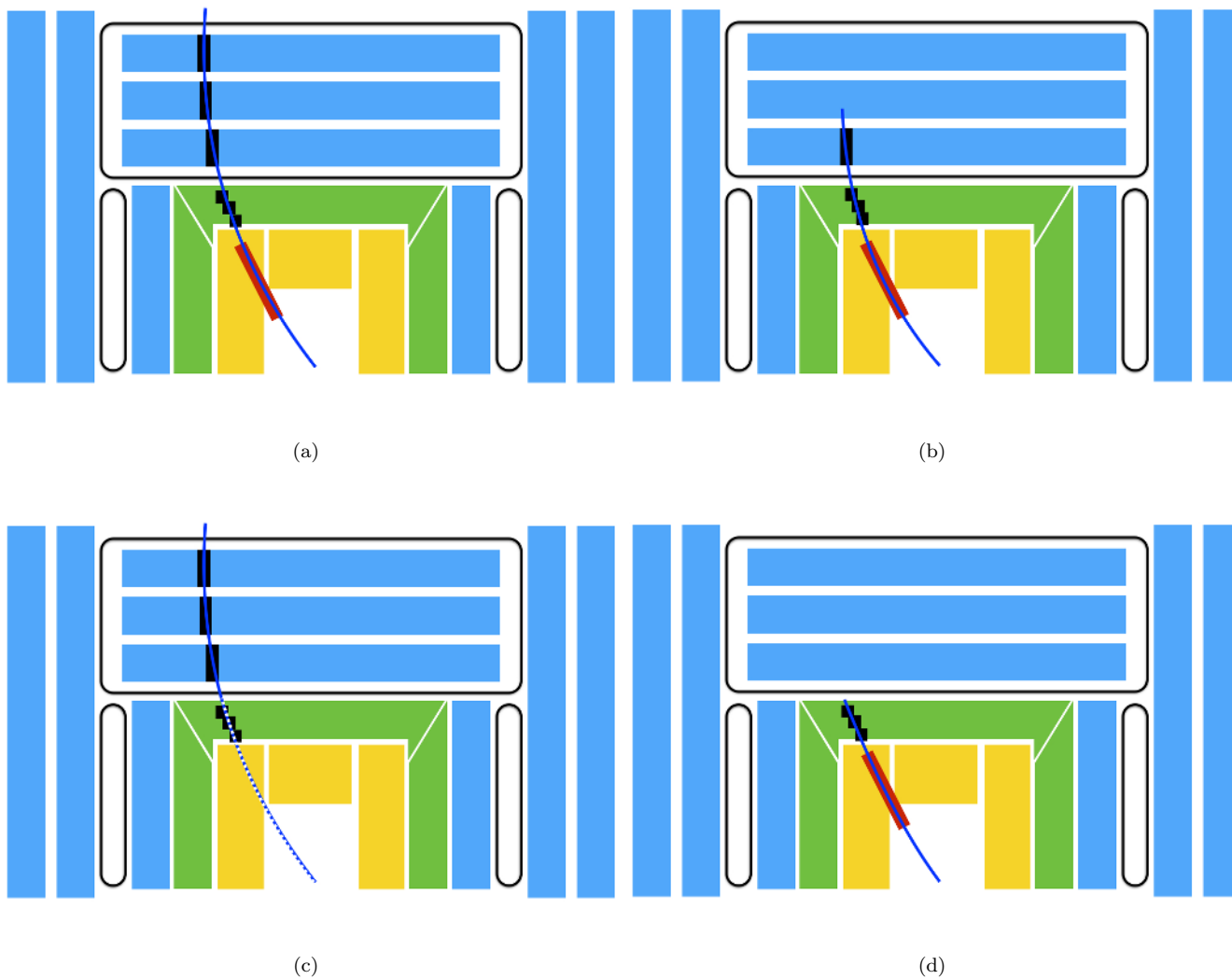


Figure 5.4: Muon reconstruction by (a) Combined, (b) Segment-Tagged, (c) Stand-Alone, and (d) Calorimeter Tagged Muons.

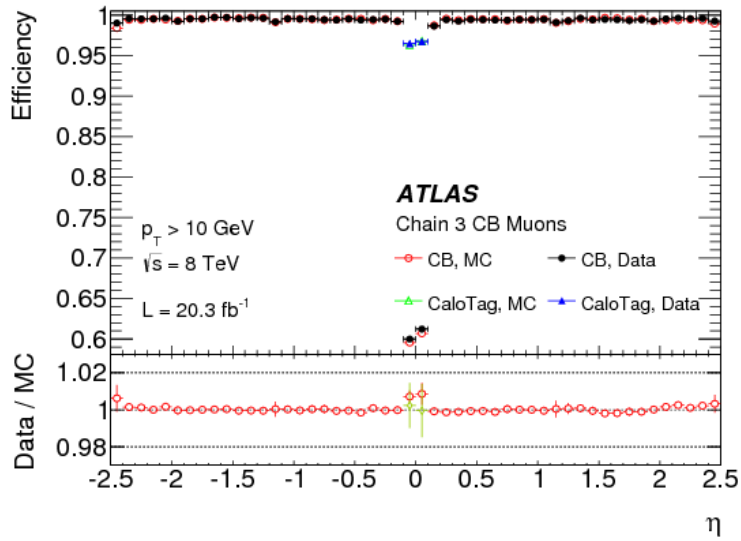


Figure 5.5: Efficiency of CB muon, measured with tag-and-probe method using $Z^0 \rightarrow \mu^+\mu^-$ events, as a function of pseudorapidity [40].

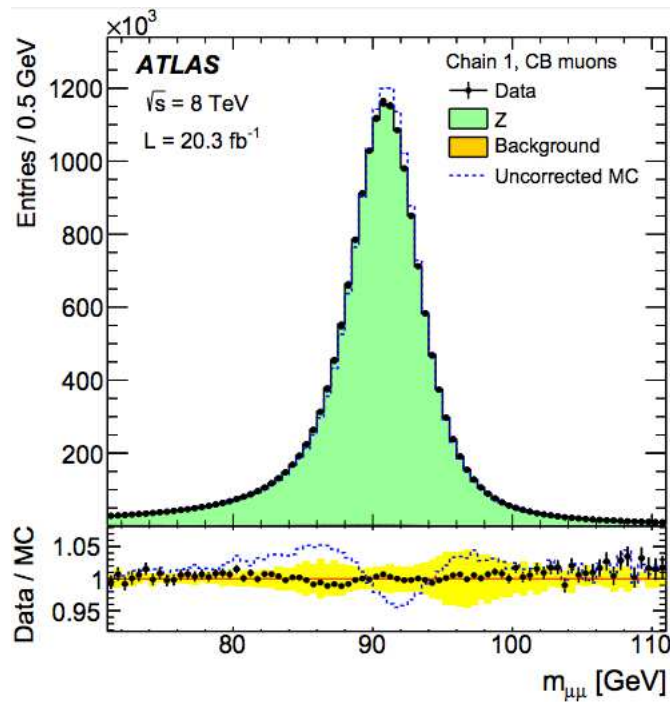


Figure 5.6: Resonant mass of $Z^0 \rightarrow \mu^+\mu^-$ reconstructed with Combined Muon. [41]

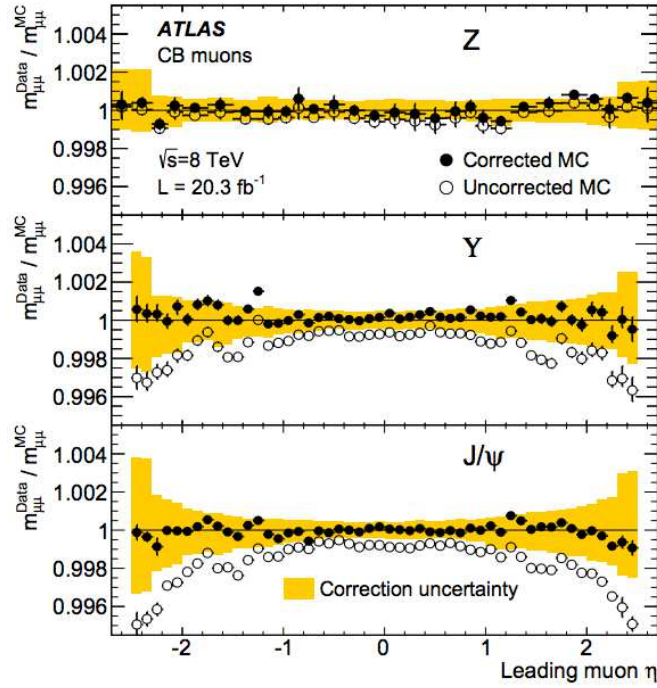


Figure 5.7: Ratio data/MC of the fitted mean mass $\langle m_{\mu^+\mu^-} \rangle$ in (Top) $Z^0 \rightarrow \mu^+\mu^-$, (Middle) $\Upsilon \rightarrow \mu^+\mu^-$, and (Bottom) $J/\psi \rightarrow \mu^+\mu^-$. [41]

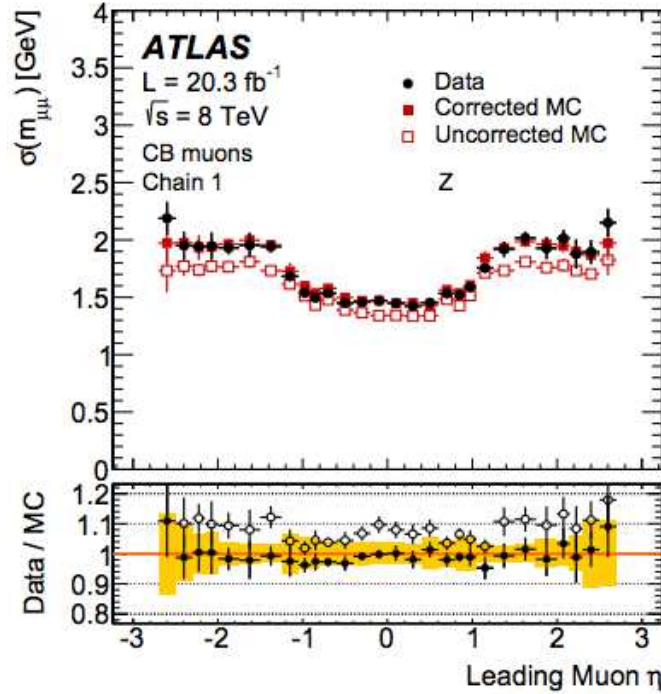


Figure 5.8: Dimuon invariant mass resolution for CB muons for $Z^0 \rightarrow \mu^+\mu^-$ as a function of leading muon η . [41]

defined as the position of center of gravity weighed by the cell energies. The mass of the cluster is defined as zero.

anti- k_T algorithm

The following parameter d_{ij} is introduced:

$$d_{ij} = \min(k_{t,i}^{2p}, k_{t,j}^{2p}) \frac{\Delta R_{ij}^2}{R^2} \quad (5.4)$$

$$d_{iB} = k_{t,i}^{2p} \quad (5.5)$$

where $k_{t,i}$ is transverse energy of the topological cluster i , \min is a function choosing a smaller value from two values in the brackets, and ΔR_{ij} corresponds to the distance of two clusters i and j defined as $\Delta R_{ij} = \sqrt{(\eta_i - \eta_j)^2 + (\phi_i - \phi_j)^2}$. R is a constant value and represents the jet cone size which is used in the algorithm. The jet cone size $R = 0.4$ is used in this analysis. p is another constant value: the jet reconstruction is split into several algorithms based on this value. The $p = 1, 0, -1$ correspond to k_T , Cambridge/Aachen and anti- k_T algorithms, respectively. The $p = -1$, anti- k_T is adopted in this analysis.

1. d_{ij} and d_{iB} are calculated for each pair of clusters i and j where B is the beam direction.
2. The minimum d_{\min} is searched from all the d_{ij} and d_{iB} . If a d_{ij} is chosen as a d_{\min} , the clusters i and j are merged and they are treated as single cluster. On the other hand, if a d_{iB} is picked up as d_{\min} then the cluster i is defined as a jet and removed from the list.
3. The processes 1 and 2 are repeated until all clusters are removed from the list.

One feature of anti- k_T is that high p_T clusters have higher priority in examination. This results in the better jet cone shape which is one of the advantages of the anti- k_T algorithm. The Figure 5.10 shows the example results of different jet algorithms, k_T , Cambridge/Aachen and anti- k_T algorithms.

5.3.2 Energy Scale and Resolution

The scheme of jet energy calibration is shown in Figure 5.11. First the vertex is modified to the “first primary vertex” which is defined by that which has the highest Σp_T^2 of tracks (with $p_T > 400$ MeV) associated with it, and next pile-up effect is removed. Then the jet energy is calibrated by applying the jet energy scale (JES) which is derived as a correction of the fraction of the reconstructed jet energy to the truth jet energy. The local cluster weighting (LCW) method is performed for energy corrections [47]. The calibration has η dependence, therefore it is derived in each η region. Figure 5.12 shows the average energy response for the LCW scale. And Figure 5.13 shows the jet energy p_T response plots after applying the JES calibration. The good agreement can be seen for η function, however there is some difference for p_T function. In order to improve this difference, further corrections “Global Sequential Correction” are applied [48]. The residual in-situ calibration is performed as the final stage of the calibration. The in-situ techniques use γ +jet, Z^0 +jets and di-jets events and see the balance of p_T between the objects and a recoiling jet in the transverse plane. The p_T of reference objects and a jet are compared in both data and MC simulation, and following quantity is defined as a residual correction.

$$\frac{\mathcal{R}_{\text{data}}}{\mathcal{R}_{\text{MC}}} = \frac{\langle p_T^{\text{jet}} / p_T^{\text{ref}} \rangle_{\text{data}}}{\langle p_T^{\text{jet}} / p_T^{\text{ref}} \rangle_{\text{MC}}} \quad (5.6)$$

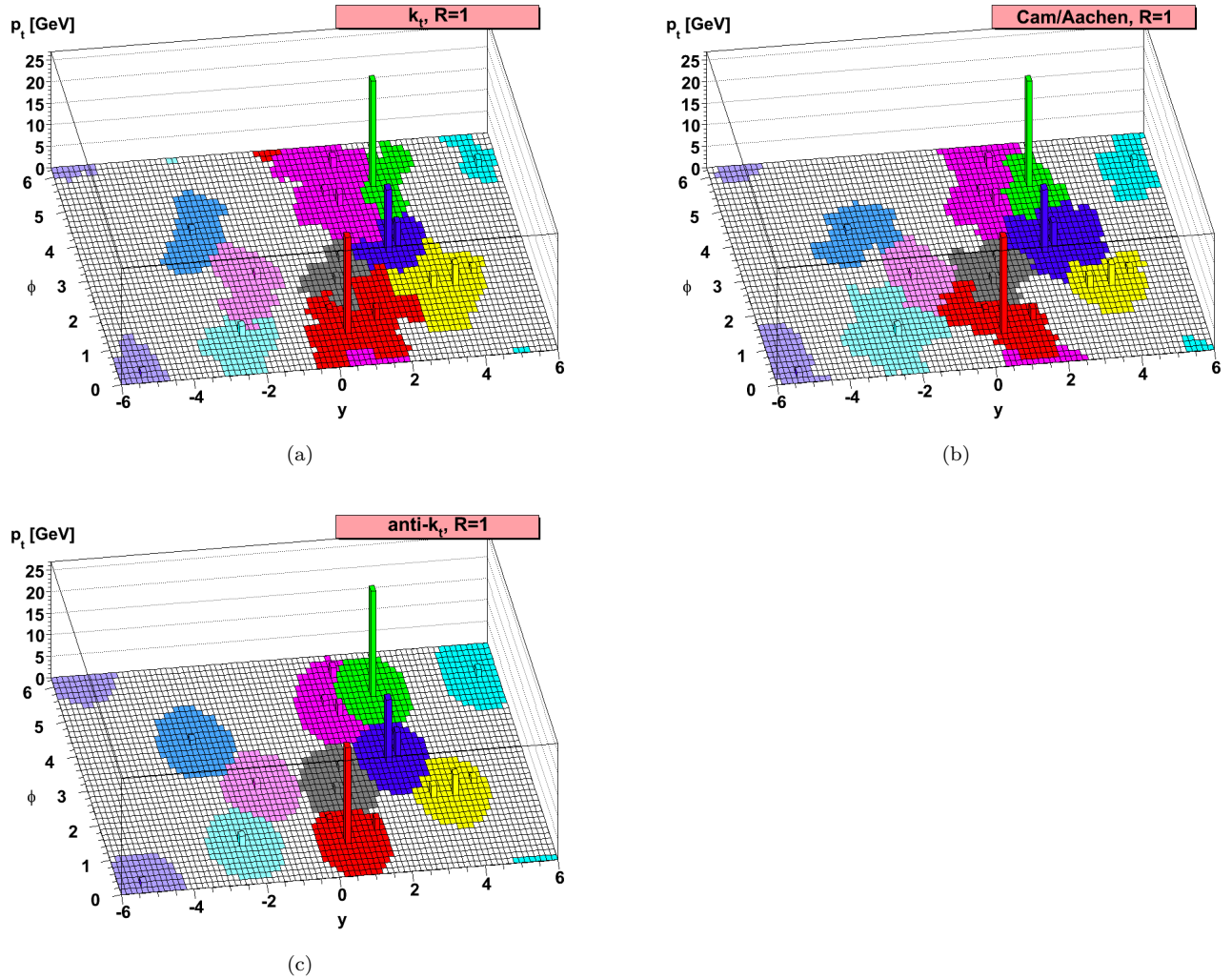


Figure 5.10: The jet reconstructions with (a) k_T , (b)Cambridge/Aachen and (c)anti- k_T are shown for the parton-level event generated with 10^4 soft “ghosts”. [44]

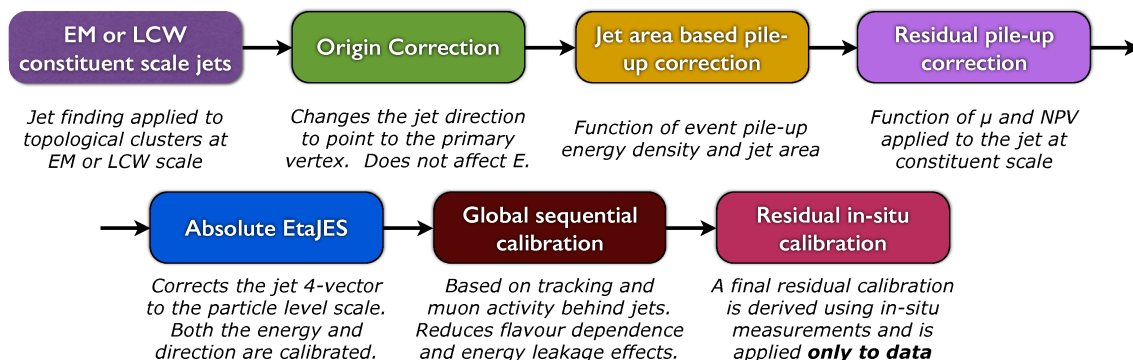
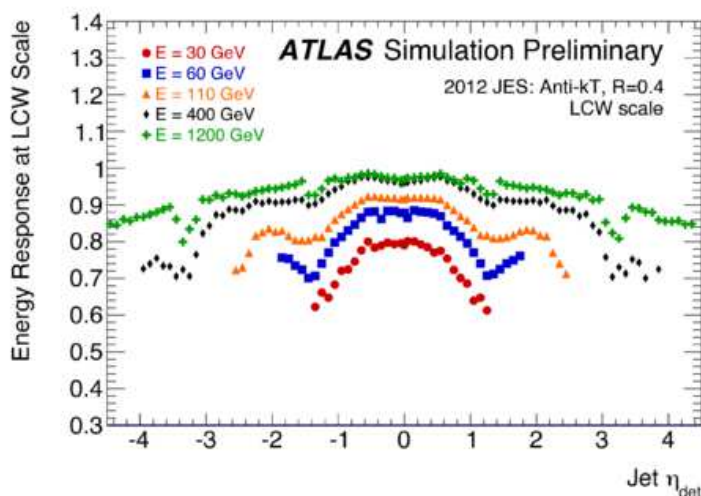


Figure 5.11: The scheme of calibration of the LCW jet. [46]


 Figure 5.12: Energy response as a function of η for LCW scale. [46]

Firstly, di-jet events are used for intercalibration for η in which the average p_T for forward jets is equalised to the p_T of balancing jets in the central region. The relative jet response which is defined as Equation 5.6 is shown in Figure 5.14. The Z^0 +jet and γ +jet used to derive in-situ JES correction for jets. Figure 5.15 shows the results of Z^0 +jet, γ +jet and di-jet balance studies. The difference of the response in MC and data is within 1% level.

5.3.3 b -Jets Identification

B hadrons have a long life time, therefore they can travel for a distance of $c\tau \approx 450 \mu\text{m}$ in the rest frame before their decay. “MV1” tagger is used for the b -tagging in this analysis. First the impact parameter (IP) is introduced as a ingredient used in the MV1 tagger.

Impact parameter:

IP is the distance of closest approach of the track to the primary vertex. The illustration is shown in Figure 5.16. The tracks from b -jets tends to have large IPs. IP is defined in directions on the transverse plane and along with z -axis, and named with d_0 , z_0 and $z_0 \sin \theta$. d_0 is the IP in the $r - \phi$, z_0 is the coordinate along the z -axis of the point of closest approach, and $z_0 \sin \theta$ stands for

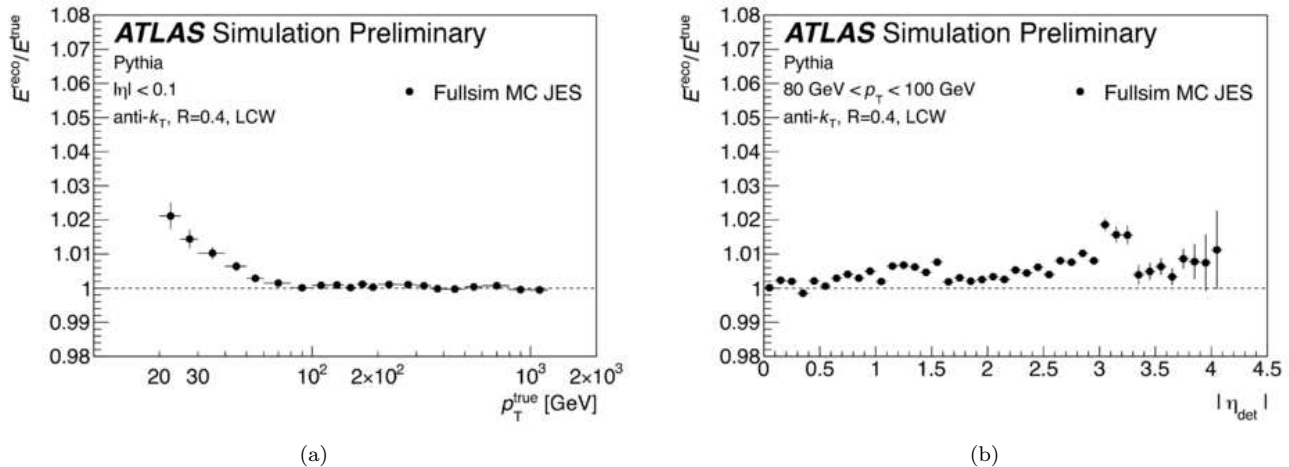


Figure 5.13: The energy response after applying JES calibration as a function of jet (a) p_T and (b) η [46].

the longitudinal IP. To evaluate the IP, so called IP significance is defined as

$$\frac{d_0}{\sigma(d_0)} = \frac{d_0}{\sqrt{\sigma^2(d_0^{\text{track}}) + \sigma_{\text{PV}}^2}}, \quad (5.7)$$

where $\sigma(d_0^{\text{track}})$ is the IP resolution, and σ_{PV}^2 represents the uncertainty of primary vertex reconstruction.

MV1 is an artificial Neural Network combination variable of the “IP3D”, “SV1” and “JetFitter” algorithms.

- IP3D algorithm:
 - The signed transverse IP significance $d_0/\sigma(d_0)$ and signed longitudinal IP significance $z_0/\sigma(z_0)$ are used for the IP3D algorithm. The information are combined.
- SV1 algorithm:
 - The combined information of:
 - The invariant mass of all tracks associated to the secondary vertex
 - The ratio of the sum of the track energies between the vertex of one coming from the secondary vertex and all the tracks in the jet.
 - The number of vertices in the jet.
 - The distance between the jet direction and the line connecting the points of primary vertex and secondary vertex.
- JetFitter algorithm:
 - JetFitter algorithm [54, 55] the topology of weak b - and c -hadron decays in the jet and finds a common flight line of B and D hadrons. Kalman filter performs for the fitting the primary vertex, secondary vertex and tertiary vertex.

5.3.4 Object Selection

Jet candidates passing following selections are defined as jet object.

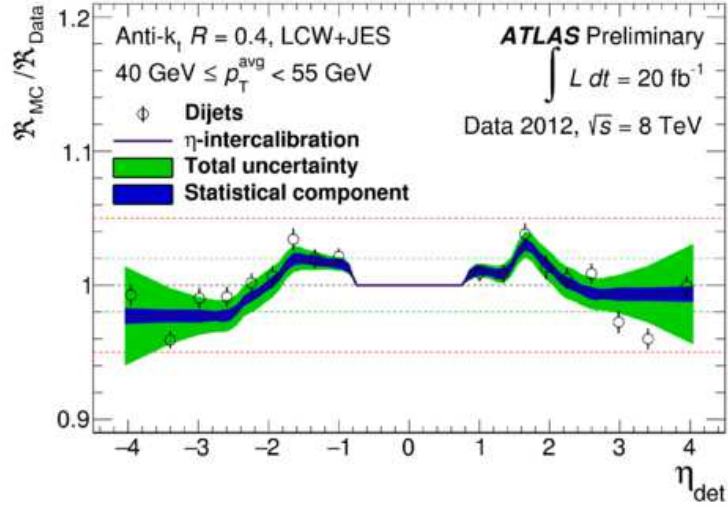


Figure 5.14: The relative jet response as a function of η [46]. The black solid line shows the derived intercalibration factors.

- transverse momentum: $p_T > 30$ GeV
- pseudorapidity: $|\eta| < 4.5$
- jet-vertex fraction (JVF): $|JVF| > 0.5$ for $|\eta| < 2.4$ and $p_T < 50$ GeV.
 JVF is the variable to suppress pileup, defined as the fraction of sum of p_T of the tracks associated to the primary vertex in concern and any vertex in the event. $|JVF| > 0.5$ is required for the jets in $|\eta| < 2.4$ and with $p_T < 50$ GeV.

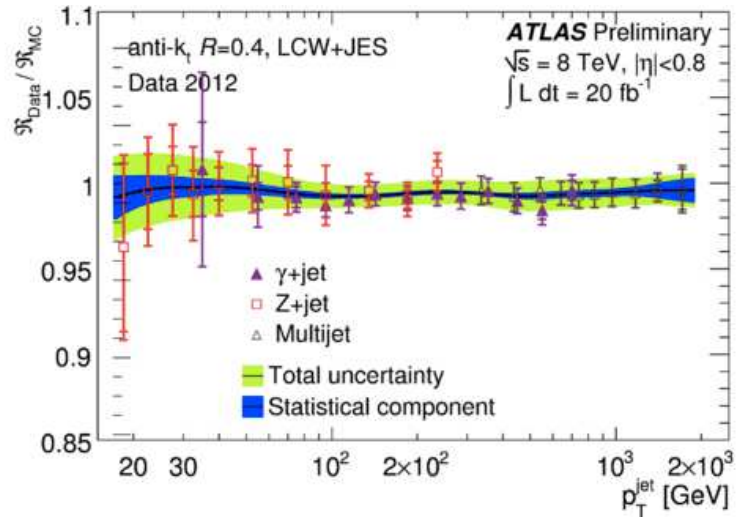


Figure 5.15: The ratio of response for Z^0 +jet, γ +jet and multi-jet balance studies [46].

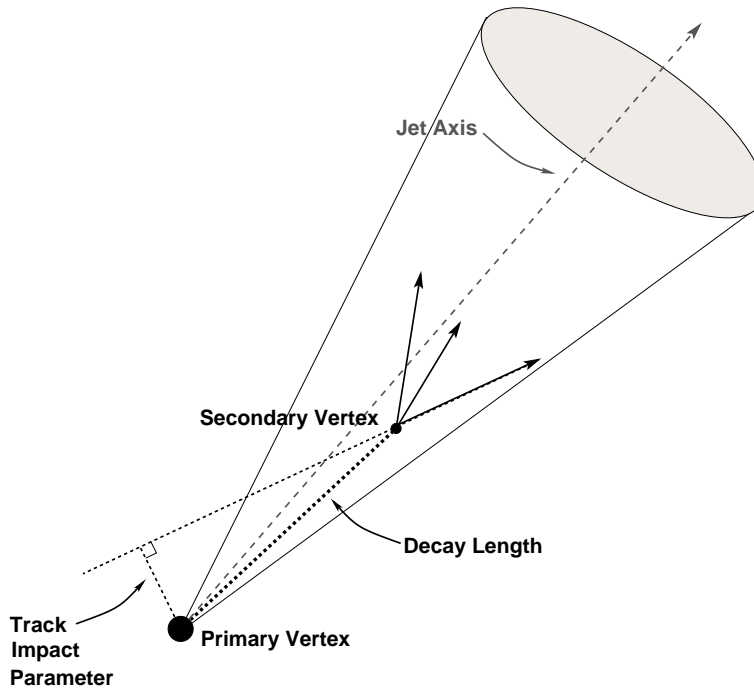


Figure 5.16: Illustration of bottom quark decay [73].

5.4 Tau

5.4.1 Leptonic Decay Tau

For leptonic decay tau shown as Figure 1.12 (a), only a light lepton electron or muon is detected and neutrinos are the component of missing transverse energy. The electron or muon is reconstructed with the way described in Section 5.1 or 5.2.

5.4.2 Hadronic Decay Tau

Reconstruction

The τ lepton can decay hadronically because of its heavy mass shown as Figure 1.12 (b). Such τ 's are referred to as τ_{had} in this thesis. The τ_{had} is reconstructed using the jet candidates which are reconstructed by anti- k_T algorithm with distance parameter $R = 0.4$. The jets with $p_T > 10$ GeV and $|\eta| < 2.5$ are seeded into τ_{had} reconstruction. The primary vertex (defined as the highest $\Sigma(p_T^{\text{track}})^2$) associated to the seed jet is not always corresponding to the one originated from tau decay. The vertex from tau is given by tau vertex associated algorithm [42]. The algorithm provides the vertex which has the highest vertex fraction. The calorimeter cell and cluster directions are calculated in a coordinate system using this vertex provided from the algorithm. The reconstructed tracks, which have $p_T > 1$ GeV and pass the quality cut of the number of tracking detector hits, are matched with the τ_{had} seed in the core region which is $\Delta R(\text{seed}, \text{track}) < 0.2$ from a center of the τ_{had} . The reconstructed τ_{had} is splitted to 1-prong, 3-prong or multi-prong based on the number of tracks in the core region.

Identification

The τ_{had} identification is performed, since many QCD jets are contaminated in the reconstructed τ_{had} . The boosted decision tree (BDT) algorithm is used for the tau identification. The variables performed as a input of the BDT to reject the jets are listed in Table 5.1. The details description is summarized in Appendix A.

The BDT training is performed with separating with 1- and 3-tracks, using simulated tau leptons in Z^0 , W^\pm and Z' samples for the tau, and large collision data samples are used for multi-jet data samples. The some of the variables are shown on Figure 5.17 [42]. The three working points

Table 5.1: The variables performed as a input of the BDT to reject the jets.

Variable	1prong	3prong
f_{cent}	•	•
f_{track}	•	•
R_{track}	•	•
$S_{\text{leadtrack}}$	•	-
$N_{\text{track}}^{\text{iso}}$	•	-
ΔR_{Max}	-	•
S_T^{flight}	-	•
m_{track}	-	•
$m_{\pi^0 + \text{track}}$	•	•
N_{π^0}	•	•
$p_T^{\pi^0} + \text{track}/p_T$	•	•

of loose, medium and tight are available corresponding to the tau identification efficiencies. The

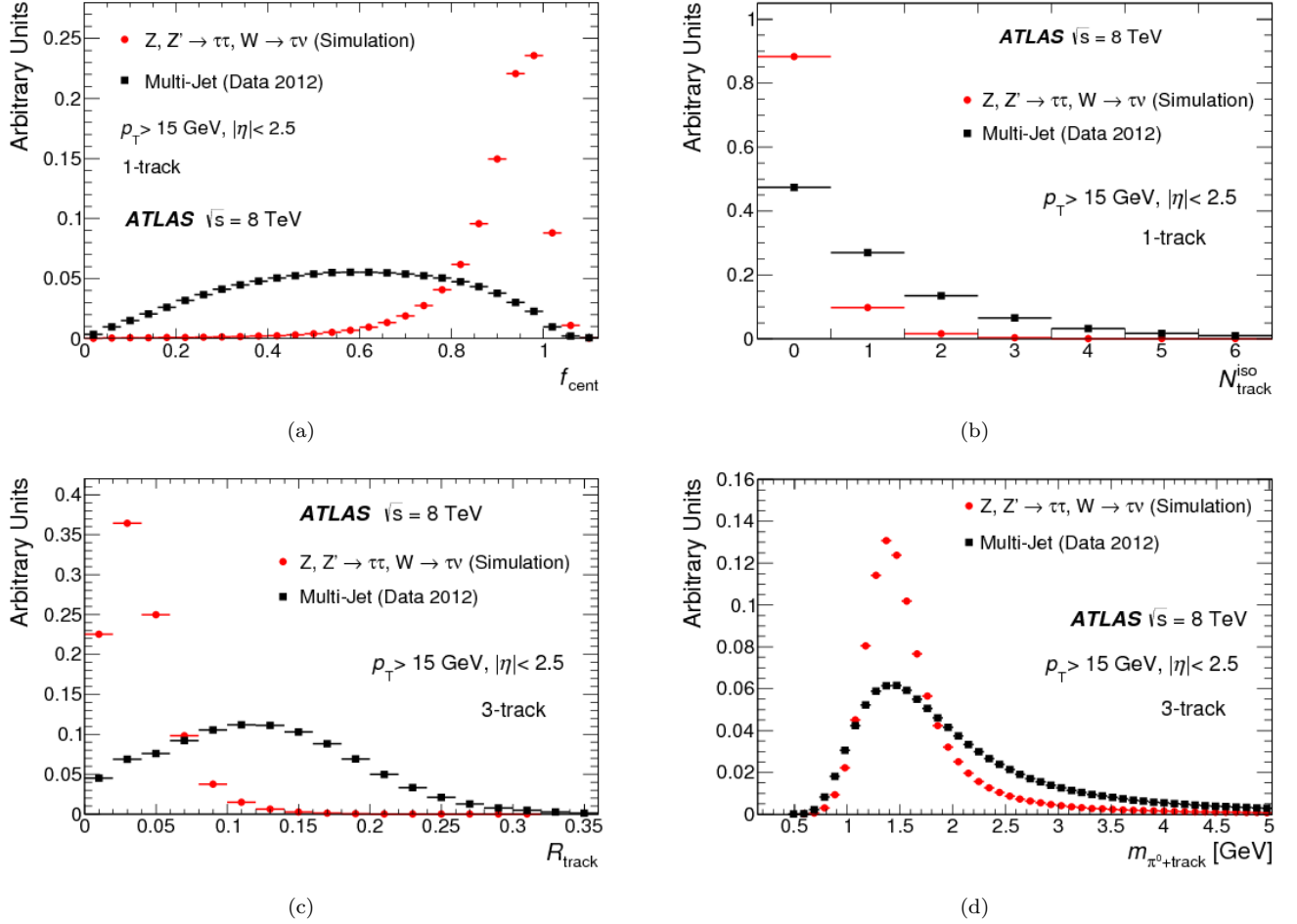


Figure 5.17: Signal and background distribution of (a) f_{cent} for 1-prong, (b) N_{track}^{iso} for 1-prong, (c) R_{track} for 3-prong and (d) $m_{\pi^0+track}$ for 3-prong. These variables are input into the tau identification BDT algorithm. [42]

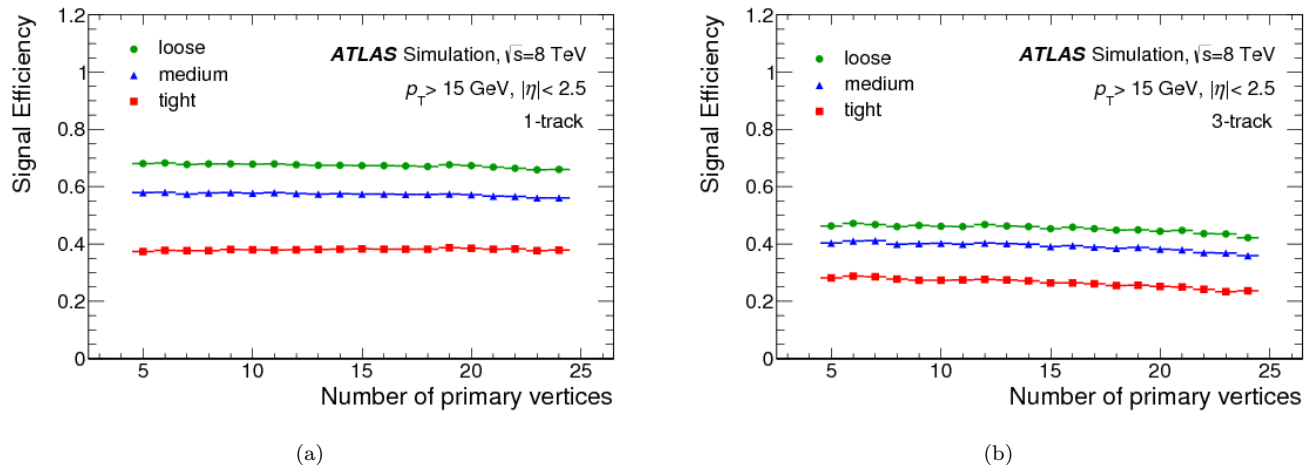


Figure 5.18: The tau identification efficiencies for (a)1-prong and (b)3-prong. [42]

loose, medium and tight working points are corresponding to the signal efficiencies of about 70, 60 and 40% for 1-prong and 45, 40 and 30% for 3-prong, respectively. The Figure 5.18 shows the tau identification efficiencies for 1- and 3-prong τ_{had} .

Energy Scale

The τ_{had} energy calibration is performed with two steps [42].

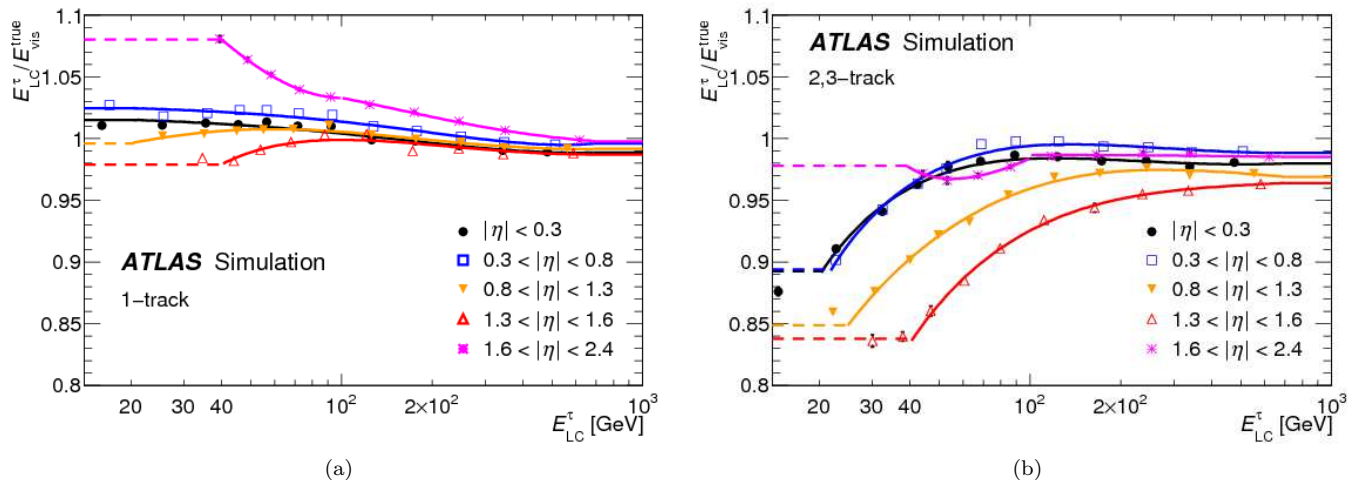
The τ_{had} is in first calibrated with LCW similarly with jets described in 5.3. In order to optimize the cone size for τ_{had} ($\Delta R = 0.2$) and to consider the specific mix of hadrons for τ decay, additional correction is needed. This correction is given as a function of E_{LC}^τ using $Z^0 \rightarrow \tau^+\tau^-$, $W \rightarrow \tau\nu$ and $Z' \rightarrow \tau^+\tau^-$ events simulated with PYTHIA8. The reconstructible τ_{had} candidate is $E_T > 15$ GeV and $|\eta| < 2.4$, since true τ_{had} is available from $E_{T,\text{vis}}^{\text{true}} > 10$ GeV. Moreover to pass medium tau identification and to have a distance of $\Delta R > 0.5$ with other jets are required. The response curve is defined as a ratio of the τ_{had} energy with the LCW scale E_{LC}^τ and true visible energy $E_{\text{vis}}^{\text{true}}$ and given as a function of E_{LC}^τ . The calibration is operated with two processes, (1) the calculating response curve and (2) additional small corrections in order to consider the η bias and pile-p effects.

The response curve is given with respect to the intervals of $E_{\text{vis}}^{\text{true}}$ and of the η for τ_{had} candidates with one or multiple tracks. The function is given average E_{LC}^τ by fitting with a Gaussian function. The Figure 5.19 shows the response curves for 1- or multiple-prong.

Object Selection

The hadronic τ candidates passing following selections are defined as hadronic τ object.

- transverse momentum $p_T > 20$ GeV
- pseudorapidity $|\eta| < 2.5$
- number of charged tracks: 1 or 3 charged tracks associated to the τ_{had} candidate are required.
- charge: charge of the τ_{had} candidate, which is determined from associated tracks, is ± 1 is required.


 Figure 5.19: The tau energy response curves as a given E_{LC}^τ for (a)1-prong and (b)3-prong. [42]

- medium τ_{had} identification is required

5.5 Missing Transverse Momentum

The neutrinos are not detected with any detectors. In the transverse plane, the momentum of all particles should be balanced, therefore the sum of momentum of neutrinos in the transverse plane is expected to be missing transverse energy E_T^{miss} which the flipped vector of the sum of the momentum of all of observable objects. The E_T^{miss} is calculated with

$$E_x^{\text{miss}} = -(E_x^{\text{cal}} + E_x^\mu), \quad (5.8)$$

$$E_y^{\text{miss}} = -(E_y^{\text{cal}} + E_y^\mu), \quad (5.9)$$

$$E_T^{\text{miss}} = \sqrt{(E_x^{\text{miss}})^2 + (E_y^{\text{miss}})^2}, \quad (5.10)$$

where E_x^{miss} and E_y^{miss} are x - and y -component of missing transverse energy. E_x^{cal} and E_y^{cal} are the energies of objects which is reconstructed in the calorimeter, electrons, photons, τ_{had} , jets and the soft term in the x and y axis, respectively. The soft term includes the energy deposited of non-reconstructed particles and non-associated tracks with any objects or clusters. And E_x^μ and E_y^μ represent energy of reconstructed muon. Here all calibrations are applied for the each objects. And for the soft term, the scale so called Soft Term Vertex Fraction (STVF) is applied to take into account the impact from the soft term coming from other vertices. STVF is defined as:

$$\text{STVF} = \frac{\Sigma p_T^{\text{soft-track}}(\text{PV})}{\Sigma p_T^{\text{soft-track}}(\text{PV}) + \Sigma_{\text{all-vertex}} p_T^{\text{soft-track}}} \quad (5.11)$$

5.6 Object Assignment

The defined physics, electron, muon, τ_{had} and jet objects can be overlap among multiple objects. In the case, only one of them is chosen. The selection priority follows the reconstruction and identification efficiencies: muon, electron, hadronic- τ and jet. The cone size used in testing overlap is $\Delta R = 0.2$. For example, if reconstructed a muon object and an electron object are within $\Delta R < 0.2$, then only muon is selected as a physics object and an overlapped electron is removed.

Loose identification is used for the muon and electron in the overlap removal. Furthermore, since low p_T muon is likely to be mis-identified as τ_{had} , lower threshold $p_T^{\text{muon}} > 4$ GeV is used for the muon in testing overlap with τ_{had} . In order to suppress the fake τ_{had} of mis-identified muons,

5.7 Higgs Boson

5.7.1 $h \rightarrow b\bar{b}$ Reconstruction

The b -quark pair is reconstructed by their four vectors. The one or two b -tagged categories are used. For one b -tagged category, highest p_T jet is chosen from no- b -tagged jets. The categorization is described in Section 6.2. The mass distributions are shown in Figure 5.20. What the one b -tagged jet events create the tail in low and high mass regions can be found.

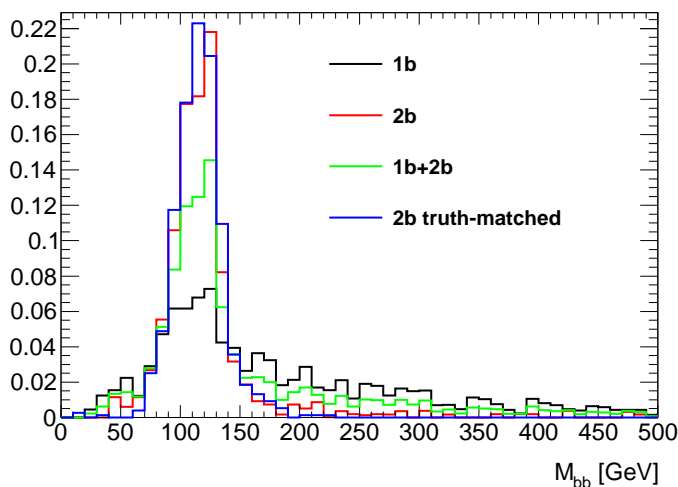


Figure 5.20: bb mass distribution for $m_H = 300$ GeV resonant sample. The black and red lines correspond to one and two b -tagged category, respectively. The merged one is shown with green line. The blue line stands for the bb mass reconstructed from correct two b -jets by using truth information.

5.7.2 $h \rightarrow \tau^+\tau^-$ Reconstruction

The reconstruction of di-tau system is not straightforward because of existence of multiple neutrinos. In this analysis the missing mass calculator (MMC) technique is used for evaluating their contribution [56]. MMC reconstructs the full di-tau system kinematics. If we assume neutrinos come from di-tau decays and detector resolution is perfect, following constraint equations can be written (equation 5.12).

$$\begin{aligned}
 E_x^{\text{miss}} &= p_{\text{mis}_1} \sin \theta_{\text{mis}_1} \cos \phi_{\text{mis}_1} + p_{\text{mis}_2} \sin \theta_{\text{mis}_2} \cos \phi_{\text{mis}_2} \\
 E_y^{\text{miss}} &= p_{\text{mis}_1} \sin \theta_{\text{mis}_1} \sin \phi_{\text{mis}_1} + p_{\text{mis}_2} \sin \theta_{\text{mis}_2} \sin \phi_{\text{mis}_2} \\
 m_{\tau_1}^2 &= m_{\text{mis}_1}^2 + m_{\text{vis}_1}^2 + 2\sqrt{p_{\text{vis}_1}^2 + m_{\text{vis}_1}^2} \sqrt{p_{\text{mis}_1}^2 + m_{\text{mis}_1}^2} \\
 &\quad - 2p_{\text{vis}_1} p_{\text{mis}_1} \cos \Delta\theta_{\text{vm}_1} \\
 m_{\tau_2}^2 &= m_{\text{vis}_2}^2 + 2\sqrt{p_{\text{vis}_2}^2 + m_{\text{vis}_2}^2} \sqrt{p_{\text{mis}_2}^2 + m_{\text{mis}_2}^2} \\
 &\quad - 2p_{\text{vis}_2} p_{\text{mis}_2} \cos \Delta\theta_{\text{vm}_2}
 \end{aligned} \tag{5.12}$$

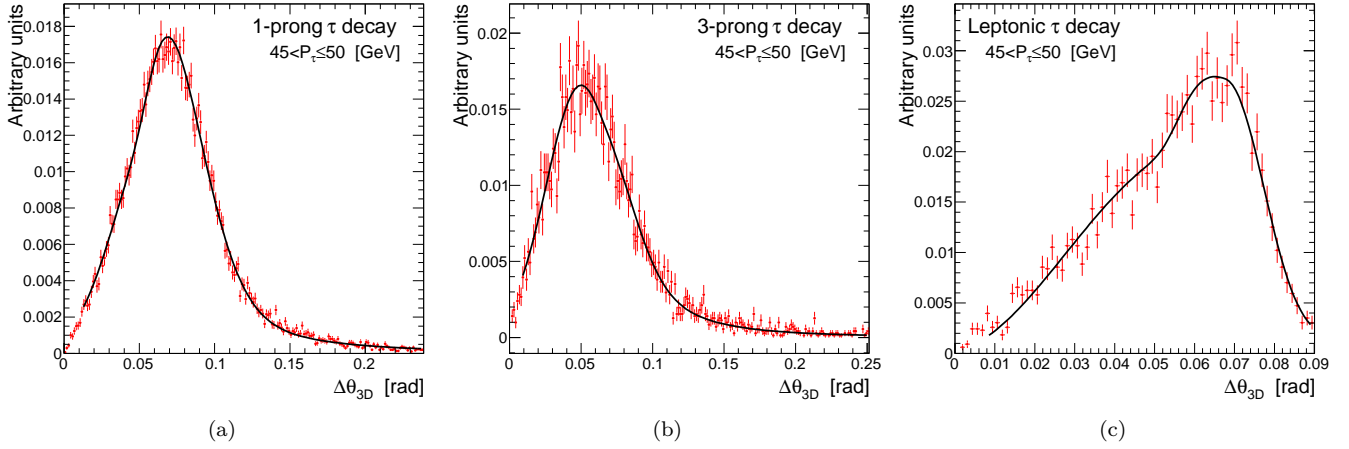


Figure 5.21: Example of the probability distributions as a function of $\Delta\theta_{3D}$ and τ momenta for (a) 1-prong hadronic decay (b) 3-prong hadronic decay (c) leptonic decay.

where $m_{\tau_{1,2}}$ is the invariant mass of tau lepton ($= 1.777 \text{ GeV}/c^2$), E_x^{miss} and E_y^{miss} are components of the transverse missing energy in x and y axes, $p_{\text{vis}1,2}$, $m_{\text{vis}1,2}$, $\phi_{\text{vis}1,2}$ are the momenta, invariant masses, and angles of the visible tau decay products. And $p_{\text{miss}1,2}$, $m_{\text{miss}1,2}$ and $\Delta\theta_{\text{vm}1,2}$ are the momentum, invariant mass of sum of invisible objects of each taus and the angle between the visible and invisible vectors, which are unknown parameters. For the hadronic decay tau, the invariant mass of invisible objects can be set to zero ($m_{\text{miss}2} = 0$), then the number of unknown parameters is reduced. In the case of lep-had channel the number of unknown parameters is seven. To solve the equations, three parameters have to be given, because there are only 4 constraint equations for seven unknown parameters. Here, $\phi_{\text{miss}1,2}$ and $m_{\text{miss}1}$ are chosen. To determine the event fully, a maximum likelihood method with templates of $\Delta\theta_{3D}$ is used. $\Delta\theta_{3D}$ is the angle between the directions of visible and invisible objects from the τ decay. This templates are given in 5 GeV steps of initial τ momenta, in the range of $10 \text{ GeV} < p_T < 230 \text{ GeV}$, for each decay types of leptonic and hadronic, moreover each number of tracks of one or three for hadronic decay. The templates for $45 \text{ GeV} < p_T < 50 \text{ GeV}$ are shown on Figure 5.21. These templates were created from $Z^0/\gamma^* \rightarrow \tau^+\tau^-$ simulation and solid lines on the templates show the fitting functions of linear combination of Gaussian and Landau function. The mean, width and relative normalization of the Gaussian and Landau functions are dependent on the p_τ , and it is parametrised to $a_0(e^{-a_1 \cdot p_\tau} + a_2/p_\tau)$. Where a_i are the coefficients of the parametrisation. This parameterisation leads fully parametrised distributions $\mathcal{P}(\Delta\theta, p_\tau)$. And this arrows to calculate the probability of a particular τ decay topology. $\phi_{\text{miss}1,2}$ and $m_{\text{miss}1}$ are scanned and following event probability is calculated for given $\phi_{\text{miss}1,2}$ and $m_{\text{miss}1}$.

$$\mathcal{P}_{\text{event}} = \mathcal{P}(\Delta\theta_1, p_{\tau 1}) \times \mathcal{P}(\Delta\theta_2, p_{\tau 2}), \quad (5.13)$$

The resolution of the missing energy have strong correlation with MMC, and have to be considered [56]. Then following probability function is used to take in account it.

$$\mathcal{P}_{\text{event}} = \mathcal{P}(\Delta\theta_1, p_{\tau 1}) \times \mathcal{P}(\Delta\theta_2, p_{\tau 2}) \times \mathcal{P}(\Delta E_x^{\text{miss}}) \times \mathcal{P}(\Delta E_y^{\text{miss}}), \quad (5.14)$$

where the probability functions $\mathcal{P}(\Delta E_x^{\text{miss}})$ and $\mathcal{P}(\Delta E_y^{\text{miss}})$ are defined as:

$$\mathcal{P}(E_{x,y}^{\text{miss}}) = \exp\left(-\frac{(\Delta E_{x,y}^{\text{miss}})^2}{2\sigma^2}\right) \quad (5.15)$$

where σ is the resolution of missing transverse energy, and it is provided from missing transverse energy group at ATLAS collaboration [57] and $\Delta E_{x,y}^{\text{miss}}$ are the differences of x - or y - components of missing transverse energy between measured values and the values in the parameter space while scanning over E_x^{miss} and E_y^{miss} . The invariant mass distribution of $\tau^+\tau^-$ reconstructed by MMC is shown in Figure 5.22 for $Z^0 \rightarrow \tau^+\tau^-$, $h \rightarrow \tau^+\tau^-$ and $H \rightarrow b\bar{b}\tau^+\tau^-$ at 300 GeV resonant.

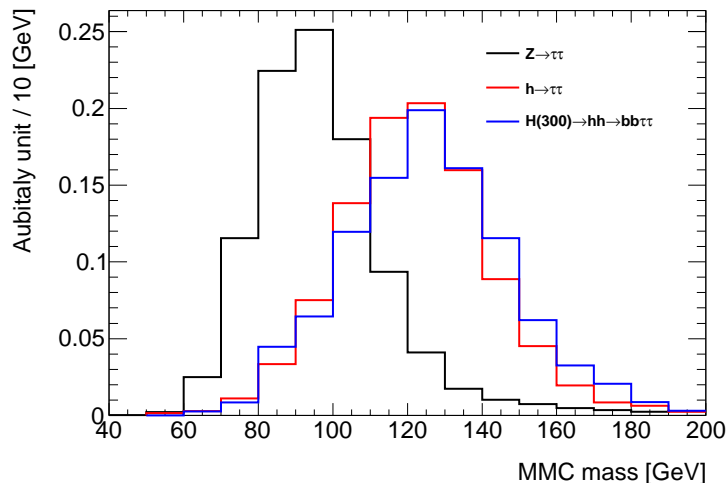


Figure 5.22: $\tau^+\tau^-$ mass distribution reconstructed by MMC for $Z^0 \rightarrow \tau^+\tau^-$, $h \rightarrow \tau^+\tau^-$ and $H \rightarrow b\bar{b}\tau^+\tau^-$ at 300 GeV resonant.

5.8 $b\bar{b}\tau^+\tau^-$ Reconstruction

The invariant masses of the two b -jets and two τ is used as a final discriminant variable. The constrained mass method is introduced in this mass reconstruction to achieve better mass resolution. This method is performed by rescaling p_T and E of the 4-vector of two b -jets and two τ to be $m_h = m_{b\bar{b}}$ and $m_h = m_{\tau^+\tau^-}$. The m_h is the mass of the SM higgs, and $m_h = 125$ GeV is used. This is corresponding to scale only p_T and E and keep the direction ϕ and η of the 4-vectors. The 4-vector of two τ given by MMC described in Section 5.7.2 is used for the calculation. The Figure 5.23 shows the $m_{b\bar{b}\tau^+\tau^-}$ for 300, 500 and 800 GeV reconstructed in different ways. The solid line and dashed line show the with and without constrained mass method, and better mass resolution is achieved with this method.

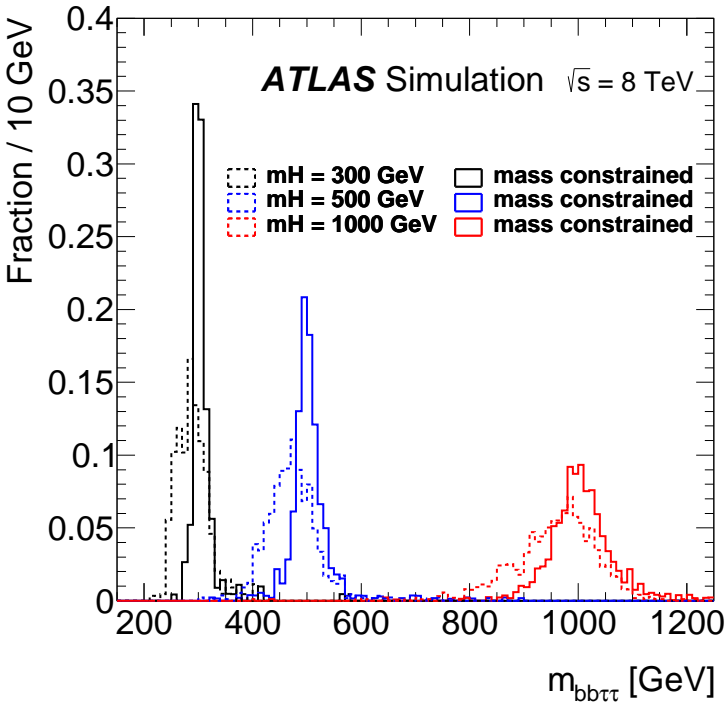


Figure 5.23: The $m_{b\bar{b}\tau^+\tau^-}$ distributions reconstructed by three ways.

Chapter 6

Event Reconstruction and Selection

This section describes event reconstruction.

6.1 Event Pre-Selection

Additional requirements are applied for the events that pass the trigger conditions described in Section 4 in order to increase the data purity and quality. At least one vertex has to be reconstructed using at least four tracks to ensure that the event comes from hard-scattering. Other quality criteria are applied for the suppression of spurious electron candidates lead from the LAr calorimeter problems and of sources of fake missing transverse energy that does not come from proton-proton collisions. Following additional selections are applied, such that the signal event include the physics objects of one isolated charged electron or muon, one τ_{had} and two hadronic b -jets.

- electron or muon: exactly one electron or muon with $p_T > 26$ GeV is required.
- hadronic τ : exactly one τ_{had} is required.
- lepton charge: electron/muon and τ_{had} are oppositely charged
- hadronic jets: at least two jets are required.

Some important kinematic distributions after the event pre-selection are shown in Figure 6.1-6.4 and Figure 6.5-6.8 for electron+ τ_{had} and muon+ τ_{had} channels. The efficiency evaluated at for the each pre-selections step is summarized in Table 6.1. Tables 6.2 shows the number of events passing the pre-selection per 20.3 fb^{-1} at $\sqrt{s} = 8$ TeV for the electron+ τ_{had} and muon+ τ_{had} channels. The data yields is well agree on the background model for both channels.

Table 6.1: Efficiencies of pre-selections evaluated for different $H \rightarrow hh$ masses for 260 to 1000 GeV.

	Non-resonant	260 GeV	300 GeV	350 GeV	400 GeV	500 GeV	800 GeV	1000 GeV
generated	100%	100%	100%	100%	100%	100%	100%	100%
trigger	35.0%	22.4%	26.3%	29.6%	32.9%	38.5%	46.6%	50.0%
one lepton	26.8%	14.0%	18.0%	21.6%	24.9%	30.1%	37.2%	39.8%
di-lepton veto	24.4%	12.6%	16.2%	19.5%	22.8%	27.3%	33.8%	36.1%
one tau	8.3%	4.2%	5.1%	6.5%	8.0%	10.4%	14.0%	16.8%
opposite sign	8.2%	4.1%	5.0%	6.4%	7.9%	10.3%	13.8%	16.6%
at least 2jets	7.2%	3.0%	3.9%	5.2%	6.7%	9.1%	13.1%	15.9%

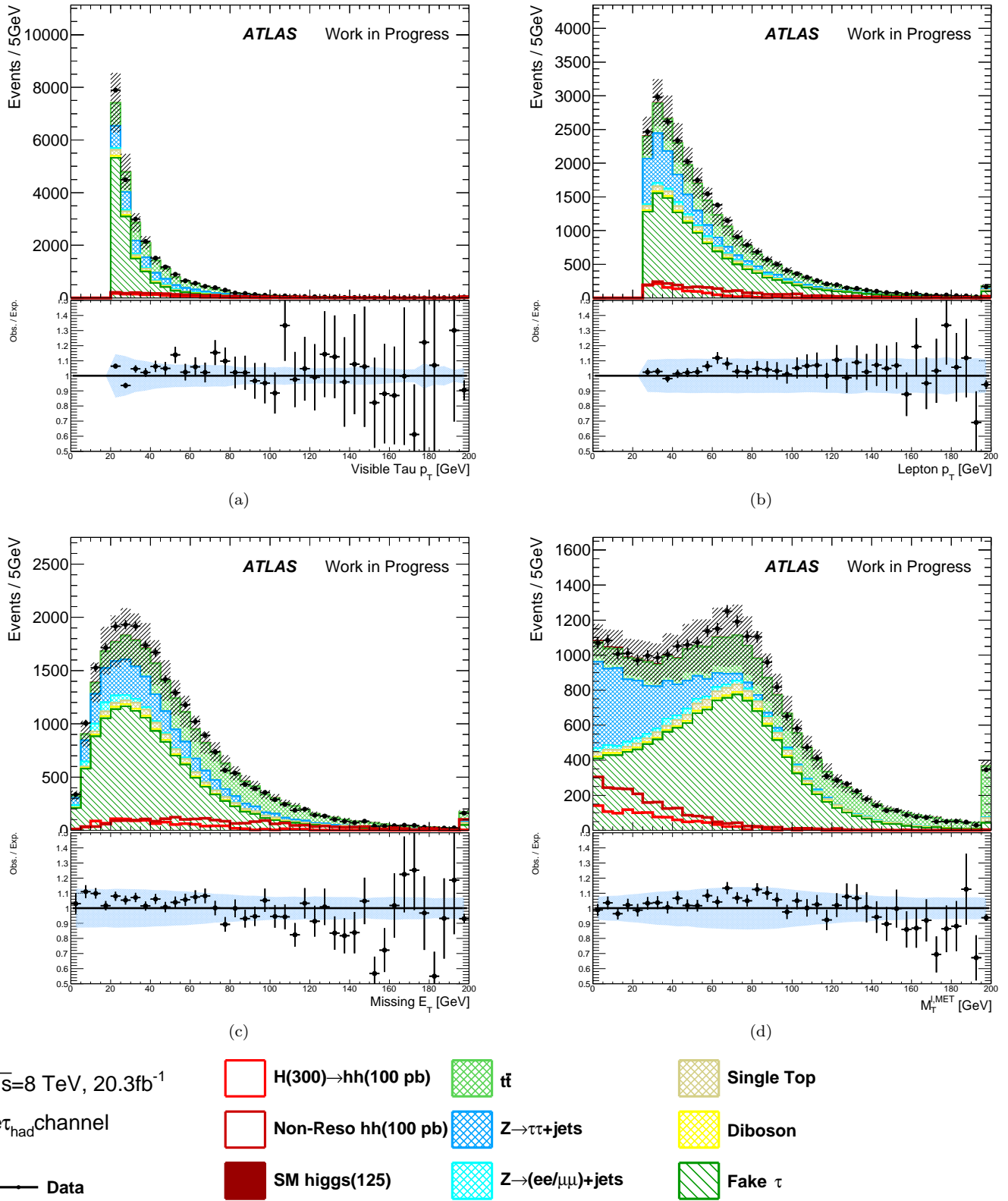


Figure 6.1: Distributions of (a) transverse momentum of τ_{had} , (b) transverse momentum of electron, (c) Missing Energy, and (d) transverse mass of electron and E_T^{miss} in the electron+ τ_{had} channel in the pre-selection level. The data yields well agree on the background model. The shade area shows the statistical and systematical errors combined of the background modeling.

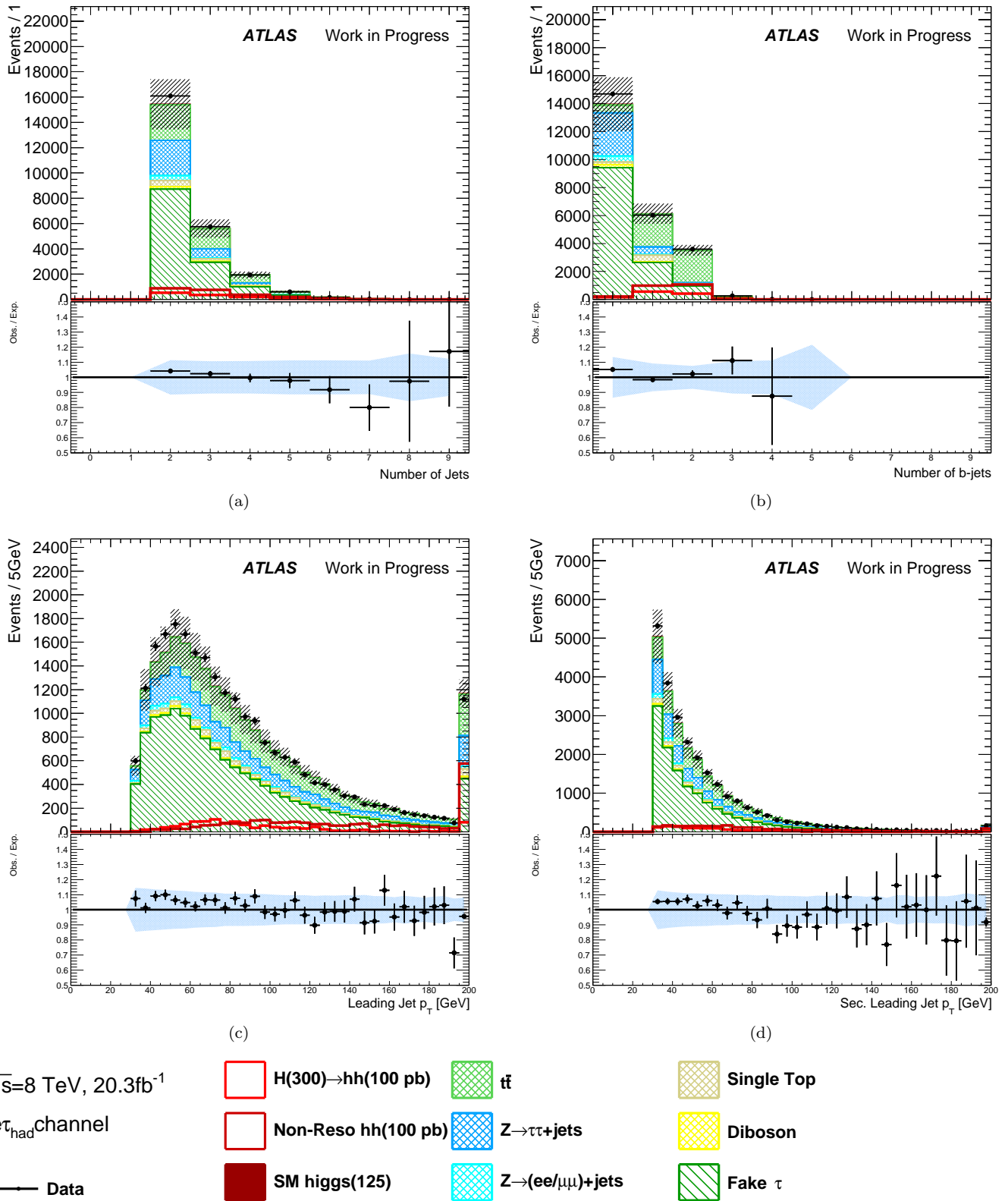


Figure 6.2: Distributions of (a) number of jets, (b) number of b -jets, (c) transverse momentum of leading jet, and (d) transverse momentum of sun-leading jet in the electron+ τ_{had} channel in the pre-selection level. The data yields well agree on the background model. The shade area shows the statistical and systematical errors combined of the background modeling.

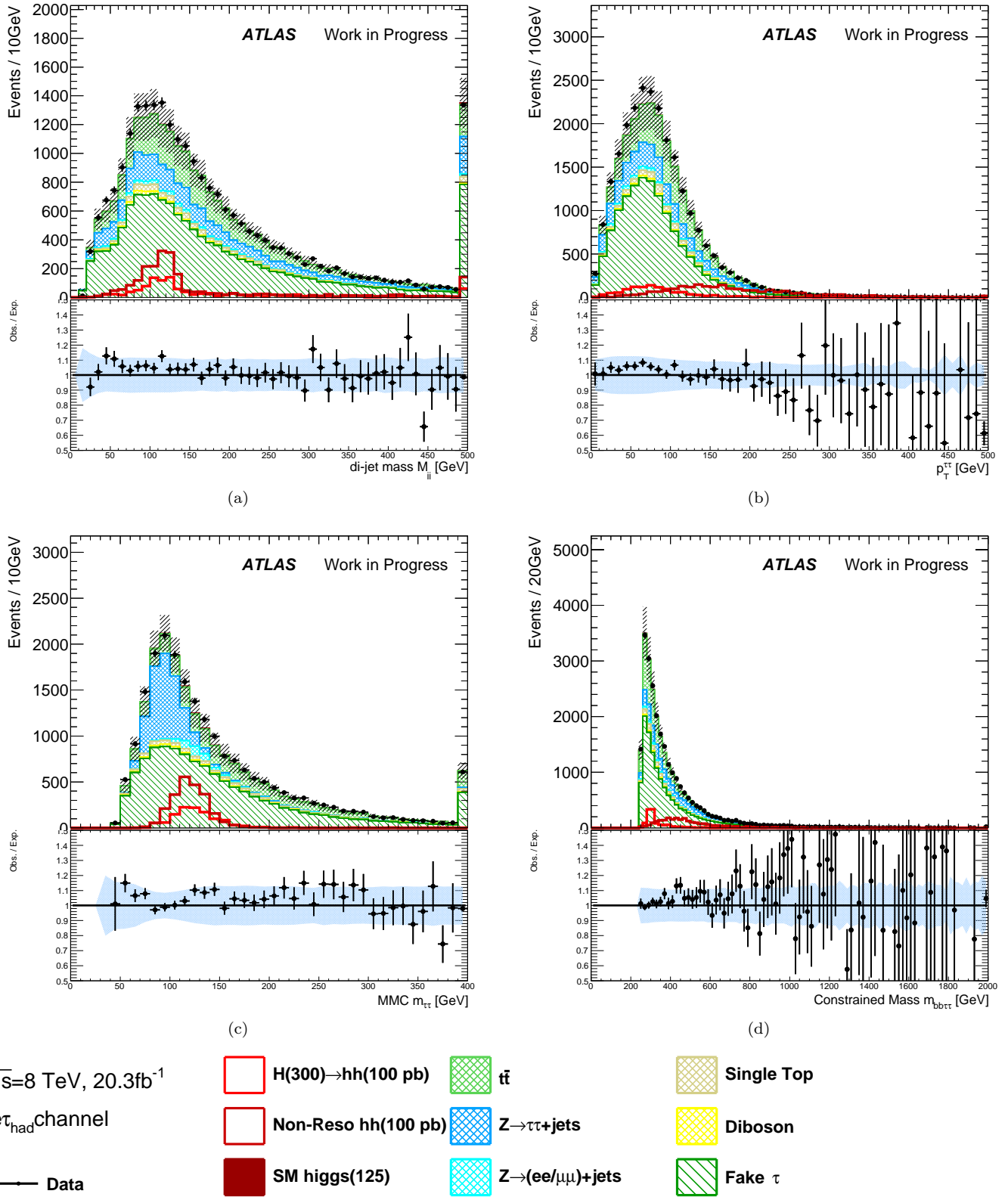


Figure 6.3: Distributions of (a) invariant mass of two b -jets $m_{b\bar{b}}$, (b) transverse momentum of di-tau system, (c) invariant mass of electron and τ_{had} . $m_{\tau+\tau^-}$ reconstructed by MMC, and (d) invariant mass of two b -jets and electron and τ_{had} . $m_{b\bar{b}\tau+\tau^-}$ in the electron+ τ_{had} channel in the pre-selection level. The data yields well agree on the background modeling. The shade area shows the statistical and systematical errors combined of the background modeling.

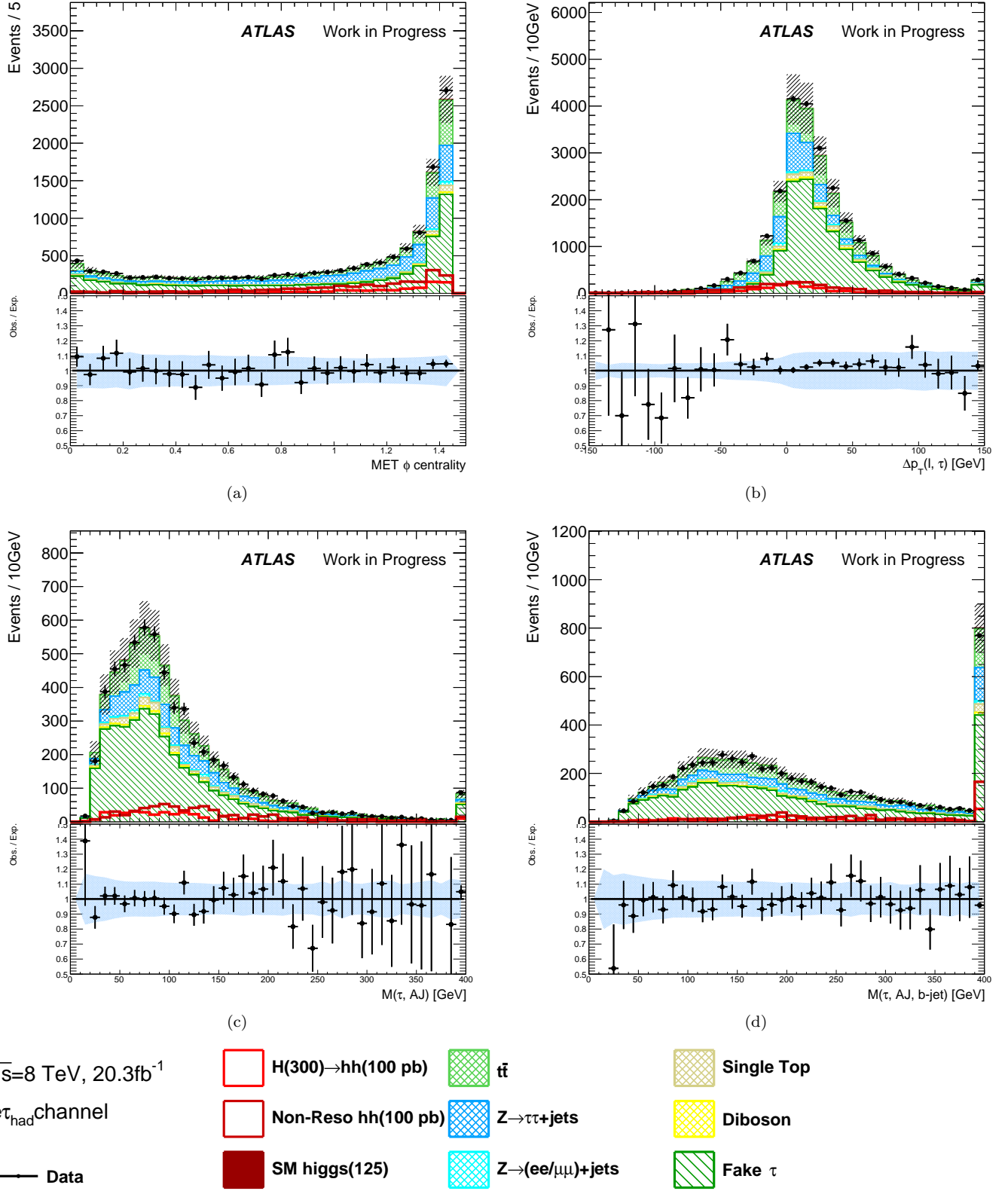


Figure 6.4: Distributions of (a) E_T^ϕ centrality, (b) Δp_T of electron and τ_{had} (c) invariant mass of τ_{had} and additional jet, and (d) invariant mass of τ_{had} , additional jet and b -jet in the electron+ τ_{had} channel in the pre-selection level. The data yields well agree on the background model. The shade area shows the statistical and systematical errors combined of the background modeling.

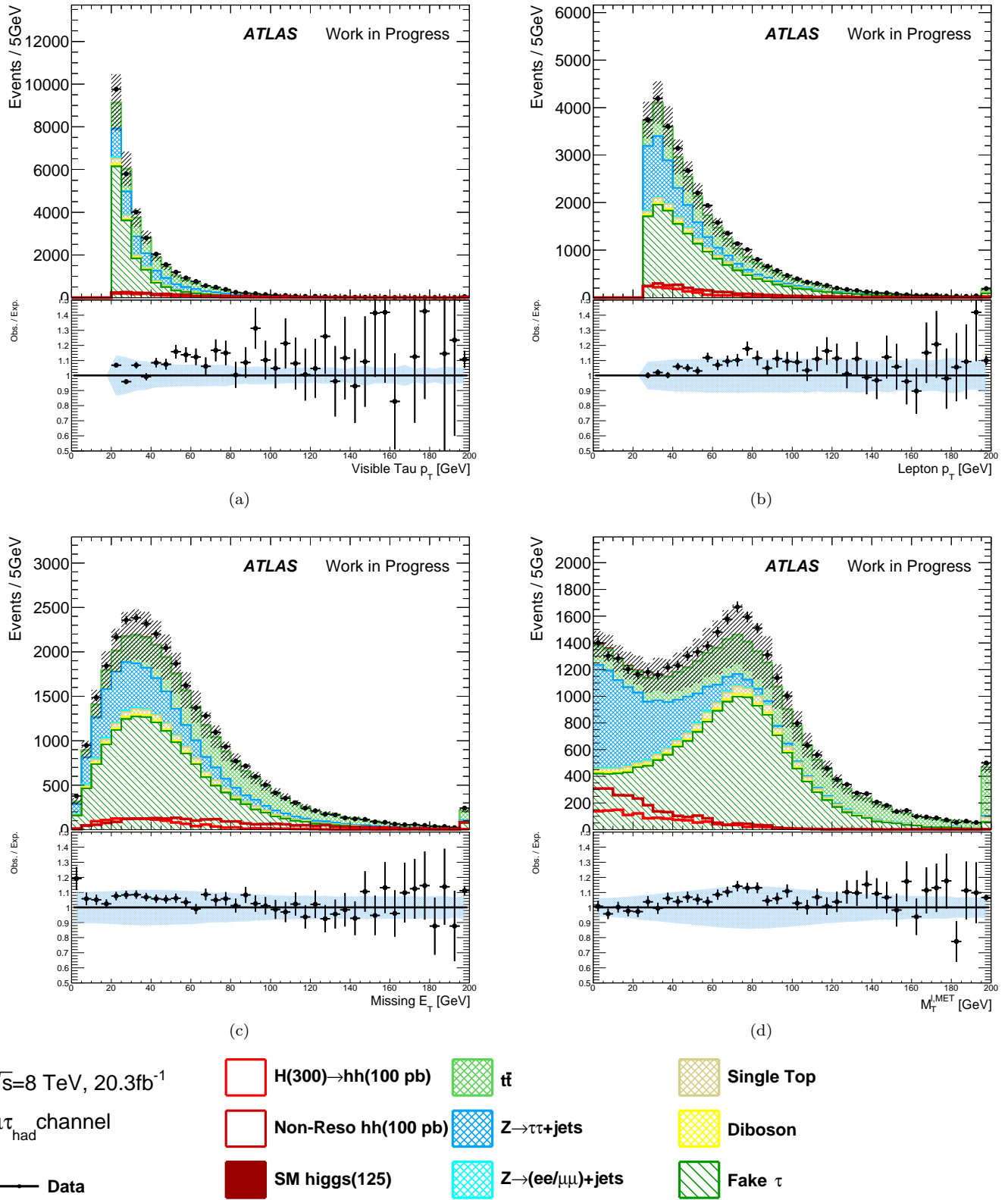


Figure 6.5: Distributions of (a) transverse momentum of τ_{had} , (b) transverse momentum of muon, (c) Missing Energy, and (d) transverse mass of muon and E_T^{miss} in the $\mu\tau_{\text{had}}$ channel in the pre-selection level. The data yields well agree on the background model. The shade area shows the statistical and systematical errors combined of the background modeling.

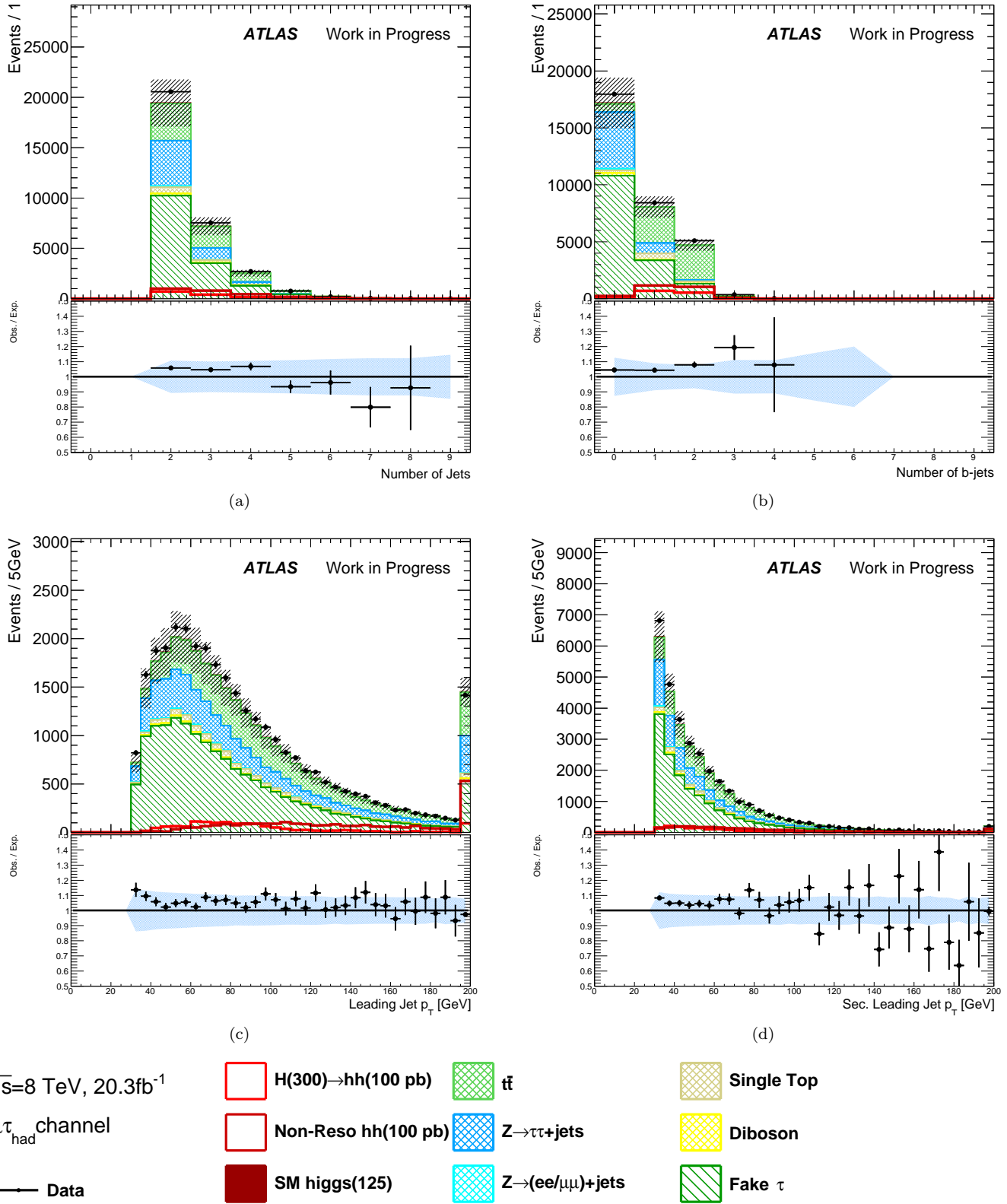


Figure 6.6: Distributions of (a) number of jets, (b) number of b -jets, (c) transverse momentum of leading jet, and (d) transverse momentum of sun-leading jet in the muon+ τ_{had} channel in the pre-selection level. The data yields well agree on the background model. The shade area shows the statistical and systematical errors combined of the background modeling.

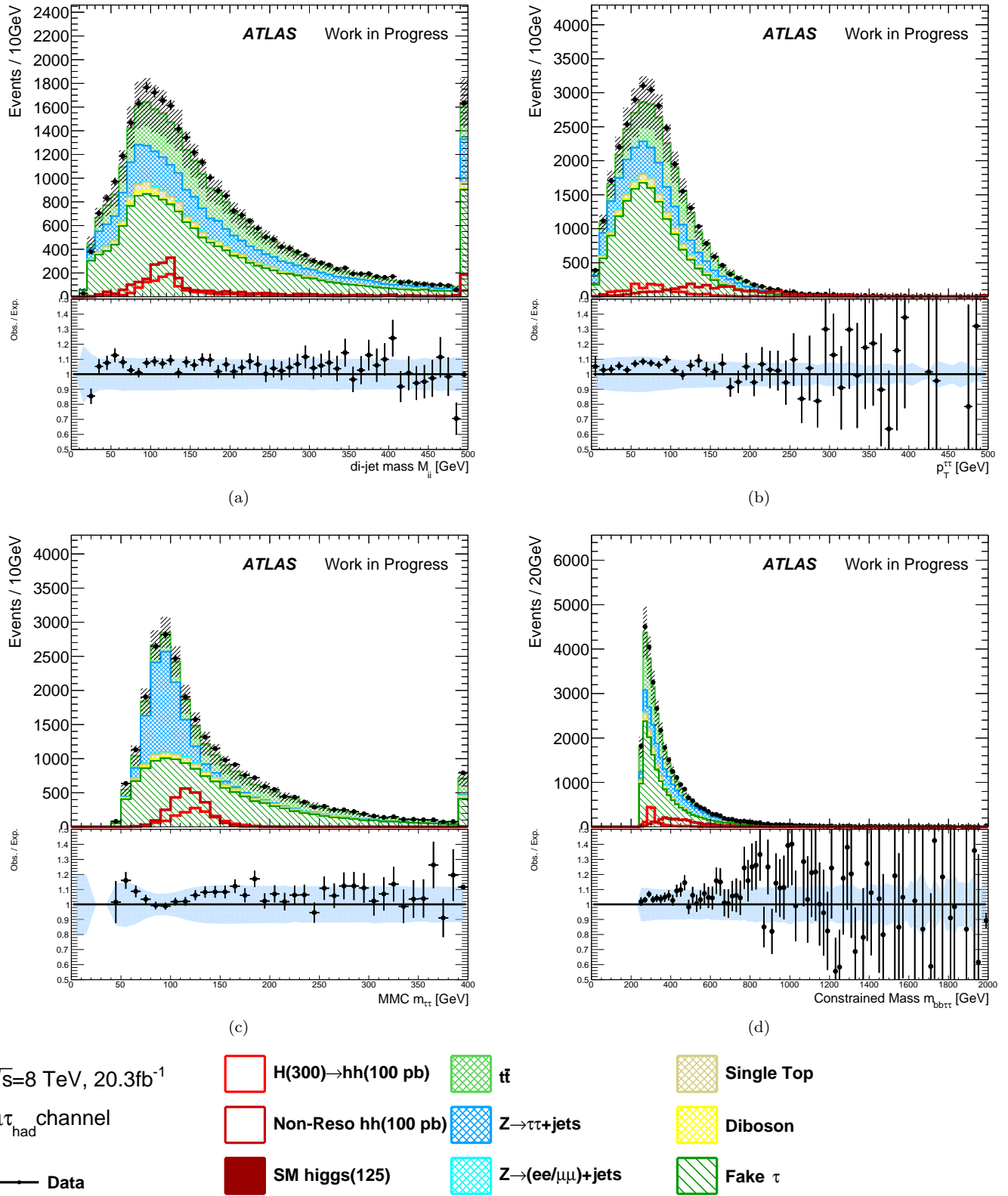


Figure 6.7: Distributions of (a) invariant mass of two b -jets $m_{b\bar{b}}$, (b) transverse momentum of di-tau system, (c) invariant mass of muon and τ_{had} . $m_{\tau+\tau-}$ reconstructed by MMC, and (d) invariant mass of two b -jets and muon and τ_{had} . $m_{b\bar{b}\tau+\tau-}$ in the muon+ τ_{had} channel in the pre-selection level. The data yields well agree on the background model. The shade area shows the statistical and systematical errors combined of the background modeling.

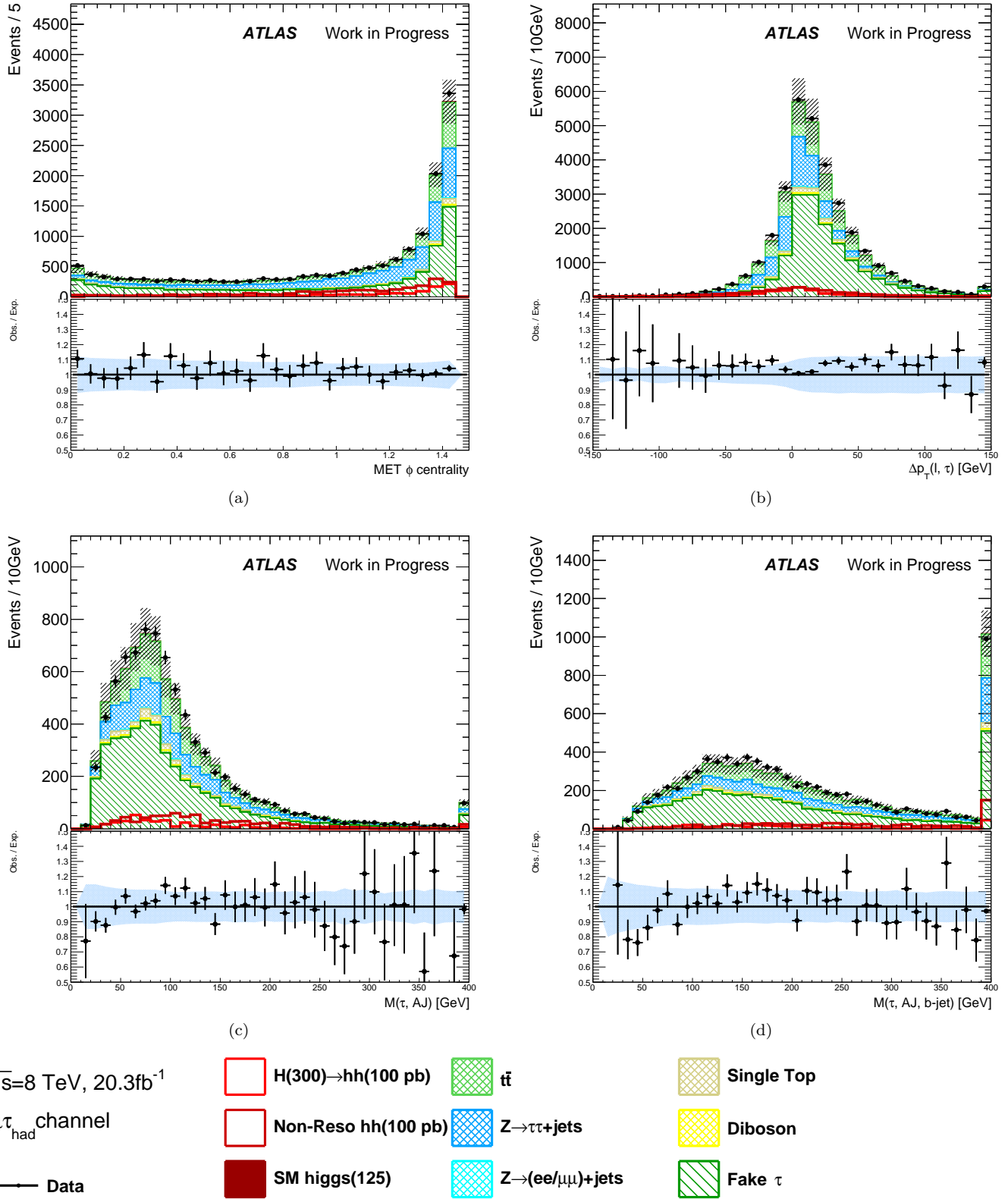


Figure 6.8: Distributions of (a) E_T^ϕ centrality, (b) Δp_T of muon and τ_{had} (c) invariant mass of τ_{had} and additional jet, and (d) invariant mass of τ_{had} , additional jet and b -jet in the muon+ τ_{had} channel in the pre-selection level. The data yields well agree on the background model. The shade area shows the statistical and systematical errors combined of the background modeling.

Table 6.2: Signal and background yields per 20.3 fb^{-1} at $\sqrt{s} = 8 \text{ TeV}$.

Process	Events	
	$\mu\tau_h$	$e\tau_h$
Signal non-resonant	25.0 ± 1.0	23.0 ± 1.0
Signal resonant 300	13.7 ± 0.9	11.3 ± 0.8
Single Higgs(125.4)	73.2 ± 1.1	62.4 ± 1.0
(VBFH $\rightarrow \tau^+\tau^-$)	20.4 ± 0.2	17.5 ± 0.2
(ggFH $\rightarrow \tau^+\tau^-$)	42.3 ± 1.0	35.7 ± 1.0
(W/ZH $\rightarrow \tau^+\tau^-$)	8.9 ± 0.2	7.6 ± 0.2
(ttH $\rightarrow \tau^+\tau^-$)	1.6 ± 0.4	1.5 ± 0.1
(W/ZH $\rightarrow \text{bb}$)	1.5 ± 0.4	1.6 ± 0.4
ttbar	6979.4 ± 701.9	5364.3 ± 541.2
$Z^0 \rightarrow \tau^+\tau^-$	6338.1 ± 71.8	3989.5 ± 68.2
Single Top	1007.0 ± 50.3	843.7 ± 48.6
Diboson	942.5 ± 31.4	780.8 ± 30.2
$Z^0 \rightarrow \ell\ell$	136.2 ± 16.6	421.8 ± 22.2
Fake τ	15778.4 ± 3156.0	13220.5 ± 2644.4
Total Background	31255.8 ± 3234.5	24683.7 ± 2700.8
Data	32009	24729

6.2 Analysis Categorization

The events are categorized into following four categories.

- number of b -tagged jets

The signal process should have two b -tagged jets in the final state, but one b -tagged jet events are also used in our analysis to allow one un-tagged events to enhance the signal efficiency. Here 80% efficiency working point for b -tagging is used. In the one b -tagged category, for reconstruction of two b -tagged jets kinematics, a jet with highest p_T is selected as un-tagged jet from all of the non b -tagged jets in the event.

- p_T of di-tau system

The fraction of signal and background is different depending on di-tau system transverse momentum. The di-tau system transverse momentum distribution, which is calculated by MMC, is shown in Figure 6.9 for both one and two b -tagged jets categories. The categorization based on the transverse momentum of the di-tau system is used to increase the sensitivity, and the events are split into two categories based on $p_T^{\tau^+\tau^-}$ of lower or higher than 100 GeV.

Table 6.3: Analysis categories.

category	Number of b -tagged jets	$p_T^{\tau^+\tau^-}$
TwoB HighPt	≥ 2	$>100 \text{ GeV}$
TwoB LowPt	≥ 2	$<100 \text{ GeV}$
OneB HighPt	1	$>100 \text{ GeV}$
OneB LowPt	1	$<100 \text{ GeV}$

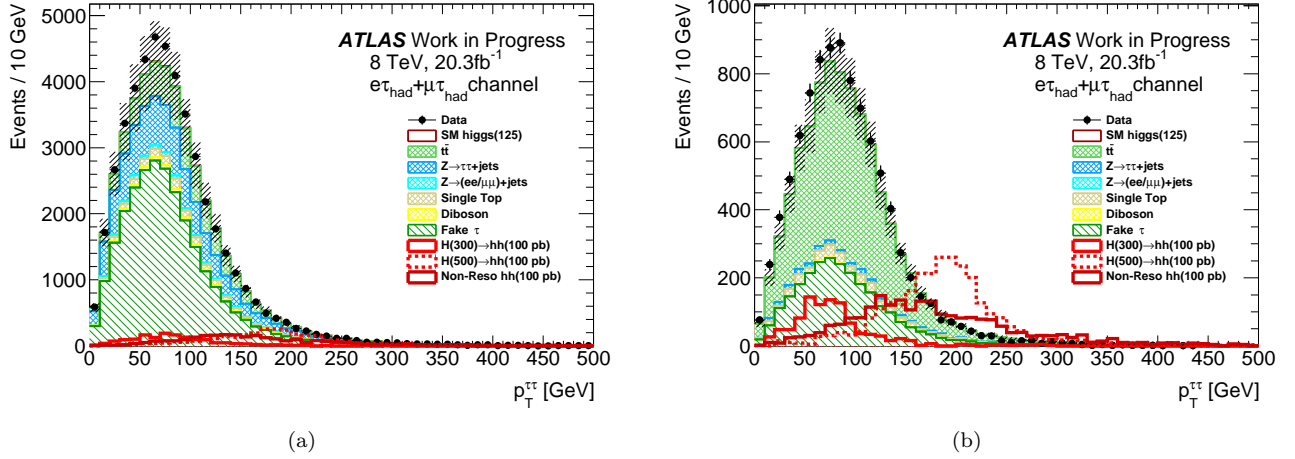


Figure 6.9: Number of events as function of p_T of di-tau system (a) 1 b -tagged and (b) 2 b -tagged categories.

6.3 Event Selection for Background Suppression

The following event selections are applied to suppress the background events and raise the signal to background ratio.

- transverse mass of lepton and missing transverse energy:
The motivation of this cut is to suppress the backgrounds including W^\pm boson decaying leptonically. The transverse mass of lepton and missing transverse energy distributes to form W^\pm boson edge. Full reconstruction of the W^\pm boson decaying leptonically is hard because of lack of information neutrino z -direction. In stead, transverse mass defined as:

$$m_T^{l, E_T^{\text{miss}}} = \sqrt{2p_T^{\text{lep}} E_T^{\text{miss}} (1 - \cos \Delta\phi)} \quad (6.1)$$

retains information of W^\pm mass, where p_T^{lep} stands for the transverse momentum of the lepton and $\Delta\phi$ is the angle between the directions of lepton on p_T and E_T^{miss} . $m_T^{l, E_T^{\text{miss}}} \leq 60$ GeV is required to suppress W^\pm background.

- ϕ centrality of missing transverse energy:
This variable, E_T^{miss} ϕ centrality, quantifies the positional relationship of light lepton(e/μ), tau and E_T^{miss} . This variable is defined as:

$$E_T^{\text{miss}} \phi \text{ centrality} = (A + B) / \sqrt{A^2 + B^2} \quad (6.2)$$

$$A = \frac{\sin(\phi_{E_T^{\text{miss}}} - \phi_\tau)}{\sin(\phi_{e/\mu} - \phi_\tau)} \quad (6.3)$$

$$B = \frac{\sin(\phi_{e/\mu} - \phi_{E_T^{\text{miss}}})}{\sin(\phi_{e/\mu} - \phi_\tau)} \quad (6.4)$$

This variable returns the value of $\sqrt{2}$ when the direction of E_T^{miss} equals the bisector of e/μ and τ_{had} directions, 1 when E_T^{miss} direction is completely the same as e/μ or τ_{had} and < 1 if E_T^{miss} is outside the region between e/μ and τ . The motivation of this cut is to suppress top and W +jets backgrounds. For the signal case, E_T^{miss} direction is likely to be inside of the region between e/μ and τ . Figure 6.10 shows this variable for signal($m_H = 300$ GeV) and W +jets background.

- semileptonic decaying $t\bar{t}$ rejection cut:

The event topology of semileptonic decay of $t\bar{t}$ has two b -tagged jets, one electron or muon and two non b -tagged jets in the final state. If one of the jets is mis-identified as a hadronic- τ , it could be background. This cut is motivated to suppress such events. In the events, the hadronic decay side W^\pm boson can be reconstructed from two jets, where one of the jets is mis-identified as a hadronic- τ . Moreover, if b -tagged jets are assigned correctly to the two b -jets, the parent hadronic decay side top quark can be reconstructed as a parent W^\pm boson can be reconstructed from $m(\text{jet}, \tau)$ and the parent top quark can be reconstructed from $m(b\text{-jet}, \text{jet}, \tau)$. The b -tagged jet is selected in a way as to minimize $m(e/\mu, b\text{-jet}) + m(\tau, b\text{-jet})$. Figure 6.11 shows the 2 dimensional plots of reconstructed W^\pm boson mass and top quark mass. And a χ^2 of them in the elliptical transformation:

$$\left(\frac{\Delta m_W \cos \theta - \Delta m_{top} \sin \theta}{28 \text{ GeV}} \right)^2 + \left(\frac{\Delta m_W \sin \theta - \Delta m_{top} \cos \theta}{18 \text{ GeV}} \right)^2 > 1 \quad (6.5)$$

is required. The ellipse is defined as following equation and shown in the figure with black solid line.

$$R = \left(\frac{x}{a} \right)^2 + \left(\frac{y}{b} \right)^2 \quad (6.6)$$

$$\begin{pmatrix} x \\ y \end{pmatrix} = \begin{pmatrix} \cos \theta & -\sin \theta \\ \sin \theta & \cos \theta \end{pmatrix} \begin{pmatrix} \Delta m_W \\ \Delta m_{top} \end{pmatrix} \quad (6.7)$$

- dileptonic decaying $t\bar{t}$ rejection cut:

The p_T of hadronic- τ is likely to be greater than p_T of an electron or muon, in case of signal, because the electron or muon comes from 3-body decay of parent τ , while hadronic- τ comes from 2-body decay. But in case of $t\bar{t}$ decaying into dileptonically, p_T of the electron or muon is likely to be greater than p_T of hadronic- τ , because electron or muon and parent τ directly come from W^\pm boson decay, but hadronic- τ is sharing its p_T with a neutrino emitted from parent τ decay. So a variable $\Delta p_T(\text{lep}, \tau)$ defined as following is introduced.

$$\Delta p_T(\text{lep}, \tau) = p_T^{\text{lep}} - p_T^\tau \quad (6.8)$$

Figure 6.12 shows the distribution of $\Delta p_T(\text{lep}, \tau)$ for both signal and $t\bar{t}$. $\Delta p_T(\text{lep}, \tau) < 20 \text{ GeV}$ is appropriate for this variable to select signal events.

- higgs mass window:

The higgs masses are reconstructed from a b -tagged jet pair and two-tau pair, and following cuts are required for resonant search.

$$\begin{aligned} & - 90 < m_{b\bar{b}} < 160 \text{ GeV} \\ & - 100 < m_{\tau^+\tau^-} < 150 \text{ GeV} \end{aligned}$$

For the non-resonant search, only $m_{b\bar{b}}$ cut is applied, because $m_{\tau^+\tau^-}$ is used as a final discriminant variable.

The signal deficiencies for non-resonant and resonant search for varied mass points are shown in Table 6.4-6.6 for each of analysis categories.

The number of data passing all selections are listed in Table 6.8 for both non-resonant and resonant search .

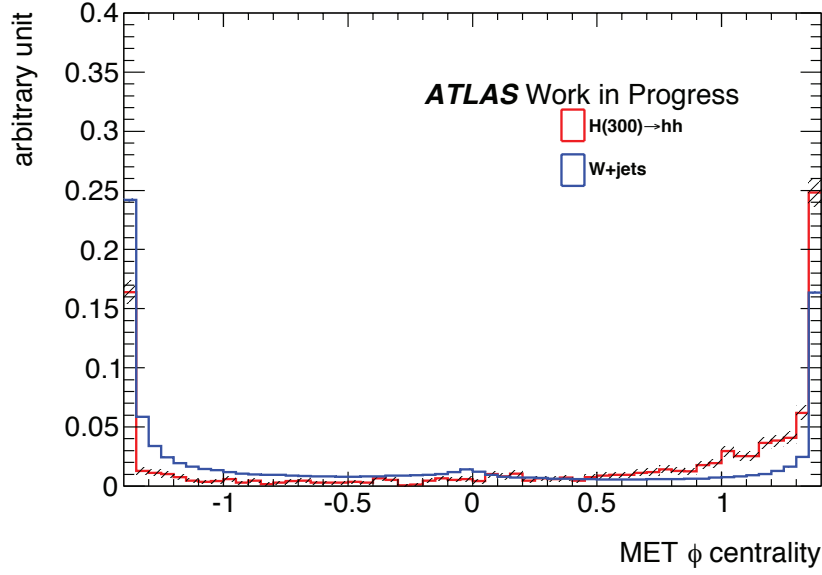

 Figure 6.10: MET ϕ centrality distribution of $m_H = 300$ GeV signal (red) and W^\pm +jets (blue).

 Table 6.4: Signal deficiencies for all selections for OneB and Low $p_T^{\tau^+\tau^-}$ category for non-resonant and various resonant masses from 260 to 1000 GeV.

	Non-resonant	260 GeV	300 GeV	350 GeV	400 GeV	500 GeV	800 GeV	1000 GeV
generated	100%	100%	100%	100%	100%	100%	100%	100%
pre-selection	7.2%	3.0%	3.9%	5.2%	6.7%	9.1%	13%	16%
OneB	3.00%	1.27%	1.31%	2.26%	2.92%	3.75%	4.87%	5.32%
Low $p_T^{\tau^+\tau^-}$	0.26%	1.16%	0.83%	0.95%	0.56%	0.39%	0.097%	0.045%
$m_T(l, \tau) < 60$	0.22%	0.91%	0.68%	0.78%	0.43%	0.3%	0.073%	0.03%
MET ϕ centrality > 1 .	0.13%	0.54%	0.42%	0.5%	0.27%	0.18%	0.053%	0.018%
Ellipse $R > 1$	0.13%	0.51%	0.44%	0.48%	0.26%	0.18%	0.053%	0.018%
$\Delta p_T < 20$ GeV	0.1%	0.47%	0.35%	0.39%	0.19%	0.16%	0.053%	0.01%
$90 < m_{jj} < 160$ GeV	0.044%	0.23%	0.17%	0.18%	0.095%	0.055%	0.017%	0%
$100 < m_{\tau^+\tau^-} < 150$ GeV	-	0.18%	0.12%	0.1%	0.058%	0.038%	0.01%	0%

 Table 6.5: Signal deficiencies for all selections for OneB and High $p_T^{\tau^+\tau^-}$ category for non-resonant and various resonant masses from 260 to 1000 GeV.

	Non-resonant	260 GeV	300 GeV	350 GeV	400 GeV	500 GeV	800 GeV	1000 GeV
generated	100%	100%	100%	100%	100%	100%	100%	100%
pre-selection	7.2%	3.0%	3.9%	5.2%	6.7%	9.1%	13%	16%
OneB	3.00%	1.27%	1.31%	2.26%	2.92%	3.75%	4.87%	5.32%
High $p_T^{\tau^+\tau^-}$	2.74%	0.11%	0.48%	1.3%	2.37%	3.36%	4.77%	5.28%
$m_T(l, \tau) < 60$	2.44%	0.095%	0.43%	1.15%	2.14%	3.03%	4.34%	4.8%
MET ϕ centrality > 1 .	1.56%	0.065%	0.26%	0.67%	1.28%	1.91%	2.56%	3.12%
Ellipse $R > 1$	1.52%	0.062%	0.25%	0.64%	1.24%	1.85%	2.55%	3.11%
$\Delta p_T < 20$ GeV	1.05%	0.035%	0.18%	0.47%	0.87%	1.28%	1.69%	2.02%
$90 < m_{jj} < 160$ GeV	0.34%	0.0025%	0.035%	0.14%	0.34%	0.47%	0.78%	1.01%
$100 < m_{\tau^+\tau^-} < 150$ GeV	-	0.0025%	0.06%	0.12%	0.29%	0.38%	0.68%	0.88%

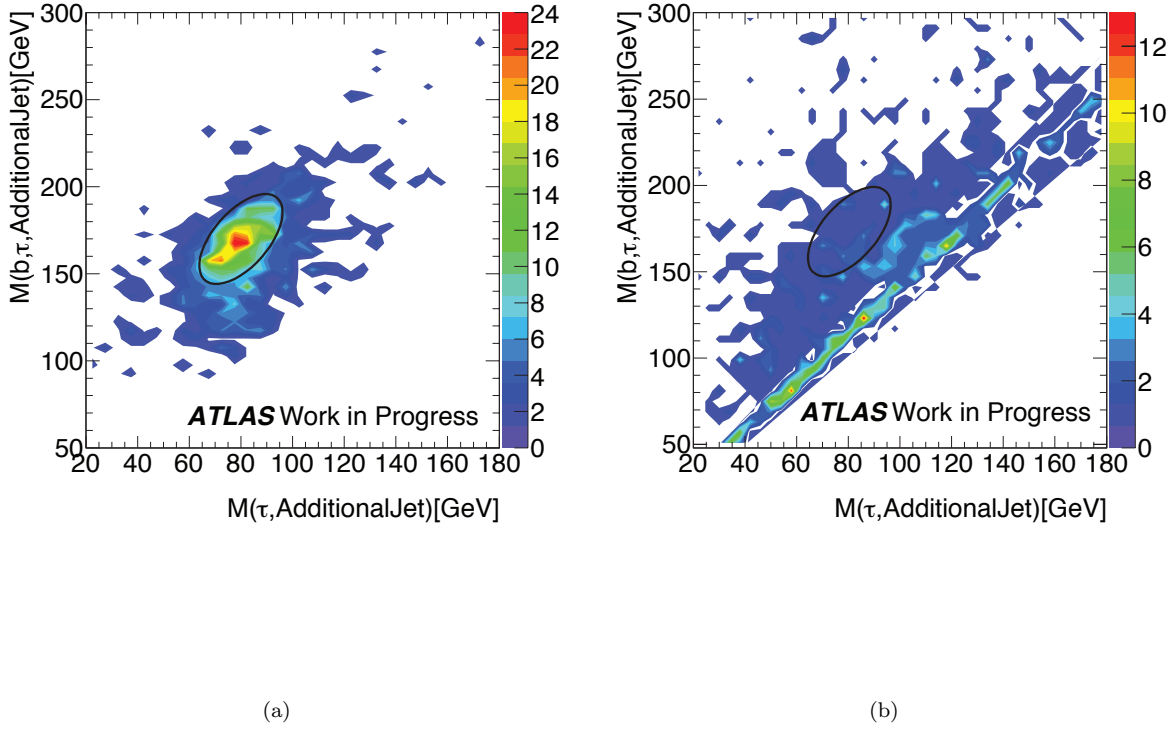


Figure 6.11: $m_{\tau, \text{jet}}$ vs $m_{\tau, \text{jet}, b\text{-jet}}$ in 2D plane for (a) $t\bar{t}$ background and (b) 300 GeV signal.

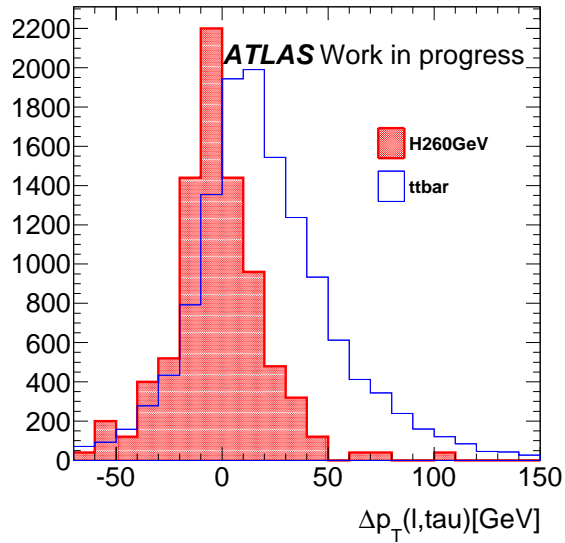


Figure 6.12: $\Delta p_T(l, \tau_{\text{had}})$ distribution in 10 GeV bin for resonant signal of $m_H = 260$ GeV (red) and $t\bar{t}$ background (blue).

Table 6.6: Signal deficiencies for all selections for TwoB and High $p_T^{\tau^+\tau^-}$ category for non-resonant and various resonant masses from 260 to 1000 GeV.

	Non-resonant	260 GeV	300 GeV	350 GeV	400 GeV	500 GeV	800 GeV	1000 GeV
generated	100%	100%	100%	100%	100%	100%	100%	100%
pre-selection	7.2%	3.0%	3.9%	5.2%	6.7%	9.1%	13%	16%
TwoB	2.97%	1.18%	1.49%	2.17%	2.8%	4.18%	7.35%	8.62%
High $p_T^{\tau^+\tau^-}$	2.68%	0.097%	0.53%	1.22%	2.24%	3.95%	7.29%	8.6%
$m_T(l, \tau) < 60$	2.41%	0.083%	0.49%	1.12%	2.05%	3.54%	6.66%	7.84%
MET ϕ centrality > 1.	1.58%	0.058%	0.3%	0.62%	1.31%	2.3%	4.27%	5.16%
Ellipse R > 1	1.54%	0.058%	0.3%	0.61%	1.28%	2.24%	4.26%	5.14%
$\Delta p_T < 20$ GeV	1.00%	0.04%	0.21%	0.46%	0.87%	1.59%	2.79%	3.32%
$90 < m_{jj} < 160$ GeV	0.77%	0.023%	0.15%	0.36%	0.69%	1.24%	2.31%	2.79%
$100 < m_{\tau^+\tau^-} < 150$ GeV	-	0.01%	0.12%	0.31%	0.56%	1.03%	1.99%	2.4%

 Table 6.7: Signal deficiencies for all selections for TwoB and Low $p_T^{\tau^+\tau^-}$ category for non-resonant and various resonant masses from 260 to 1000 GeV.

	Non-resonant	260 GeV	300 GeV	350 GeV	400 GeV	500 GeV	800 GeV	1000 GeV
generated	100%	100%	100%	100%	100%	100%	100%	100%
pre-selection	7.2%	3.0%	3.9%	5.2%	6.7%	9.1%	13%	16%
TwoB	2.97%	1.18%	1.49%	2.17%	2.8%	4.18%	7.35%	8.62%
Low $p_T^{\tau^+\tau^-}$	0.29%	1.09%	0.96%	0.95%	0.56%	0.23%	0.06%	0.02%
$m_T(l, \tau) < 60$	0.23%	0.87%	0.82%	0.78%	0.45%	0.19%	0.053%	0.018%
MET ϕ centrality > 1.	0.15%	0.47%	0.5%	0.5%	0.3%	0.12%	0.037%	0.015%
Ellipse R > 1	0.15%	0.46%	0.48%	0.49%	0.3%	0.12%	0.037%	0.015%
$\Delta p_T < 20$ GeV	0.12%	0.4%	0.39%	0.38%	0.24%	0.095%	0.03%	0.015%
$90 < m_{jj} < 160$ GeV	0.09%	0.34%	0.32%	0.32%	0.18%	0.07%	0.023%	0.01%
$100 < m_{\tau^+\tau^-} < 150$ GeV	-	0.22%	0.23%	0.21%	0.11%	0.045%	0.013%	0.01%

 Table 6.8: The numbers of events passing event selections per 20.3 fb^{-1} at $\sqrt{s} = 8 \text{ TeV}$.

search mode	OneB Low	OneB High	TwoB Low	TwoB High
non-resonant	266	157	118	117
resonant	92	46	35	35

Chapter 7

Background Estimation

In this section, the methods of background estimation are described.

7.1 Overview of The Methods

The final state in this analysis contains two b -tagged jets and one light lepton (electron or muon) and τ_{had} . The major background processes are split into four sources depending whether light lepton and hadronic- τ are true or fake.

- a jet fakes to tau:
The main processes of this source are top background, QCD and W +jets.
- a jet fakes to light lepton:
This process, for example $W \rightarrow \tau\nu$ +jets (fake to electron or muon), is not considered in this analysis, because of tiny contribution and negligible.
- both light lepton and hadronic- τ are true:
The main processes of this source are $t\bar{t}$, and $Z^0/\gamma^* \rightarrow \tau^+\tau^-$ associated with heavy flavor jets, diboson $\rightarrow l + \tau_{\text{had}} + X$ and single-top can contribute.
- a lepton fakes to hadronic- τ :
The main processes of this source are top background and $Z^0 \rightarrow e^+e^-/\mu^+\mu^-$ +heavy flavor jets, and diboson can contribute.

7.2 Fake Factor Method

7.2.1 Fake Factor Method

The fake τ_{had} background is estimated by fake factor (FF) method. This method is used in the standard model higgs boson search in $h \rightarrow \tau^+\tau^-$ analysis [61]. The basic approach of this method is applying the FF, which is the rate that a jet fakes to τ_{had} , to the jet events. This method has been developed using a jet rich control sample. This control sample is created by applying similar event selection as signal τ_{had} . but failing medium τ BDT identification is required. This requirement enhances the purity of jets. In order to minimize the difference in partons components between identified- τ and “anti- τ ” samples, passing the criteria of 0.7 times the working point of loose τ BDT identification is required for anti- τ identification. This working point provides to keep a similar quark/gluon fraction (Figure 7.1) in the two samples. The fake factor FF_{CR} is calculated

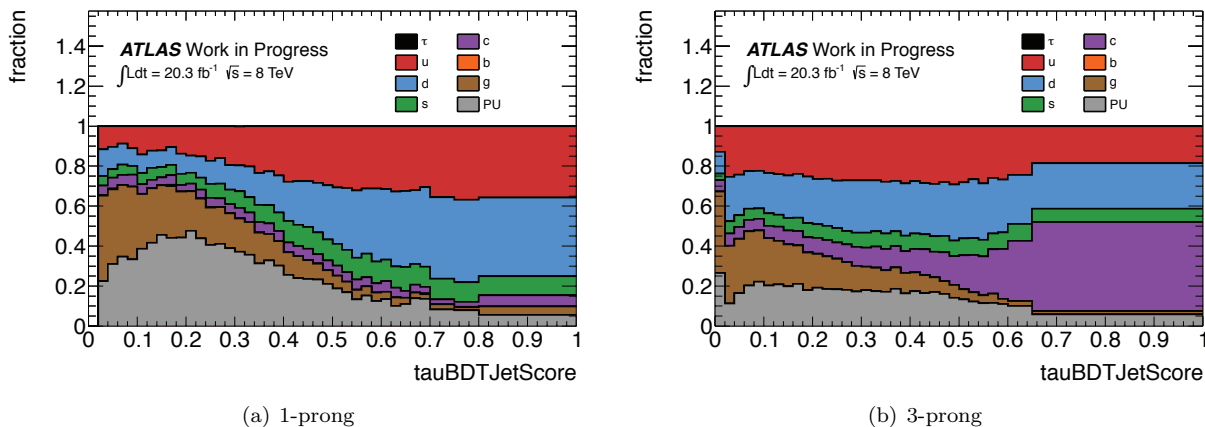


Figure 7.1: Fraction of partons in jet events as function of tau selection criteria.

in the data control regions described later, and defined as

$$\text{FF}_{\text{CR}} \equiv \frac{N_{\text{CR}}^{\text{identified}-\tau}}{N_{\text{CR}}^{\text{anti}-\tau}} \quad (7.1)$$

, where $N_{\text{CR}}^{\text{identified}-\tau}$ is the number of events identified as τ , and $N_{\text{CR}}^{\text{anti}-\tau}$ is the number of events of anti-identification τ in the control region.

The fake background $N_{\text{Bkg.}}^{\text{Est.}}$ is estimated by multiplying this factor to the anti- τ data sample subtracted true tau contribution,

$$N_{\text{Bkg.}}^{\text{Est.}} = (N_{\text{data,SR}}^{\text{anti}-\tau} - N_{\text{true,SR}}^{\text{anti}-\tau}) \times \text{FF}_{\text{CR}} \quad (7.2)$$

where $N_{\text{data,SR}}^{\text{anti}-\tau}$ is the number of events of anti- τ in the signal region, $N_{\text{true,SR}}^{\text{anti}-\tau}$ is the number of events including real τ . $N_{\text{true,SR}}^{\text{anti}-\tau}$ is evaluated as the failed τ_{had} identification in $Z^0 \rightarrow \tau^+\tau^-$ is estimated from MC simulation. $t\bar{t}$ and diboson also contribute to this.

The one anti-tau event can have multiple anti- τ candidates, and considering this, Equation 7.2 can be transformed to

$$N_{\text{Bkg.}}^{\text{Est.}} = \sum_{i \in \text{data}} \sum_{0 < j < \bar{n}_i} \text{FF}_{\text{CR}}^j - \sum_{i \in \text{true}} \sum_{0 < j < \bar{n}_i} \text{FF}_{\text{CR}}^j \quad (7.3)$$

where i stands for event number, and j shows the number for anti- τ candidates. This method allows to estimate the fake τ background from different processes, QCD, W +jets, $Z^0 \rightarrow \ell\ell(j \rightarrow \tau)$ and $\text{Top}(j \rightarrow \tau)$, all at once. In a practical way, one anti- τ candidate is weighted by FF and summed up for one event.

7.2.2 Control Region Definitions

The fake factors are measured in the control regions optimized of each background, W +jets, QCD, Top and $Z^0 \rightarrow \ell\ell(j \rightarrow \tau)$. The definitions of the control regions are:

- W +jets: pre-selections, but with $m_T^{l, E_T^{\text{miss}}} > 70$ GeV requirement
- QCD: pre-selection, but with lepton isolation relaxed (no track or calo isolation)
- $\text{Top}(j \rightarrow \tau)$: pre-selections but with one b -tagged jet and $m_T^{l, E_T^{\text{miss}}} > 70$ GeV requirement

- $Z^0 \rightarrow \ell\ell(j \rightarrow \tau)$: pre-selections but with dilepton veto inverted

The fake factors are shown in Figure 7.2 for the number of tracks of one or three.

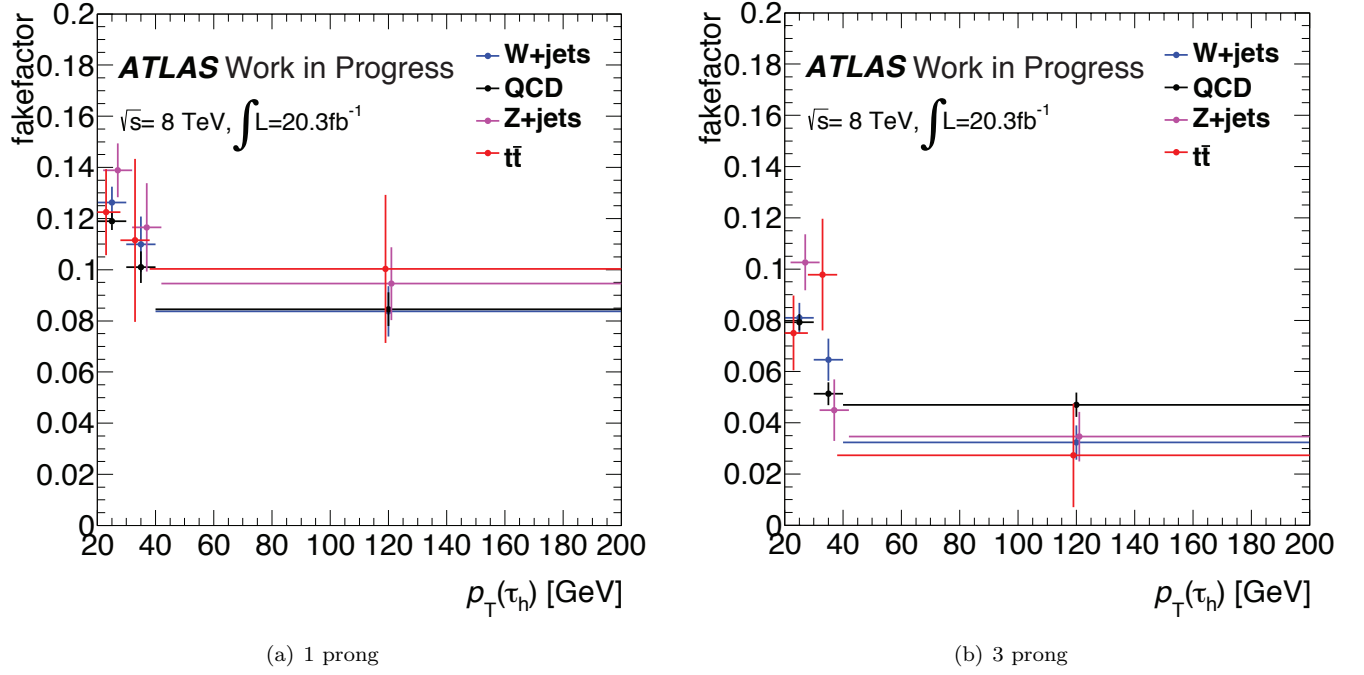


Figure 7.2: Fake factors for various processes for (a) 1 prong and (b) 3 prong.

7.2.3 Combined Fake Factor

The FFs are measured in each control regions, but we can not know the actual physics process for one event. Therefore the pre-measured event fraction R_i of a background i in the anti- τ_{had} signal region is applied for the FF.

$$\text{FF}(p_T, n_{\text{prong}}) = \sum_{i=\text{bkg}} R_i \text{FF}_i(p_T, n_{\text{prong}}) \quad (7.4)$$

where R_i is the fraction of the background i . For W +jets, the fraction $R_{W+\text{jets}}$ is calculated by using data events and part of simulation.

$$R_{W+\text{jets}} = \frac{N_{W+\text{jets}}^{\text{anti-}\tau}}{N_{\text{all-fakes}}^{\text{anti-}\tau}} = \frac{N_{W+\text{jets}}^{\text{anti-}\tau}}{N_{\text{data}}^{\text{anti-}\tau} - N_{\text{others,MC}}^{\text{anti-}\tau}} \quad (7.5)$$

$$N_{W+\text{jets}}^{\text{anti-}\tau} = N_{\text{data,WCR}}^{\text{anti-}\tau} \times \frac{N_{\text{MC,W+jets}}^{\text{anti-}\tau}}{N_{\text{MC,W+jets,WCR}}^{\text{anti-}\tau}} \quad (7.6)$$

where $N_{\text{all-fakes}}^{\text{anti-}\tau}$ represents the total number of fake τ_{had} events and $N_{W+\text{jets}}^{\text{anti-}\tau}$ is the number of events of W +jets in the anti- τ signal region. $N_{\text{data}}^{\text{anti-}\tau}$ is the number of data in the anti- τ signal region and $N_{\text{others,MC}}^{\text{anti-}\tau}$ is the number of events which is real τ_{had} with failing τ identification and estimated by MC simulation. The number of expected W +jets events $N_{W+\text{jets}}^{\text{anti-}\tau}$ are estimated from the number of data events of anti- τ in the W +jets control region multiplying to the factor of the fraction of the anti- τ events between the signal $N_{\text{MC,W+jets}}^{\text{anti-}\tau}$ and W +jets control region $N_{\text{MC,W+jets,WCR}}^{\text{anti-}\tau}$. The

factor is estimated by MC simulation. The R_{Top} and $R_{Z \rightarrow ll}$ are estimated from MC simulation, and R_{QCD} is estimated from

$$R_{\text{QCD}} = 1 - (R_{W+\text{jets}} + R_{\text{Top}} + R_{Z \rightarrow ll}) \quad (7.7)$$

Table 7.1 summarize the fake background composition.

Table 7.1: Fraction of the different processes contributing to the fake background.

R_W	0.46
R_{QCD}	0.40
R_Z	0.11
R_{Top}	0.03

7.2.4 Method Validation

The FF method is validated by checking the same sing of light lepton and τ_{had} events. Kinematic distributions are shown in Figure 7.3, 7.4 in one and two b -tagged categories, respectively. In the plot, the low and high $p_{\text{T}}^{\tau^+\tau^-}$ categories are merged for the event statistics. The estimated yield is 132.4 ± 26.7 and 32.9 ± 7.5 for one b -tag and two b -tag category, and 130 and 33 events are observed for each categories. And the reasonable agreement can be seen for not only event yield but also shape of the each distributions.

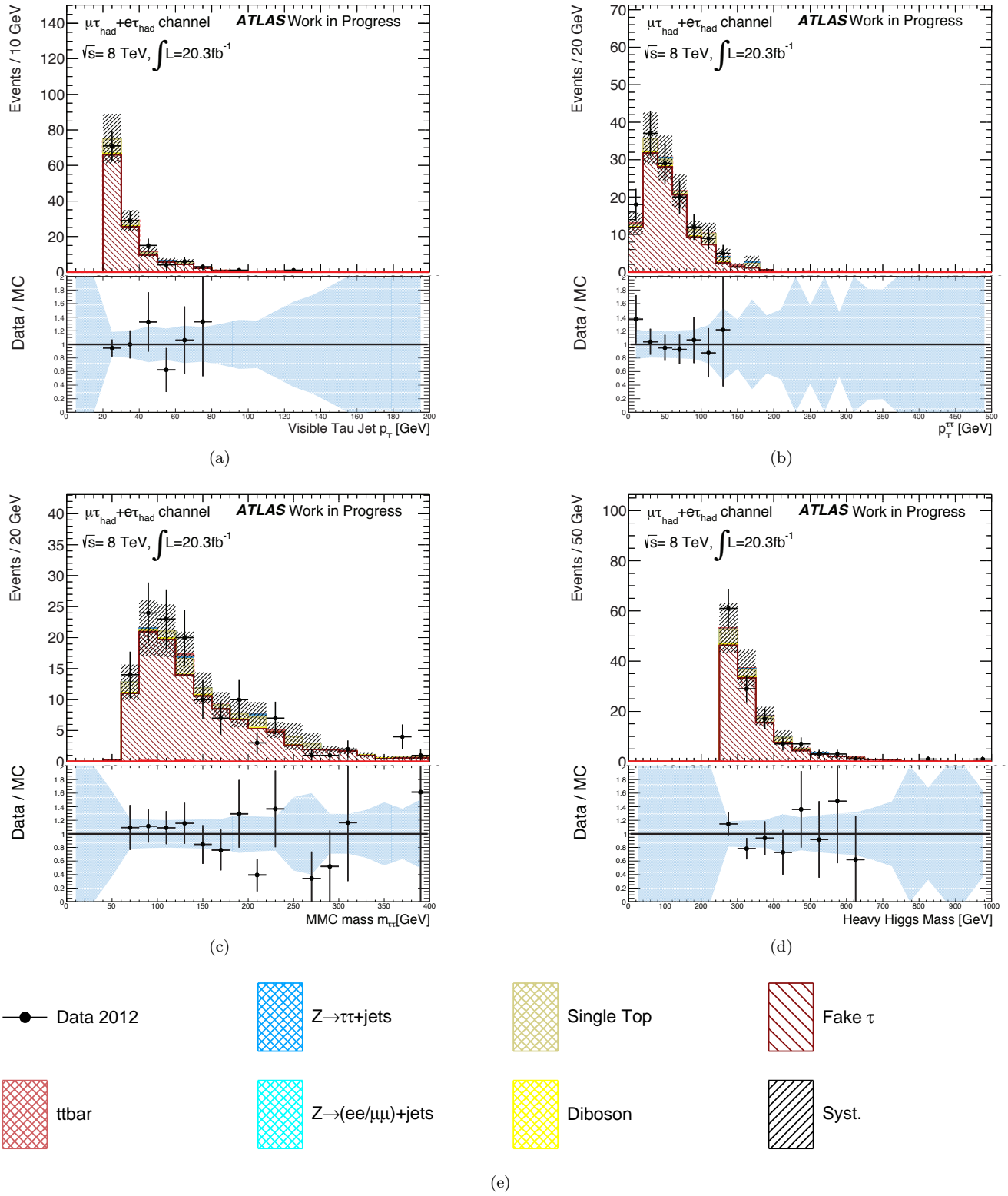


Figure 7.3: Kinematics distributions of (a) transverse momentum of τ_{had} , (b) transverse momentum of di-tau system, (c) invariant mass $m_{\tau^+\tau^-}$ reconstructed by MMC, and (d) invariant mass $m_{b\bar{b}\tau^+\tau^-}$ in same sign events for one b -tagged category. Background model enhanced fake background well agrees with same sign data. The shaded area indicates statistical and systematic uncertainty which includes ones of b -tag and fake estimation.

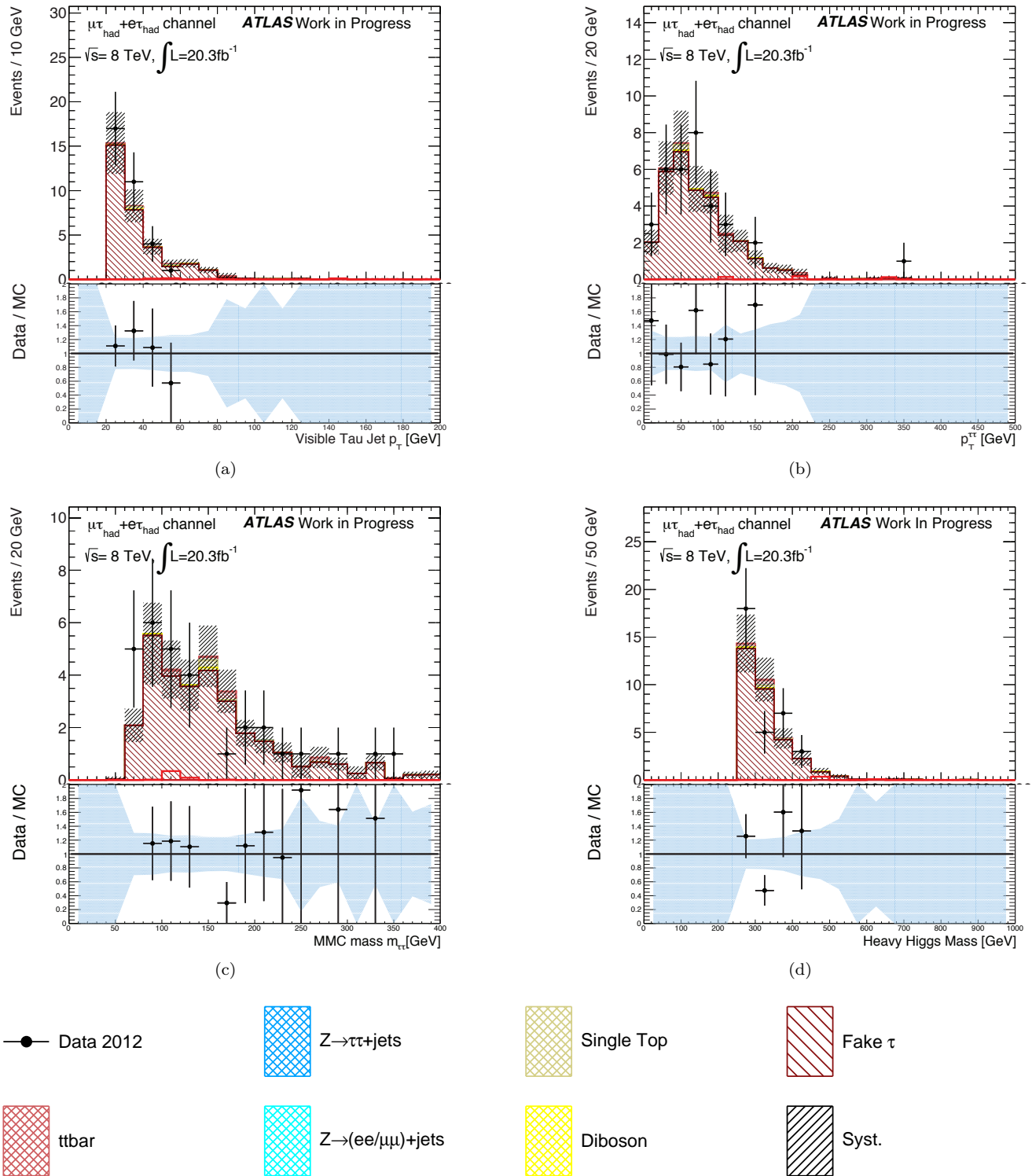


Figure 7.4: Kinematics distributions of (a) transverse momentum of τ_{had} , (b) transverse momentum of di-tau system, (c) invariant mass $m_{\tau^+\tau^-}$ reconstructed by MMC, and (d) invariant mass $m_{b\bar{b}\tau^+\tau^-}$ in same sign events for two b -tagged category. Background model enhanced fake background in same sign well agrees data. The shaded area indicates statistical and systematic uncertainty which includes ones of b -tag and fake estimation.

7.3 Top Background

The $t\bar{t}$ processes can be split to two background sources based on its decay types, semi-leptonic or di-leptonic decays. The semi-leptonic $t\bar{t}$ is a decay type including only one W^\pm boson from a top quark decaying leptonically, and in case of di-leptonic $t\bar{t}$, both W^\pm bosons from top quarks decay leptonically. For the semi-leptonic $t\bar{t}$, a tau object is provided from faking jet, and this is estimated by the fake factor method described in 7.2. On the other hand, di-leptonic $t\bar{t}$ is estimated from MC simulation applied all kind of scale factors for efficiency and the others.

Figure 7.5 shows some kinematic distributions for two b -tagged jet category in the Top control region which is defined by pre-selection with inverted $m_{b\bar{b}}$ mass window cut described in 6.3, and low/high tau $p_T^{\tau^+\tau^-}$ categories are merged here to keep enough event statistics. The total number of yields of estimated model in this region is 369 ± 37 and this number is consistent with the observed data of 360 events. And from these figures, the shapes of the kinematics distributions also can be seen reasonable agreement with estimated model.

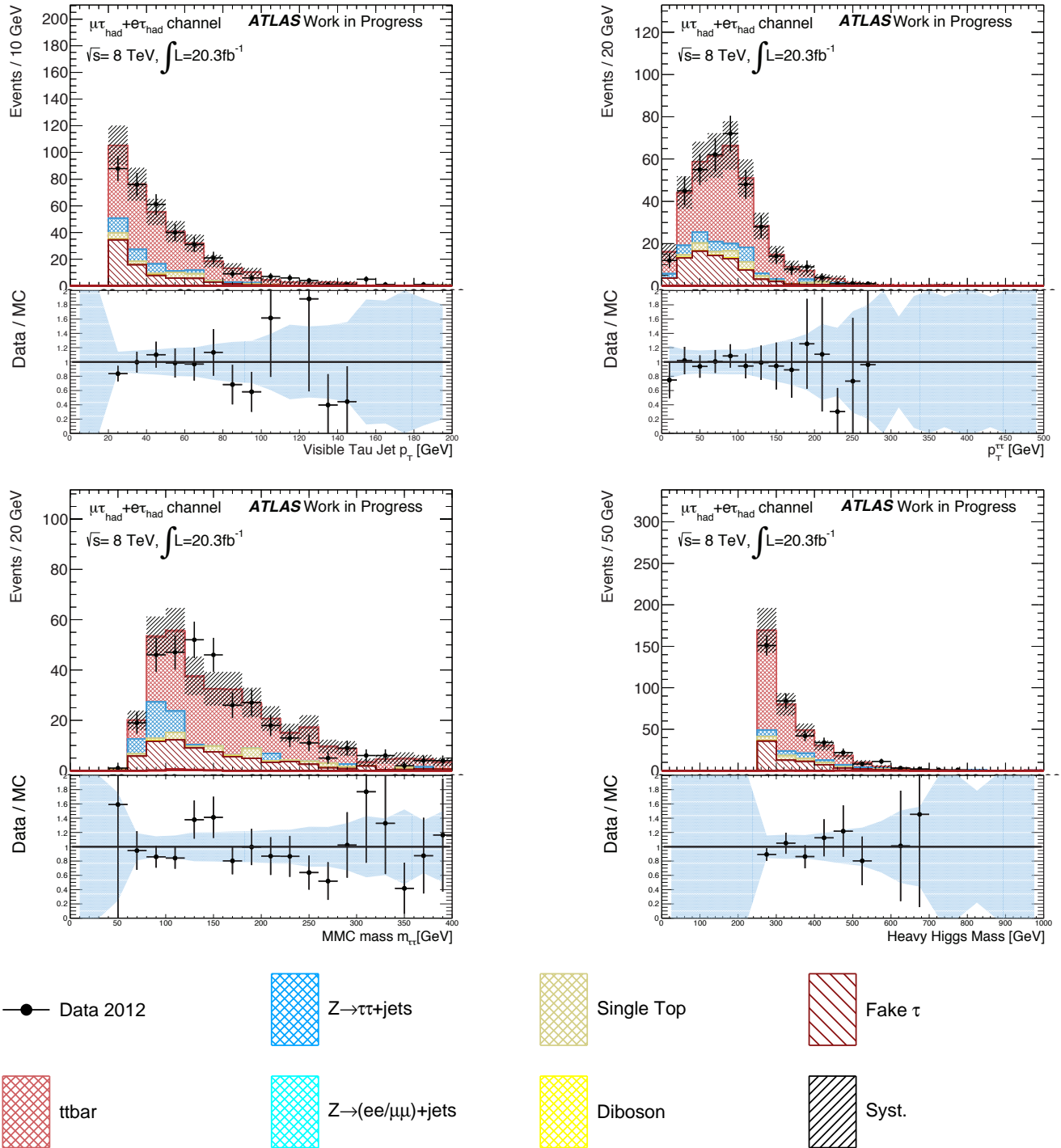


Figure 7.5: Kinematics distributions of (a) transverse momentum of transverse momentum of τ_{had} . (b) transverse momentum of di-tau system, (c) invariant mass $m_{\tau^+\tau^-}$ reconstructed by MMC, and (d) invariant mass $m_{b\bar{b}\tau^+\tau^-}$ in top control region. Background model enhanced $t\bar{t}$ background in same sign well agrees data.

7.4 $Z^0 \rightarrow \tau^+\tau^-$ Background

The estimation for $Z^0 \rightarrow \tau^+\tau^-$ background is very important in this analysis because of large contribution in the signal region. Therefore data-driven way with a part of simulation, so called embedding technique, is used for the estimation. The embedding sample is generated from $Z^0 \rightarrow \mu^+\mu^-$ data events with replacement muons to simulated τ leptons. The $Z^0 \rightarrow \mu^+\mu^-$ events are acquired by the selection described in Section 4.3. The τ kinematics is inherited from the two muons. The advantage of this method is what the systematic uncertainties related to jets, pile-up interactions and underlying events do not need to be considered.

7.5 Diboson and $Z^0 \rightarrow e^+e^-$ or $\mu^+\mu^-$ Background

The diboson and $Z^0 \rightarrow e^+e^-/\mu^+\mu^-$ backgrounds are estimated from MC simulation. The events of mis-identified fake τ_{had} from a jet are estimated from FF method described in Section 7.2 for $Z^0 \rightarrow e^+e^-/\mu^+\mu^-$, but MC simulation is used for the diboson background estimation because of tiny contribution.

7.6 The Events in Signal Region

The background events are estimated from the background estimation methods described in this section. The number of events for each background source after the event selection described in the Section 6.3 is summarized with data and signal in Tables. For the non-resonant searches, they are listed in Table 7.2 and Table 7.3 for one and two b -tagged jet categories, respectively. For the resonant search, they are listed in Table 7.4 and Table 7.5 for one and two b -tagged jet categories, respectively. In both non-resonant and resonant search, 1 pb is assumed as a signal cross section, and for resonant search heavy higgs of $m_H = 300$ GeV is listed. The numbers of second and third terms represent statistical uncertainty and systematic uncertainty, respectively. The systematic uncertainty is described in the next section. The dominant background sources come from $t\bar{t}$, $Z^0 \rightarrow \tau^+\tau^-$ and fake τ backgrounds for both non-resonant and resonant searches. The Figure 7.6 and 7.7 show the mass distributions of $m_{\tau^+\tau^-}$ reconstructed from MMC method and $m_{b\bar{b}\tau^+\tau^-}$ reconstructed from mass constrained method, respectively.

Table 7.2: Number of events in the OneB category of the $e\tau_h$ and $\mu\tau_h$ channels combined for non-resonant search, assuming signal cross section of 1 pb. Various background processes are estimated with the methods described in Section 7. Both statistical (first number) and systematic (second number) uncertainties are given.

Process	Number of Events	
	Low Higgs Pt	High Higgs Pt
Signal	$0.3 \pm 0.1 \pm 0.1$	$2.3 \pm 0.2 \pm 0.3$
$t\bar{t}$	$56.8 \pm 4.7 \pm 5.3$	$51.6 \pm 3.7 \pm 7.1$
SM higgs	$0.7 \pm 0.1 \pm 0.1$	$0.9 \pm 0.1 \pm 0.2$
$Z^0 \rightarrow \tau^+\tau^-$	$96.4 \pm 4.9 \pm 6.9$	$53.9 \pm 4.3 \pm 5.4$
others	$27.4 \pm 5.0 \pm 5.1$	$9.2 \pm 2.2 \pm 4.4$
Fake τ	$117.4 \pm 3.7 \pm 12.3$	$39.0 \pm 2.1 \pm 4.1$
Total	$298.7 \pm 9.2 \pm 15.9$	$154.6 \pm 6.4 \pm 10.8$
Data	266	157

Table 7.3: Number of events in the TwoB category of the $e\tau_h$ and $\mu\tau_h$ channels combined for non-resonant search, assuming signal cross section of 1 pb. Various background processes are estimated with the methods described in Section 7. Both statistical (first number) and systematic (second number) uncertainties are given.

Process	Number of Events	
	Low Higgs Pt	High Higgs Pt
Signal	$0.6 \pm 0.1 \pm 0.1$	$5.2 \pm 0.3 \pm 0.6$
$t\bar{t}$	$81.6 \pm 4.7 \pm 10.8$	$74.5 \pm 4.3 \pm 12.5$
SM higgs	$0.2 \pm 0.0 \pm 0.1$	$0.4 \pm 0.0 \pm 0.1$
$Z^0 \rightarrow \tau^+\tau^-$	$16.8 \pm 2.2 \pm 2.1$	$16.1 \pm 2.4 \pm 2.5$
others	$9.8 \pm 2.7 \pm 2.7$	$2.6 \pm 1.1 \pm 2.4$
Fake τ	$34.8 \pm 2.1 \pm 3.7$	$17.9 \pm 1.5 \pm 1.9$
Total	$143.1 \pm 6.2 \pm 11.9$	$111.5 \pm 5.3 \pm 13.1$
Data	118	117

Table 7.4: Number of events in the OneB category of the $e\tau_h$ and $\mu\tau_h$ channels combined for resonant search, assuming signal cross section of 1 pb. Various background processes are estimated with the methods described in Section 7. Both statistical (first number) and systematic (second number) uncertainties are given.

Process	Number of Events	
	Low Higgs Pt	High Higgs Pt
Signal(300)	$0.8 \pm 0.1 \pm 0.2$	$0.4 \pm 0.1 \pm 0.2$
$t\bar{t}$	$19.1 \pm 2.3 \pm 3.1$	$16.2 \pm 2.1 \pm 3.3$
SM higgs	$0.5 \pm 0.1 \pm 0.1$	$0.8 \pm 0.1 \pm 0.1$
$Z^0 \rightarrow \tau^+\tau^-$	$38.1 \pm 3.1 \pm 3.1$	$20.2 \pm 2.7 \pm 2.5$
others	$14.3 \pm 3.7 \pm 2.5$	$3.9 \pm 1.5 \pm 1.5$
Fake τ	$37.0 \pm 2.1 \pm 3.9$	$12.1 \pm 1.2 \pm 1.3$
Total	$109.1 \pm 5.8 \pm 6.4$	$53.1 \pm 3.9 \pm 4.6$
Data	92	46

Table 7.5: Number of events in the TwoB category of the $e\tau_h$ and $\mu\tau_h$ channels combined for resonant search, assuming signal cross section of 1 pb. Various background processes are estimated with the methods described in Section 7. Both statistical (first number) and systematic (second number) uncertainties are given.

Process	Number of Events	
	Low Higgs Pt	High Higgs Pt
Signal(300)	$1.5 \pm 0.2 \pm 0.2$	$0.8 \pm 0.1 \pm 0.2$
$t\bar{t}$	$28.3 \pm 2.7 \pm 6.4$	$22.7 \pm 2.4 \pm 4.5$
SM higgs	$0.1 \pm 0.0 \pm 0.1$	$0.2 \pm 0.0 \pm 0.1$
$Z^0 \rightarrow \tau^+\tau^-$	$6.8 \pm 1.4 \pm 1.2$	$2.6 \pm 0.8 \pm 0.6$
others	$3.4 \pm 1.6 \pm 3.0$	$1.2 \pm 0.7 \pm 0.4$
Fake τ	$13.7 \pm 1.3 \pm 1.4$	$5.4 \pm 0.8 \pm 0.6$
Total	$52.2 \pm 3.7 \pm 7.3$	$32.1 \pm 2.7 \pm 4.6$
Data	35	35

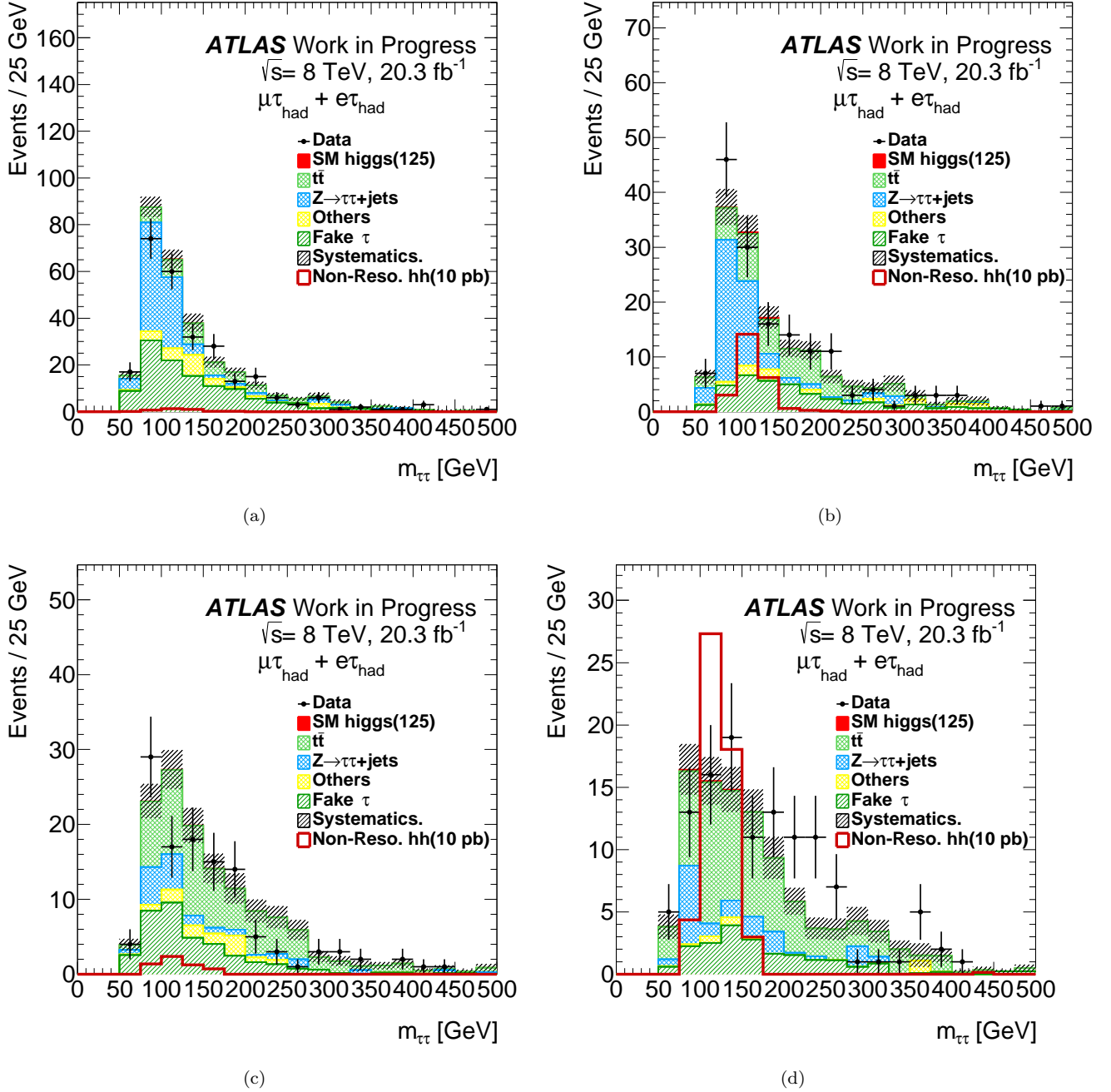


Figure 7.6: The $m_{\tau^+\tau^-}$ distribution reconstructed from MMC method after the non-resonant search selections in each of categories, (a) one b -tagged and $p_T^{\tau^+\tau^-} < 100 \text{ GeV}$, (b) one b -tagged and $p_T^{\tau^+\tau^-} > 100 \text{ GeV}$, (c) two b -tagged and $p_T^{\tau^+\tau^-} < 100 \text{ GeV}$, and (d) two b -tagged and $p_T^{\tau^+\tau^-} > 100 \text{ GeV}$.

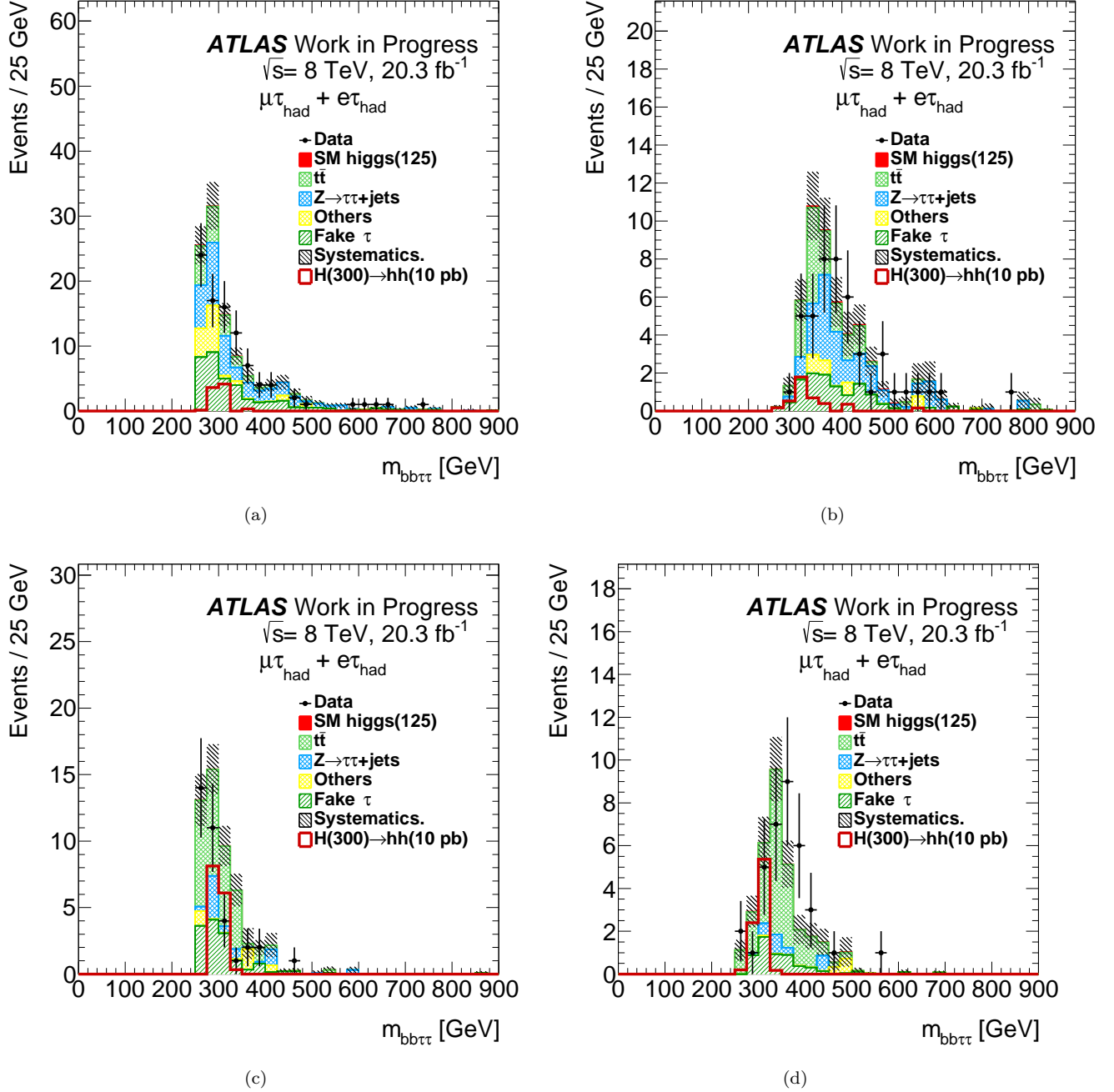


Figure 7.7: The $m_{b\bar{b}\tau^+\tau^-}$ distribution reconstructed from constrained mass method after the resonant search selections in each of categories, (a) one b -tagged and $p_T^{\tau^+\tau^-} < 100 \text{ GeV}$, (b) one b -tagged and $p_T^{\tau^+\tau^-} > 100 \text{ GeV}$, (c) two b -tagged and $p_T^{\tau^+\tau^-} < 100 \text{ GeV}$, and (d) two b -tagged and $p_T^{\tau^+\tau^-} > 100 \text{ GeV}$.

Chapter 8

Systematic Uncertainties

8.1 Theoretical Systematic Uncertainties

QCD scale and PDF

Theoretical cross sections for some tiny contributing backgrounds are used for the normalization. Table 8.1 shows the uncertainties assigned for each backgrounds. The uncertainties of QCD scale are shown as QCDScale_XX, with XX being V and VV standing for a Gauge Boson and di-boson, respectively [62]. The PDF uncertainty is also assigned [63].

Table 8.1: Summary of theory uncertainties for the background process normalizations.

Background	Uncertainty	
$t\bar{t}$	QCDScale_ttbar	6%
$t\bar{t}$	pdf_gg	2%
diboson	QCDScale_VV	5%
$Z^0 \rightarrow \ell\ell$	QCDScale_V	1%
$Z^0 \rightarrow \ell\ell$ and VV	pdf_qq	4%

8.2 Experimental Systematic Uncertainties

8.2.1 Electron

- **Reconstruction and Identification:**
The correction factors of the single electron trigger and the reconstruction and identification efficiencies are applied for the MC simulation samples for both signal and background processes. Their systematic uncertainties are assigned and evaluated to be 3% [39]. The impact of the propagation from these uncertainties is estimated by varying them within one upper or lower standard deviation.
- **Calorimeter Isolation:**
The correction factors of isolation are applied for the MC simulation samples for both signal and background processes. The isolation requirement efficiencies are estimated by the study with tag-and-probe method and the uncertainty of $\pm 2\%$ for electron $p_T > 20$ GeV and $\pm 4\%$ for electron $p_T < 20$ GeV are assigned [39]. The impact of the propagation from the their uncertainties estimated by varying them within one upper and lower standard deviation.
- **Energy Scale and Resolution:**
The correction factors of energy scale and resolution are applied to the MC for both signal and background processes. The factors are estimated by comparing between MC simulation and $Z^0 \rightarrow e^+e^-$ events on data. The uncertainty of $\pm 1\%$ for central region and $\pm 3\%$ for forward region are assigned.

8.2.2 Muon

- **Reconstruction and Identification:**
The correction factors of the single muon trigger and the reconstruction and identification efficiencies are applied for the MC simulation samples for both signal and background processes. Their systematic uncertainties are assigned and evaluated to be 1% [41]. The impact of the propagation from these uncertainties is estimated by varying them within one upper or lower standard deviation.
- **Momentum Resolution:**
The correction factors of energy scale and resolution are applied to the MC for both signal and background processes. The factors are estimated by comparing between MC simulation and $Z^0 \rightarrow \mu^+\mu^-$ events on data. The uncertainty of $\pm 1\%$ for central region and $\pm 3\%$ for forward region are assigned.

8.2.3 Hadronic- τ

- **Identification:**
The correction factor of τ identification efficiency is applied to MC simulation samples. The factor is obtained by tag-and-probe method of $Z^0 \rightarrow \tau^+\tau^-$ events, and its systematic uncertainty is assigned. The correction factors on the rate of misidentification efficiency and its scale factor is estimated from $Z^0 \rightarrow e^+e^-(e \rightarrow \tau_{\text{had}})$ events. The systematic uncertainties on the scale factor is depended on the p_T and $|\eta|$. The impact of the propagation from the uncertainties is estimated by varying them within one upper or lower standard deviation.
- **Energy Scale:**
The tau energy scale is determined by resonant fitting to visible mass of $Z^0 \rightarrow \tau^+\tau^-$ events, and the systematic uncertainties are estimated. [64]. TES uncertainties are measured with a precision of $\pm 2 - \pm 4\%$. The TES uncertainty is divided into four uncorrelated parts:

- In-situ interpolation on true taus:
uncertainty of the in-situ energy scale, relevant mainly for $p_T < 50$ GeV.
- Single particle interpolation on true taus:
uncertainty of the particle decomposition component, relevant mainly for $p_T < 70$ GeV.
- Modeling on true taus:
sum of many components related to modeling of pile-up, underlying event, dead material and physics lists.
- fake taus:
A single systematic uncertainty is assigned for fake taus, and treated uncorrelated to the TES uncertainties on true taus.

8.2.4 Jet

The JES uncertainty is given as following uncorrelated components:

- In-situ energy correction
- η inter-calibration
- high- p_T jets
- Non-closure
- Flavour composition and response for light jets
- b-jets
- Pile-up

The total uncertainty is shown in Figure 8.1. The MC modeling is one of the main source of the

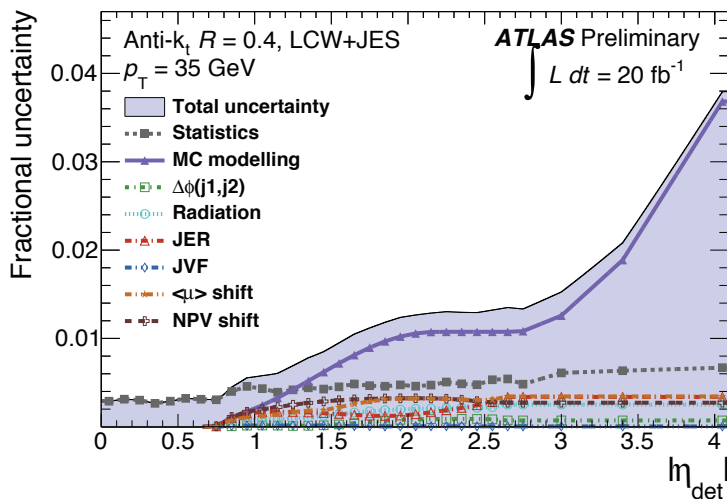


Figure 8.1: Uncertainties on the JES as a function of the jet $|\eta|$ in $p_T = 35$ GeV [49].

uncertainties. It is evaluated from the difference of the generator, Sherpa and PowhegPythia8. The comparison of the Sherpa and PowhegPythia8 is shown in the Figure 8.2.

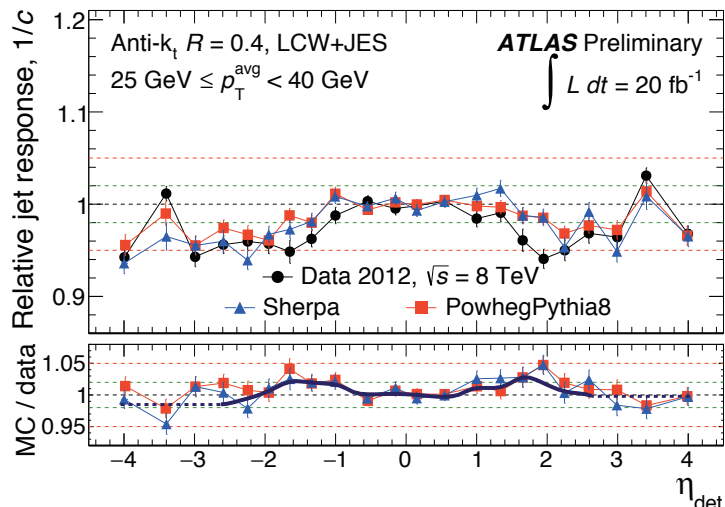


Figure 8.2: Relative jet response $1/c$ as a function of jet η in the p_T slice from 25 GeV to 40 GeV [49].

8.2.5 Missing Transverse Energy

The E_T^{miss} calculation depends on the other objects, therefore their uncertainties propagate to the E_T^{miss} uncertainty. And E_T^{miss} soft term scale and resolution are considered as the E_T^{miss} uncertainty.

8.2.6 Trigger

The scale factors of both single electron and single muon lepton trigger are applied. The uncertainties of them are about 1-2% depending on the transverse momentum and pseudo rapidity.

8.2.7 Luminosity

The systematic uncertainty on the integrated luminosity of $\pm 2.8\%$ is evaluated from beam-separation scans and is assigned for the 8 TeV 20.3 fb^{-1} dataset.

8.2.8 Fake Background

The fake τ background is estimated by FF method described in 7.2. The systematic uncertainties comes from the composition fraction R_i (i stands for each processes, W +jets, Z +jets, QCD jets and Top). The $\pm 50\%$ uncertainty is assigned for the fraction. The impact from this uncertainty is estimated by varying this fractional uncertainty, and is estimated to be $\pm 9.5\%$. The $\pm 5.1\%$ is assigned for statistical uncertainty. These uncertainties are summarized in Table 8.2

Table 8.2: The uncertainty for fake background.

Source	uncertainty[%]
total	10.8
composition	9.5
statistical	5.1

8.2.9 Estimation of $Z^0 \rightarrow \tau^+\tau^- + \text{jets}$ with Embedding Method

$Z^0 \rightarrow \tau^+\tau^- + \text{jets}$ backgrounds are estimated by embedding technique. The systematic uncertainties are composed of three components, $Z^0 \rightarrow \mu^+\mu^-$ event selection, replacement of muons with simulation taus, and subtraction of $t\bar{t}$.

- $Z^0 \rightarrow \mu^+\mu^-$ event selection:
The uncertainties from isolation requirement on $Z^0 \rightarrow \mu^+\mu^-$ event selection is evaluated from comparing the nominal isolation requirement ($\sum_{\text{tracks}}^{\Delta R \leq 0.2} p_{T,\text{track}}/p_{T,\mu} < 0.2$) with other criteria, tighter isolation requirement ($\sum_{\text{tracks}}^{\Delta R \leq 0.2} p_{T,\text{track}}/p_{T,\mu} < 0.06$) and no-isolation requirement.
- replacement of muons with simulation taus:
The calorimeter cells which is to be associated is expected from MC simulation, and subtracted in the replacement of muon to simulation tau. The subtraction systematics are assigned by scaling up and down with 20% for each cell energy.
- subtraction of $t\bar{t}$:
The systematic uncertainty of 15% is assigned for the subtraction of $t\bar{t}$ process described in Selection 4.3.1.

8.2.10 Estimation of Top Background

The uncertainty of $t\bar{t}$ events in signal region is extrapolated from top control region. The uncertainty is estimated from the difference of the generator, between the generator Powheg and MC@NLO. The difference of the event yields fraction of signal region and control for each generators is assigned as the uncertainty. The systematic uncertainties of 2.0% and 7.9% are assigned for Low and High $p_T^{\tau^+\tau^-}$ category respectively, for both resonant and non-resonant searches.

Chapter 9

Results

The signal events are extracted by a maximum likelihood fit on the $m_{\tau+\tau^-}$ and $m_{b\bar{b}\tau+\tau^-}$ distributions for non-resonant and resonant searches, respectively.

9.1 Fit Method for The Background and Signal

The profile likelihood method performed for the limit setting on the cross section is introduced. The likelihood function is given as:

$$\mathcal{L}(\mu, \vec{\beta}_{\text{samp}}, \vec{\theta}_s, \vec{\theta}_b, \vec{\theta}_{\text{global}}) = \text{Pois}(n|\mu_T) \text{Pois}(n_{\text{samp}}|\beta_{\text{samp}}) \mathcal{L}(\vec{\theta}_s, \vec{\theta}_b, \vec{\theta}_{\text{global}}), \quad (9.1)$$

where:

- function ‘‘Pois’’ stands for the poisson distribution
- n is the number of events in the signal region
- $\vec{\beta}_{\text{samp}}$ are the statistical uncertainties of the MC or data driven control sample events, using the initial event numbers (n_{samp}), before scaling to the cross section
- $\vec{\theta}_{s,b}$ are the specific nuisance parameters related to the signal and the background, such as the efficiency and the cross section uncertainties
- $\vec{\theta}_{\text{global}}$ represent the common nuisance parameters which are correlated between channels, such as the luminosity uncertainty
- μ_T is the total number of expected events given by

$$\mu_T = \sum_{l=1}^4 \mu L \sigma_l(m_H) f_s(\vec{\theta}_s) f_g(\vec{\theta}_{\text{global}}) + \sum_j L \beta_j f_b(\vec{\theta}_b) f_g(\vec{\theta}_{\text{global}}), \quad (9.2)$$

where

- L is the nominal integrated luminosity
- μ is the one parameter of interest e.g., the scaling factor for the expected signal rate (signal strength)
- $\sigma_l(m_H)$ is the effective cross section (in pb) for signal events
- β_j is the nominal effective cross section (in pb) for background j (including β_{samp})
- $f_{s,b,\text{global}}$ represent the dependence of the expected number of events on the various nuisance parameters.

The likelihood is used to construct a statistical test based on the profile-likelihood ratio and asymptotic formulae [65] are used when appropriate. The statistical test is given by

$$\tilde{q}_\mu = \begin{cases} -2 \ln \frac{L(\mu, \hat{\vec{\theta}}(\mu))}{L(0, \hat{\vec{\theta}}(0))} & \hat{\mu} < 0, \\ -2 \ln \frac{L(\mu, \hat{\vec{\theta}}(\mu))}{L(\hat{\mu}, \hat{\vec{\theta}})} & 0 \leq \hat{\mu} \leq \mu, \\ 0 & \hat{\mu} > \mu. \end{cases} \quad (9.3)$$

where

- $\vec{\theta}$ represent the nuisance parameters: $\hat{\mu}$, $\hat{\vec{\theta}}$ evaluated at μ
- $\hat{\vec{\theta}}(\mu)$ are the Maximum Likelihood Estimators (MLE) of μ , $\vec{\theta}$.

For computing statistical significance, the background-only p -value is computed from the test statistic q_0 .

$$p_0 = \int_{q_{0,\text{obs}}}^{\infty} f(q_0|0, \hat{\theta}_0) dq_0 \quad (9.4)$$

9.2 Result of Non-Resonant Analysis

The limits for the non-resonant search is derived in this section using the techniques for the limit-setting described in the previous section. The MMC distributions shown in the Figure 7.6 are used as a final discriminant. The expected exclusion with 95% confidence level (CL) limit is 1.3 pb. And the observed 95% CL exclusion limit is 1.6 pb. It is summarized in Table 9.1 showing observed and expected 95% CL limits. This limit is corresponding to the 130 times cross section of $gg \rightarrow hh$ predicted within standard model of 9.9 ± 1.3 fb [66]. If the signal cross section of 1 pb is assumed, the local signal significance p_0 is -0.56σ for the expectation of 1.3σ . It is summarized in Table 9.2.

Table 9.1: Observed and expected 95% confidence level upper limits (UL) for non-resonant search.

Category	Observed	Expected UL
Combined	1.60 pb	1.31 pb
TwoB	1.40 pb	1.70 pb
OneB	4.47 pb	4.75 pb

The major uncertainties on the signal strength are summarized in Table 9.3. The leading uncertainty is statistical uncertainty of the data. The jet energy scale and resolution contribute most to the signal strength estimation.

Table 9.2: Observed and expected local significance, p_0 , in non-resonant search, for each categories, assuming signal cross section is 1 pb.

Category	Observed p_0	Expected p_0
Combined	-0.56σ	1.30σ
TwoB	-0.56σ	1.23σ
OneB	-0.20σ	0.47σ

Table 9.3: The effect of the most important sources of uncertainty on the signal strength parameter, for the non-resonant signal.

Source of uncertainty	Uncertainty on μ [%]
Data statistics	61.2
Jet energy scale and resolution	25.2
Background Model	11.3
b-jet tag	11.1
Tau	9.4
Branching ratio	6.8
Total systematics	33.1

9.3 Result of Resonant Analysis

The resonant search is derived for the range of 260-1000 GeV. The limits for the resonant search is set on the cross section $gg \rightarrow H$ production of the heavy Higgs boson times branching ration of $\text{BR}(H \rightarrow hh)$ as a function of the mass of the heavy Higgs boson m_H . The $m_{b\bar{b}\tau^+\tau^-}$ distributions shown in Figure 7.7 are used as a final discriminant. The expected exclusions on 95% CL are 3.1, 0.66 and 0.28 pb for the heavy higgs mass of $m_H = 300, 500$ and 1000 GeV, respectively. And the observed exclusions on 95% CL are 1.7, 1.0 and 0.46 pb for $m_H = 300, 500$ and 1000 GeV, respectively. They are summarized in Table 9.4 and illustrated in Figure 9.1. Since a deficit can be seen in the $m_{b\bar{b}\tau^+\tau^-}$ distribution, the observed limit around $m_H = 300$ GeV is appreciably lower than the expectation.

The local significance assuming signal cross section of 1 pb are summarized in Table 9.5 and Figure 9.2..

The major uncertainties on the signal strength for the resonant mass of $m_H = 260, 400, 500$ and 1000 GeV are summarized in Table 9.6 to 9.9.

Table 9.4: Observed and expected 95% confidence level upper limits (UL) for each mass point for the 1b-tag and 2-btag combined.

mass [GeV]	Observed UL	Expected UL
260	4.2 pb	2.6 pb
280	3.2 pb	3.7 pb
300	1.7 pb	3.1 pb
350	2.8 pb	2.2 pb
400	1.5 pb	0.97 pb
500	1.0 pb	0.66 pb
800	0.51 pb	0.31 pb
1000	0.46 pb	0.28 pb

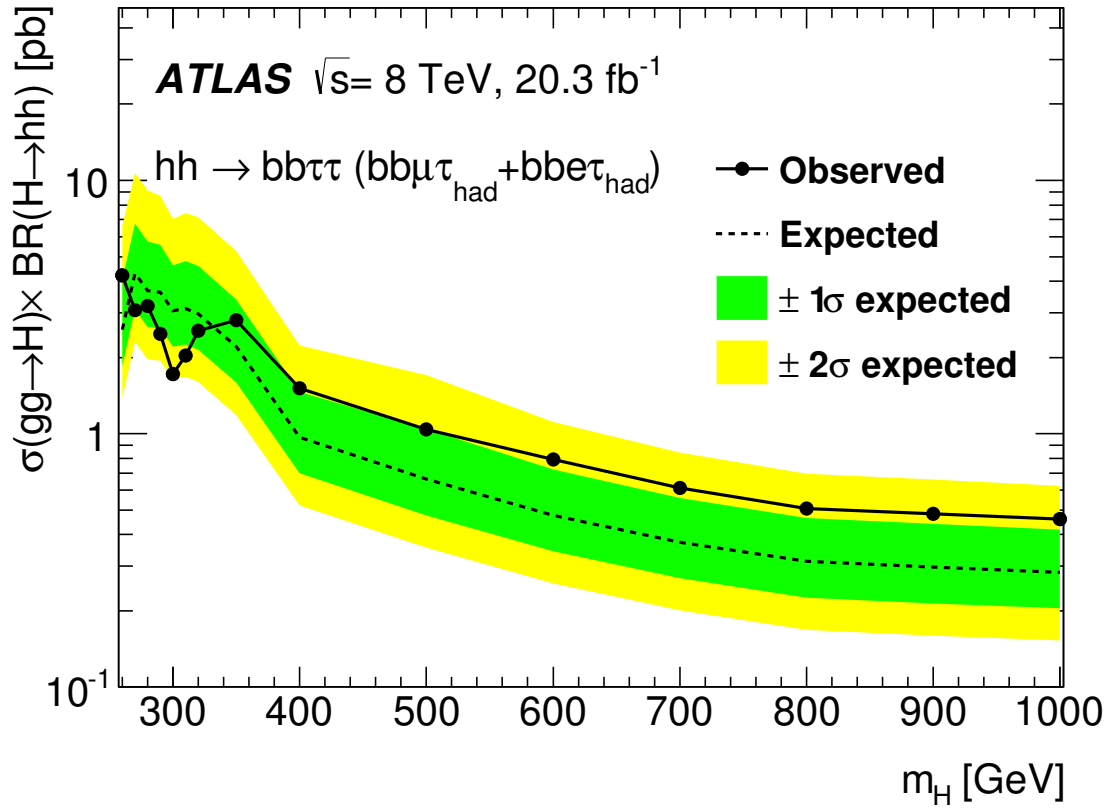


Figure 9.1: Observed (solid line) and expected (dashed line) 95% CL limits as a function of resonant mass for category combination. Green and yellow bands represent the ± 1 and 2σ deviation.

Table 9.5: Observed and expected local significance, p_0 , for each mass point for the combination, assuming signal cross section is 1 pb.

mass [GeV]	Observed p_0	Expected p_0
260	1.7σ	1.2σ
280	-0.14σ	0.75σ
300	-1.7σ	0.84σ
350	0.69σ	1.1σ
400	1.2σ	2.1σ
500	1.3σ	2.9σ
800	1.3σ	4.5σ
1000	1.4σ	4.8σ

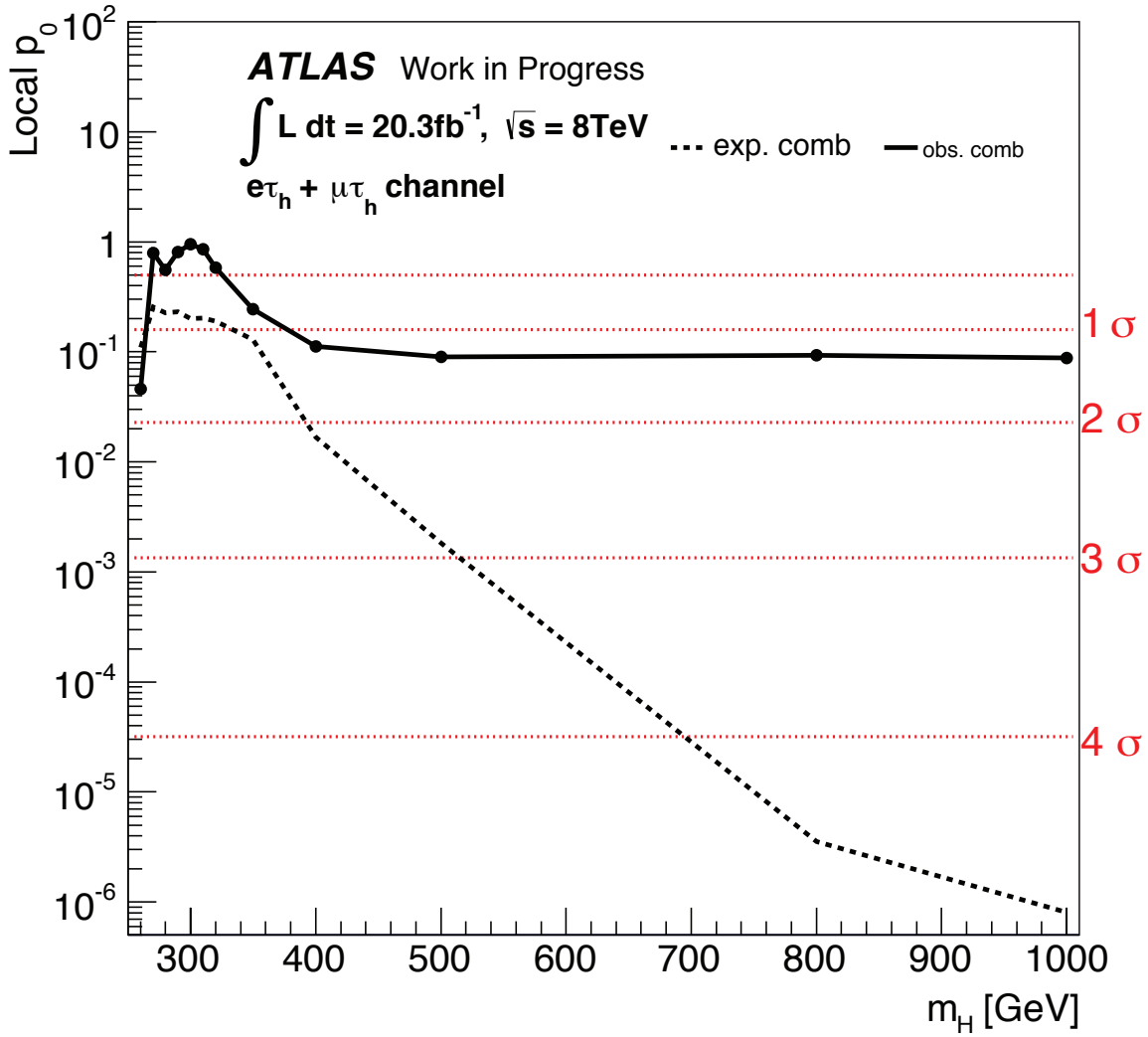


Figure 9.2: Observed (solid line) and expected (dashed line) local significance, p_0 , as a function of resonant mass for category combination, assuming signal cross section is 1 pb.

Table 9.6: The effect of the most important sources of uncertainty on the signal strength parameter, for the resonant 260 GeV signal.

Source of uncertainty	Uncertainty on μ [%]
Data statistics	90.1
Jet energy scale and resolution	25.7
Missing Et	9.6
b-jet tag	7.8
Branching ratio	7.5
Lepton	7.0
Total systematics	31.9

Table 9.7: The effect of the most important sources of uncertainty on the signal strength parameter, for the resonant 400 GeV signal.

Source of uncertainty	Uncertainty on μ [%]
Data statistics	45.9
Jet energy scale and resolution	16.1
Tau	11.1
Branching ratio	6.7
b-jet tag	5.2
Signal theory	4.5
Total systematics	22.5

Table 9.8: The effect of the most important sources of uncertainty on the signal strength parameter, for the resonant 500 GeV signal.

Source of uncertainty	Uncertainty on μ [%]
Data statistics	31.4
Jet energy scale and resolution	20.3
Tau	9.4
Lepton	7.4
Branching ratio	6.7
Signal theory	4.5
Total systematics	25.3

Table 9.9: The effect of the most important sources of uncertainty on the signal strength parameter, for the resonant 1000 GeV signal.

Source of uncertainty	Uncertainty on μ [%]
Data statistics	22.0
b-jet tag	7.3
Branching ratio	6.6
Tau	4.9
Jet energy scale and resolution	3.8
Luminosity	2.5
Total systematics	12.8

Chapter 10

Combination with Other Analysis Channels

In order to achieve better sensitivity for the search of di-higgs production, the results of all analysis channels $hh \rightarrow b\bar{b}\tau^+\tau^-$, $\gamma\gamma WW$, $\gamma\gamma b\bar{b}$, $b\bar{b}b\bar{b}$ have been combined [67]. The results of $hh \rightarrow \gamma\gamma b\bar{b}$ [68] and $hh \rightarrow b\bar{b}b\bar{b}$ [69] channels have been reported in stand alone analysis. The results of each analysis channel are described in Appendix C. In this section the results of these channels and combination of all channels are described.

10.1 Result of Non-Resonant Analysis

In the non-resonant search, the combined observed and expected 95% CL exclusions on the di-higgs cross sections are 0.47 and 0.69 pb corresponding to 70(48) times the standard model cross section predictions. It is summarized in Table 10.1. The most sensitive channel is $hh \rightarrow b\bar{b}b\bar{b}$ channel. The observed combined limit is slightly weaker than expected. This is largely due to the result of $hh \rightarrow \gamma\gamma b\bar{b}$ analysis where some excess of events is observed [68].

Table 10.1: The expected and observed 95% CL upper limits on the cross sections of non-resonant $gg \rightarrow hh$ production at $\sqrt{s} = 8$ TeV from individual analyses and their combinations. SM values are assumed for the h decay branching ratios. The cross-section limits normalized to the SM value are also included.

Analysis	$\gamma\gamma b\bar{b}$	$\gamma\gamma WW^*$	$b\bar{b}\tau^+\tau^-$	$b\bar{b}b\bar{b}$	Combined
Upper limit on the cross section [pb]					
Expected	1.0	6.7	1.3	0.62	0.47
Observed	2.2	11	1.6	0.62	0.69
Upper limit on the cross section relative to the SM prediction					
Expected	100	680	130	63	48
Observed	220	1150	160	63	70

10.2 Result of Resonant Analysis

The mass ranges used for the combination are summarized in Table 10.2. The combined limit of the resonant search is summarized in the Table 10.3 and Figure 10.1. The most significant excess

Table 10.2: The mass ranges used for the search in each channel.

channel	$\gamma\gamma b\bar{b}$	$\gamma\gamma WW^*$	$bb\tau^+\tau^-$	$bbbb$
mass range	260 - 500 [GeV]	260 - 500 [GeV]	260 - 1000 [GeV]	500 - 1000 [GeV]

is corresponding to a mass point of 300 GeV in the combined results. The local significance of 3.0σ in $hh \rightarrow \gamma\gamma b\bar{b}$ analysis is dominating.

 Table 10.3: The expected and observed 95% CL upper limits on $\sigma(gg \rightarrow H) \times \text{BR}(H \rightarrow hh)$ in pb at $\sqrt{s} = 8$ TeV from individual analyses and their combinations. The SM branching ratios are assumed same for the light Higgs boson decay.

m_H [GeV]	Expected limit [pb]					Observed limit [pb]				
	$\gamma\gamma b\bar{b}$	$\gamma\gamma WW^*$	$bb\tau^+\tau^-$	$bbbb$	Combined	$\gamma\gamma b\bar{b}$	$\gamma\gamma WW^*$	$bb\tau^+\tau^-$	$bbbb$	Combined
260	1.70	11.2	2.6	–	1.1	2.29	18.7	4.2	–	2.1
300	1.53	9.3	3.1	–	1.2	3.54	15.1	1.7	–	2.0
350	1.23	7.8	2.2	–	0.89	1.44	13.3	2.8	–	1.5
400	1.00	6.9	0.97	–	0.56	1.00	11.5	1.5	–	0.83
500	0.72	5.9	0.66	–	0.38	0.71	10.9	1.0	–	0.61
500	–	–	0.66	0.17	0.16	–	–	1.0	0.16	0.18
600	–	–	0.48	0.070	0.067	–	–	0.79	0.072	0.079
700	–	–	0.31	0.041	0.040	–	–	0.61	0.038	0.040
800	–	–	0.31	0.028	0.028	–	–	0.51	0.046	0.049
900	–	–	0.30	0.022	0.022	–	–	0.48	0.015	0.015
1000	–	–	0.28	0.018	0.018	–	–	0.46	0.011	0.011

The upper cross section limits of the resonant search gives the exclusion for the parameter spaces in the hMSSM [70, 71] and low-tb-high [72] scenarios of MSSM. In this interpretation, the CP-even light higgs boson in MSSM is assumed to h and CP-even heavy higgs boson in MSSM is corresponding to H , respectively. Since the di-higgs production rate depends on $\tan\beta$ and the mass of the CP-odd Higgs boson (m_A) in both scenarios, the upper limits on di-higgs can give the exclusion for the parameter space of $(\tan\beta, m_A)$. The analysis has sensitivity for the low $\tan\beta$ and m_A region ~ 200 -350 GeV. $H \rightarrow hh$ decay is strongly suppressed for lower and higher than this mass, because of out of range from $2 \times m_h$ to $2 \times m_{top}$. Figure 10.2 shows the exclusion in the parameter space of $(\tan\beta, m_A)$.

The observed exclusion region is smaller than expected, because of small excess observed in $hh \rightarrow \gamma\gamma b\bar{b}$.

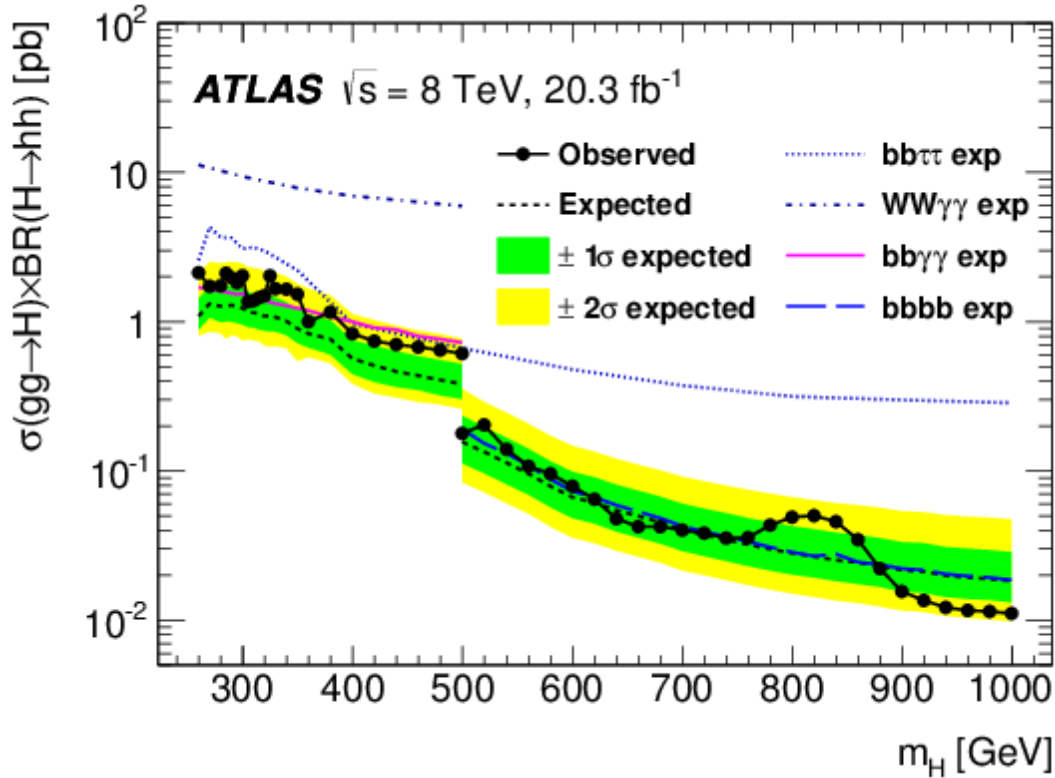


Figure 10.1: The observed and expected 95% CL upper limits on $\sigma(gg \rightarrow H) \times BR(H \rightarrow hh)$. $hh \rightarrow b\bar{b}\tau^+\tau^-$, $\gamma\gamma WW$, $\gamma\gamma b\bar{b}$, $b\bar{b}b\bar{b}$ are combined.

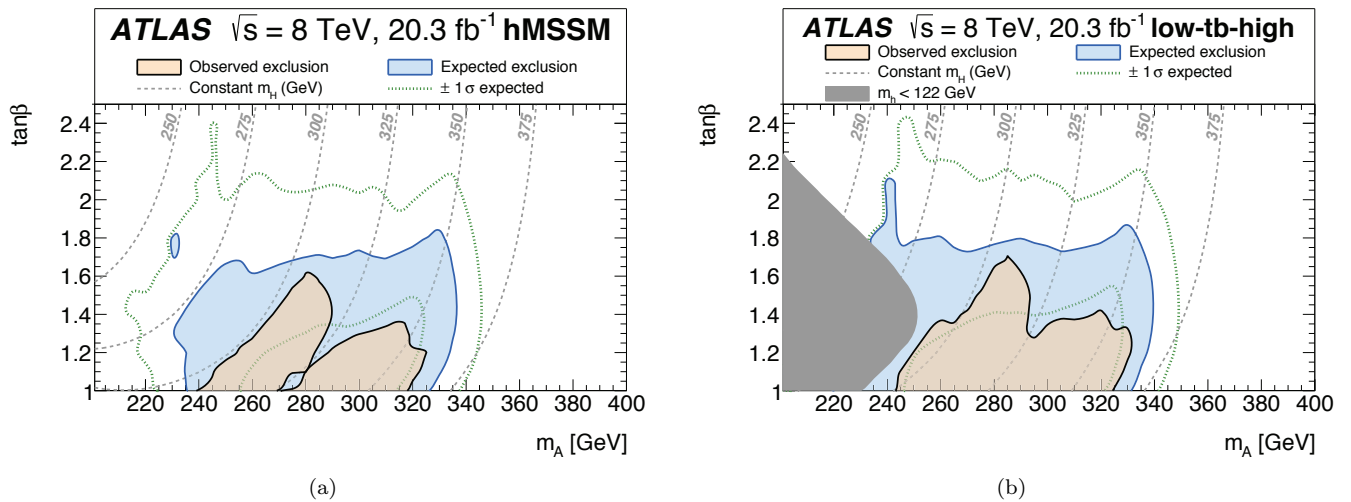


Figure 10.2: (a) hMSSM scenario and (b) low-tb-high scenario. [67]

Chapter 11

Conclusions

We have searched for di-higgs production in $hh \rightarrow b\bar{b}\tau^+\tau^-$ decay channel for both non-resonant and resonant di-higgs production scenarios using proton-proton collision data amount to 20.3 fb^{-1} at $\sqrt{s} = 8 \text{ TeV}$ recorded with the ATLAS detector. This analysis is motivated for the searches including beyond standard model, while this channel is potentially very important for future search of higgs self-coupling decays. No excess is observed in both non-resonant and resonant searches. For the non-resonant search the observed and expected 95% CL limits are 1.60 pb (corresponding to 160 times σ_{hh}^{SM}) and 1.31 pb. For the resonant search the observed 95% CL limits varied with m_H from 4.2 pb to 0.46 pb for the resonance mass region from 260 GeV to 1000 GeV.

The $hh \rightarrow b\bar{b}\tau^+\tau^-$ channel is combined to other channels, $hh \rightarrow \gamma\gamma WW, \gamma\gamma b\bar{b}, b\bar{b}b\bar{b}$. The $hh \rightarrow b\bar{b}\tau^+\tau^-$ is third sensitive channel for the non-resonant search, 30% worse than second sensitive channel $\gamma\gamma b\bar{b}$. Improvement of $hh \rightarrow b\bar{b}\tau^+\tau^-$ is foreseen by including other $\tau^+\tau^-$ decays, all-hadronic- and leptonic- decay channels. For the resonant mass from about 400 to 500 GeV, $hh \rightarrow b\bar{b}\tau^+\tau^-$ is most sensitive channel.

Appendix A

Tau Identification Variables

- Central energy fraction (f_{cent}):
The fraction of transverse energy deposited around the τ_{had} candidate with cone size of $\Delta R < 0.1$ and $\Delta R < 0.2$.

$$f_{\text{cent}} = \frac{\sum_{i \in \text{all}}^{\Delta R_i < 0.1} E_{T,i}}{\sum_{j \in \text{all}}^{\Delta R_i < 0.2} E_{T,j}} \quad (\text{A.1})$$

- Leading track momentum fraction (f_{track}):
The fraction of the momentum of the τ_{had} candidate attributed to the track and the total momentum of the candidate.

$$f_{\text{track}} = \frac{p_{T,1}^{\text{track}}}{p_T^T} \quad (\text{A.2})$$

- Track radius (R_{track}):
distance of the associated tracks to the direction of the τ_{had} candidate weighted with p_T , using all tracks in the core and isolation regions.

$$R_{\text{track}} = \frac{\sum_i^{\Delta R_i < 0.4} p_{T,i} \Delta R_i}{\sum_i^{\Delta R_i < 0.4} p_{T,i}} \quad (\text{A.3})$$

- Leading track IP significance ($S_{\text{lead-track}}$):
Transverse impact parameter of the highest p_T track in the core region, using the tau vertex in the calculation, divided by its estimated uncertainty.

$$S_{\text{lead-track}} = \frac{d_0}{\delta d_0} \quad (\text{A.4})$$

- Number of tracks in the isolation region ($N_{\text{track}}^{\text{iso}}$):
Number of tracks associated with the τ_{had} candidate in the region $0.2 < \Delta R < 0.4$.
- Maximum ΔR (ΔR_{Max}):
The maximum ΔR between the τ_{had} candidate and a track associated with it.
- Transverse flight path significance (S_T^{flight}):
The decay length of the secondary vertex in the transverse plane which is given by tau vertex associated algorithm, divided by its estimated uncertainty.

$$S_T^{\text{flight}} = \frac{\delta L_T^{\text{flight}}}{\delta L_T^{\text{flight}}} \quad (\text{A.5})$$

- Track mass (m_{track}):
Invariant mass of all tracks in the core and isolation regions.
- Track-plus- π^0 -system mass ($m_{\pi^0+\text{track}}$):
Invariant mass of the system on the tracks and π^0 mesons in the core region.
- Number of π^0 mesons (N_{π^0}):
The number of π^0 mesons reconstructed in the core region.
- Ratio of track-plus- π^0 -system p_T ($p_T^{\pi^0 + \text{track}}/p_T$):
Ratio of the p_T estimated using the track + π^0 information to the calorimeter-only measurement.

Appendix B

$t\bar{t}$ Contamination in Embedding Sample

The di-muon selections which is used for embedding sample are:

- $p_T^{\mu 1} > 20$ GeV, $p_T^{\mu 2} > 15$ GeV
- $|\eta^{\mu 1, \mu 2}| < 2.5$
- $m^{\mu 1, \mu 2} > 40$ GeV

But the contamination of other processes, in particular $t\bar{t}$, single top and diboson have potentially to be negligible contribution because of one or two b -tagged jets requirement of SR selections. This can lead the double counting of the event number. In order to estimate the contamination, the number of events which passes the embedding selections has been checked for $t\bar{t}$. The contribution in resonant mass and MMC in two b -tagged jets category is shown in Figure B.1. We found that $t\bar{t}$ is not negligible source, therefore we subtract this from embedding sample. 15% uncertainty, which is the uncertainty of $t\bar{t}$ normalization, is assigned for the subtraction. And the event yields on each selection levels in one and two b -tagged jets categories are shown in Table B.1 and B.2.

Table B.1: The event yields comparison on each selections of $t\bar{t}$ di-tau with $Z^0 \rightarrow \tau^+\tau^-$ in one b -tagged jet category.

Selection	$t\bar{t}$ (di-tau)	$Z^0 \rightarrow \tau^+\tau^-$
$m_T(l, \tau) < 60$	54.4 ± 2.9	8802.4 ± 72.9
OneB	43.9 ± 2.6	1472.9 ± 30.4
MET ϕ centrality > 1 .	20.4 ± 1.8	770.0 ± 22.2
Ellipse R > 1	20.3 ± 1.8	761.0 ± 22.1
$\Delta p_T < 20$ GeV	16.2 ± 1.6	601.0 ± 19.6
$90 < m_{jj} < 160$ GeV	4.0 ± 0.8	150.3 ± 9.6
High $p_T^{\tau^+\tau^-}$	1.2 ± 0.4	53.2 ± 5.6
$100 < m_{\tau^+\tau^-} < 150$ GeV	1.0 ± 0.4	43.1 ± 5.0

Table B.2: The event yields comparison on each selections of $t\bar{t}$ di-tau with $Z^0 \rightarrow \tau^+\tau^-$ in two b -tagged jets category.

Selection	$t\bar{t}$ (di-tau)	$Z^0 \rightarrow \tau^+\tau^-$
$m_T(l, \tau) < 60$	45.8 ± 2.7	305.4 ± 14.6
TwoB	45.1 ± 2.7	305.4 ± 14.6
MET ϕ centrality > 1 .	22.7 ± 1.9	151.2 ± 10.4
Ellipse R > 1	22.1 ± 1.9	146.8 ± 10.3
$\Delta p_T < 20$ GeV	18.0 ± 1.6	114.0 ± 8.8
$90 < m_{jj} < 160$ GeV	7.0 ± 1.1	33.0 ± 4.9
High $p_T^{\tau^+\tau^-}$	2.3 ± 0.6	8.4 ± 1.9
$100 < m_{\tau^+\tau^-} < 150$ GeV	2.1 ± 0.5	7.9 ± 1.9

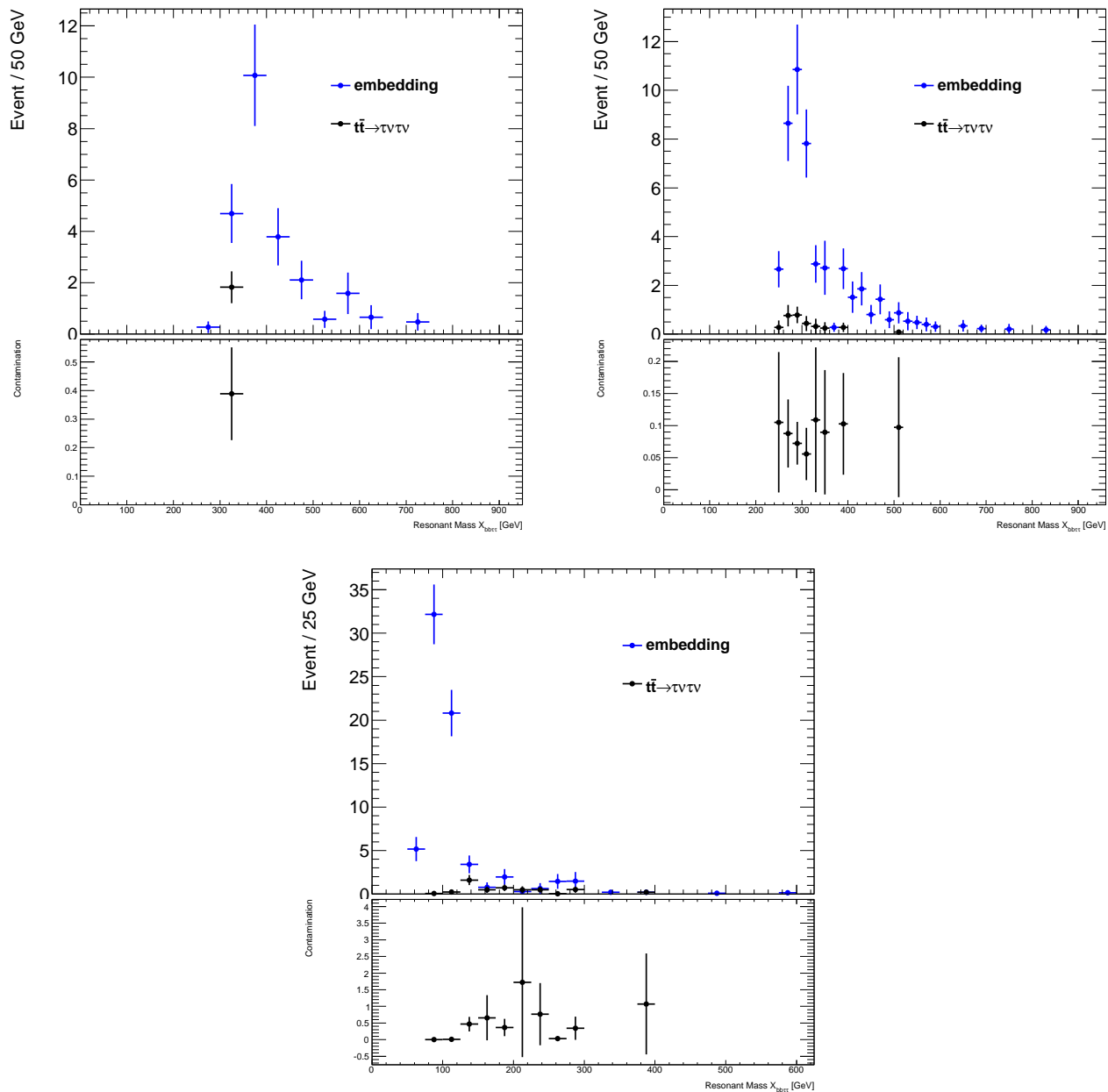


Figure B.1: Top two plots show embedding(blue) and $t\bar{t}$ contamination(black) in resonant mass distribution of two b-tagged jet category for resonant search. Bottom plot shows embedding(blue) and $t\bar{t}$ contamination(black) in MMC distribution of two b-tagged jet category for non-resonant search.

Appendix C

Other Analyses

C.1 $hh \rightarrow b\bar{b}\gamma\gamma$ analysis

The result of $hh \rightarrow b\bar{b}\gamma\gamma$ [68] is summarized in this section.

For the non-resonant search, the background is fitted with sum of a Crystal Ball function and a wide Gaussian component in the CR defined as fewer than two b tags region. The invariant mass distribution of diphoton is shown on Figure C.1 (a).

For the resonant search, the background is fitted with Landau in the CR defined as fewer than two b tags region. The invariant mass $m_{b\bar{b}\gamma\gamma}$ distribution is shown on Figure C.1 (b). The 95% CL upper limits for resonant production cross section times branching ratio is calculated as shown of Figure C.4.

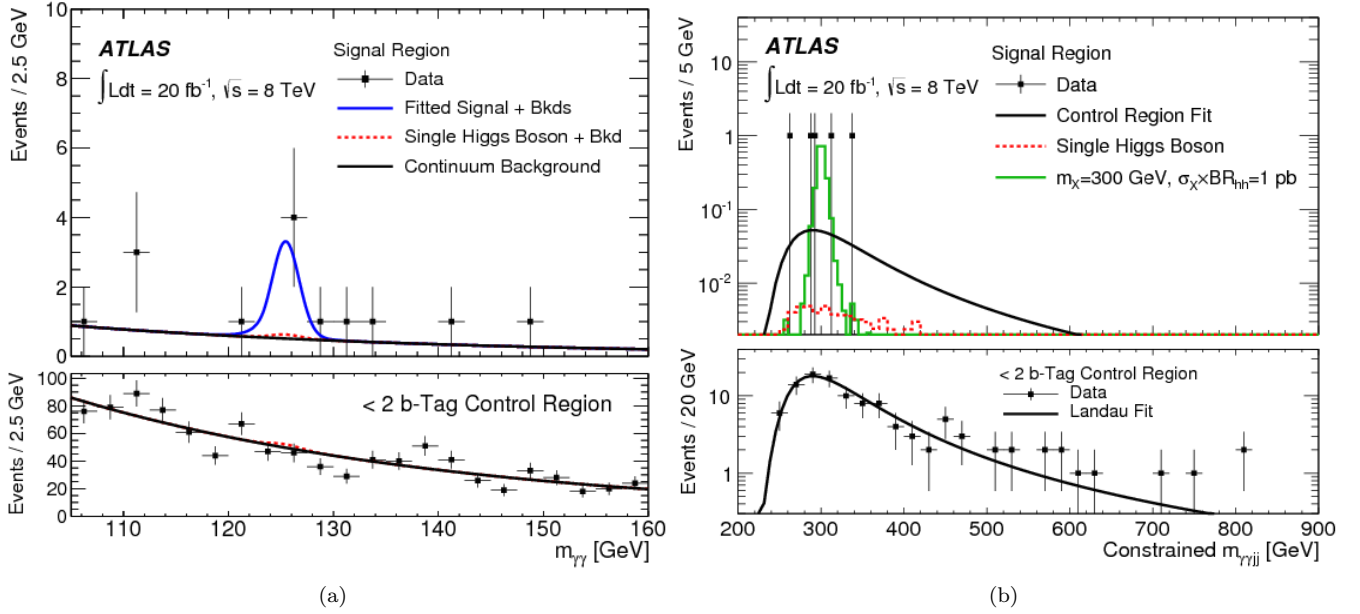


Figure C.1: Left: Invariant mass of diphoton $m_{\gamma\gamma}$ for non-resonant search (Upper) signal region, and (Lower) fewer than two b tags control region. The fitted curve is also used in the upper plot. Right: Invariant mass $m_{b\bar{b}\gamma\gamma}$ for resonant search (Upper) signal region, and (Lower) fewer than two b tags control region. The fitted curve is also used in the upper plot. [68].

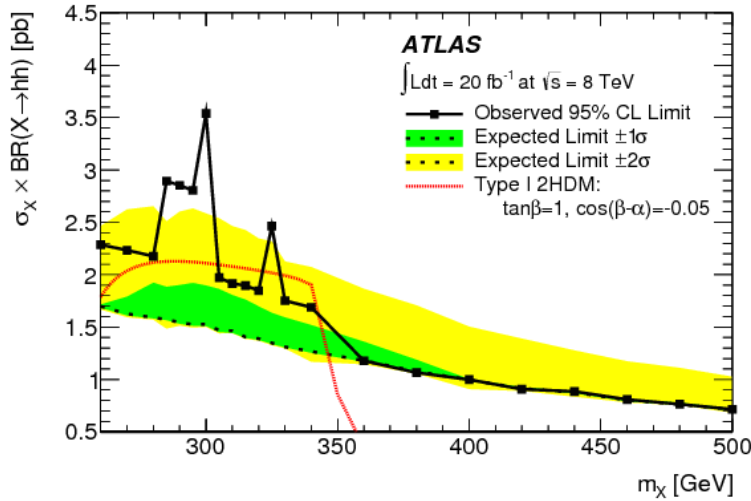


Figure C.2: The 95% CL upper limits for resonant production cross section times branching ratio of hh . [68]

C.2 $hh \rightarrow b\bar{b}b\bar{b}$ analysis

The result of $hh \rightarrow b\bar{b}b\bar{b}$ analysis [69] is summarized in this section. The event is required to have at least 4 b-tagged jets, and split into two analysis categories, Resolved or Boosted analysis.

Resolved analysis

Two dijet systems are chosen to satisfy ΔR between the jets in each of the dijets is smaller than 1.5. In the rare case that a jet could be used to create more than one dijet, the dijet with the highest mass is chosen. For the non-resonant search, invariant masses of two dijet system in 2D plane shown in Figure C.3 (a) is used. The surrounded region by inner back contour line is corresponding to the signal region. For the resonant search, invariant mass m_{4j} is used shown in Figure C.3 (b).

Boosted analysis

For the higher four jets mass, the higgs boson candidate is reconstructed as a single anti-Kt jet with large cone size $\Delta R = 1.0$. Here, it is called as “fat jet” and denoted by “J”. For the non-resonant search, invariant masses of two fat jets in 2D plane shown in Figure C.3 (c) is used. The surrounded region by inner back contour line is corresponding to the signal region. For the resonant search, invariant mass m_{2J} is used shown in Figure C.3 (d).

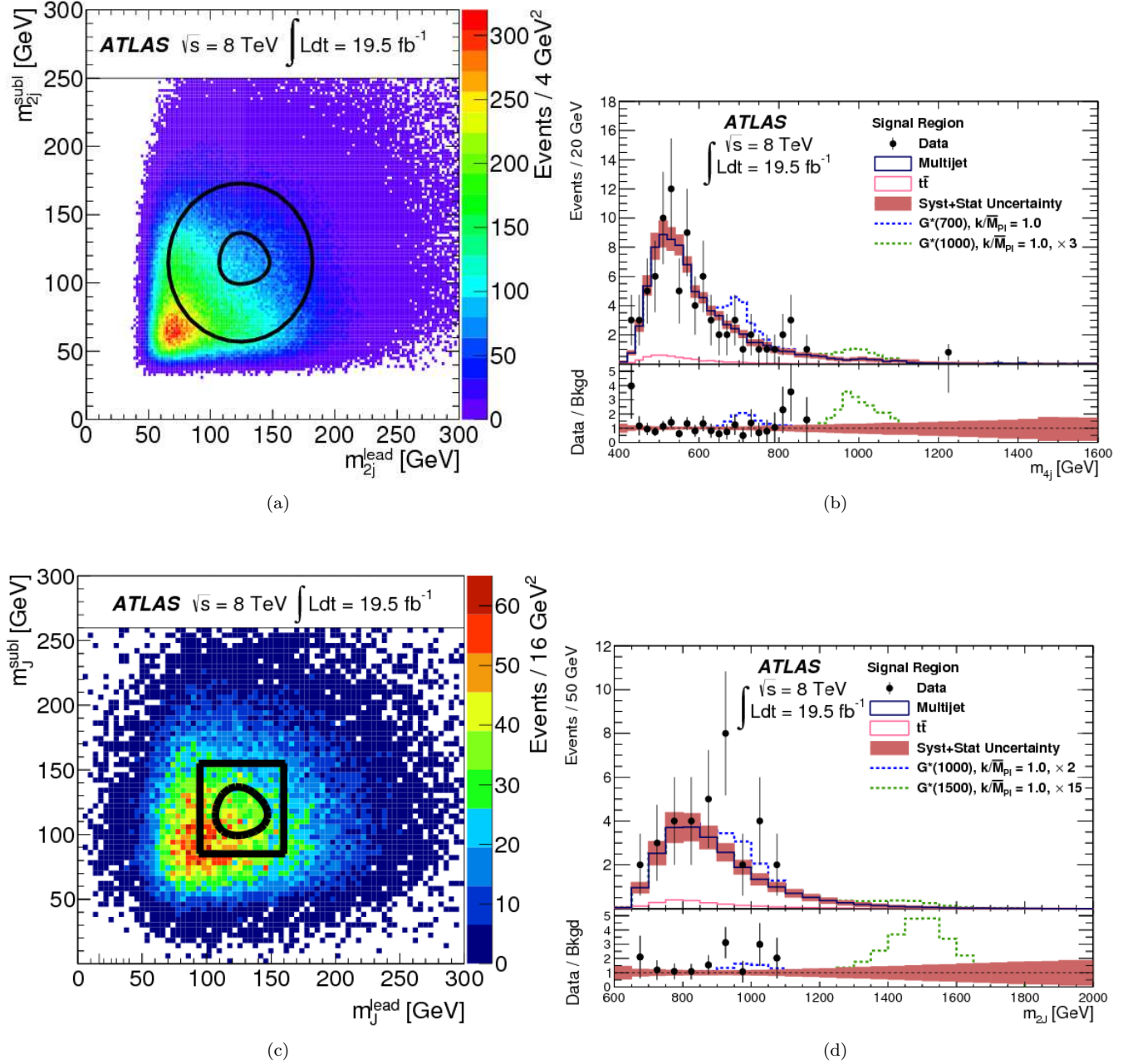


Figure C.3: Resolved analysis: Invariant masses of two dijet system in 2D plane (a), and four jets m_{4j} (b). Boosted analysis: Invariant masses of two fat jets in 2D plane (c), and two fat jets m_{2J} (d).

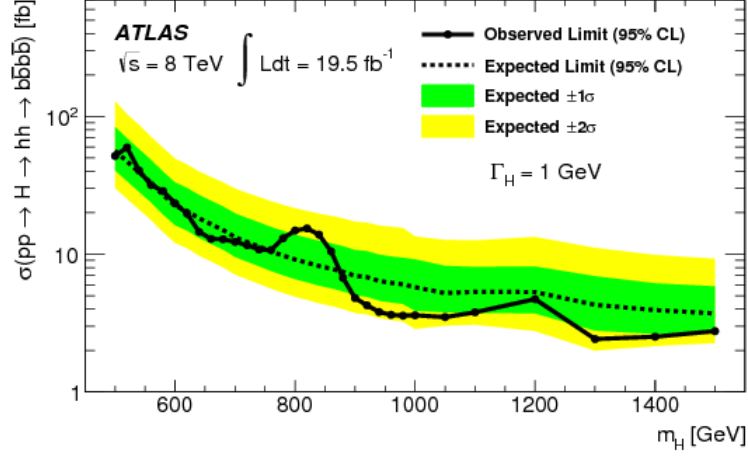


Figure C.4: The 95% CL upper limits for resonant production cross section times branching ratio of hh . [69]

C.3 $hh \rightarrow WW\gamma\gamma$ analysis

The result of $hh \rightarrow WW\gamma\gamma$ analysis [67] is summarized in this section. To suppress dijet background, one light lepton is required. Therefore $hh \rightarrow WW\gamma\gamma \rightarrow l\nu qq\gamma\gamma$ channel is analyzed. The invariant mass of diphoton is shown in Figure C.5. The result is derived to count the event yields in the signal region. The 95% CL upper limits for resonant production cross section times branching ratio is shown in Figure C.6

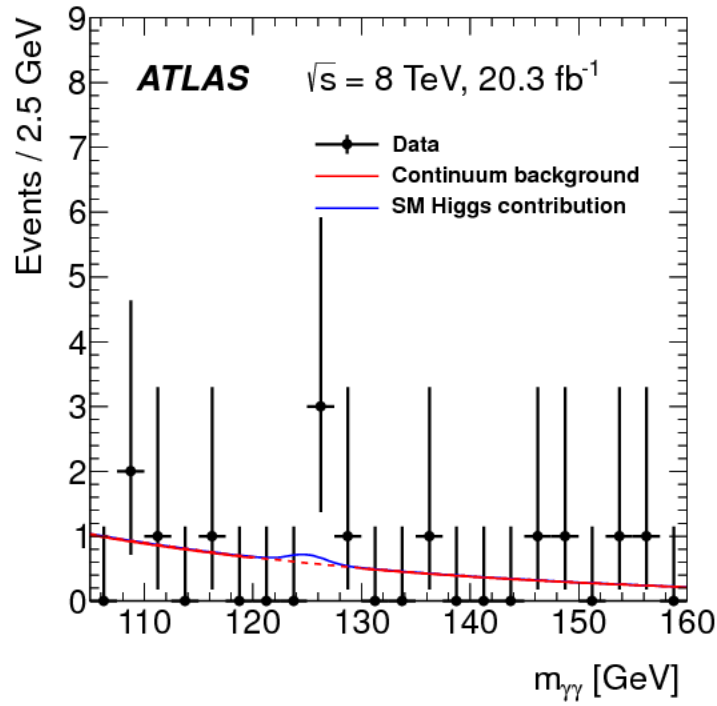


Figure C.5: The invariant mass of diphoton in the signal region. [67].

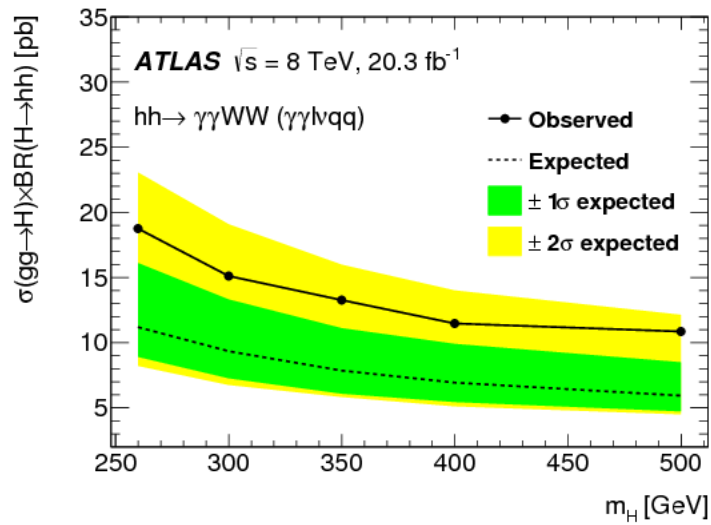


Figure C.6: The 95% CL upper limits for resonant production cross section times branching ratio of hh [67].

Bibliography

- [1] ATLAS Collaboration,
Observation of a new particle in the search for the standard model Higgs boson with the ATLAS detector at the LHC,
Phys. Lett. B 716 (2012) 129.
- [2] CMS Collaboration,
Observation of a new boson at a mass of 125 GeV with the CMS experiment at the LHC,
Phys. Lett. B 716 (2012) 30-61.
- [3] ATLAS Collaboration,
Measurement of the Higgs boson mass from the $H \rightarrow \gamma\gamma$ and $H \rightarrow ZZ^* \rightarrow 4l$ channels with the ATLAS detector using 25 fb^{-1} of pp collision data,
Phys. Rev. D90 (2014) 052004.
- [4] ATLAS Collaboration,
Evidence for the Higgs-boson Yukawa coupling to tau leptons with the ATLAS detector,
JHEP 1504 (2015) 117.
- [5] ATLAS Collaboration,
Measurements of the Higgs boson production and decay rates and coupling strengths using pp collision data at $\sqrt{s} = 7$ and 8 TeV in the ATLAS experiment,
ATLAS-CONF-2015-007.
- [6] ATLAS Collaboration,
Evidence for the spin-0 nature of the Higgs boson using ATLAS data,
Phys. Lett. B726 (2013) 120.
- [7] U. Baur, T. Plehn and D. L. Rainwater,
Determining the Higgs Boson Self Coupling at Hadron Colliders,
Phys. Rev. D67 (2003) 033003.
- [8] U. Baur, T. Plehn and D. L. Rainwater,
Probing the Higgs self-coupling at hadron colliders using rare decays,
Phys. Rev. D69 (2004) 053004.
- [9] M. J. Dolan, C. Englert and M. Spannowsky,
Higgs self-coupling measurements at the LHC,
JHEP 1210 (2012) 112.
- [10] J. Baglio et al.,
The measurement of the Higgs self-coupling at the LHC: theoretical status,
JHEP 1304 (2013) 151.
- [11] Lan-Chun Lu et al.,
Searching for Heavier Higgs Boson via Di-Higgs Production at LHC Run-2 (2015),
arXiv: 1507.02644 [hep-ph].

- [12] Baglio, J. and Djouadi, A. and Grober, R. and M. M. Uhrlleitner, and Quevillon, J. and other
The measurement of the Higgs self-coupling at the LHC: theoretical status,
JHEP 1304 (2013) 151.
- [13] R. Contino, M. Ghezzi, M. Moretti, G. Panico, F. Piccinini, et al.,
Anomalous Couplings in Double Higgs Production,
JHEP 1208 (2012) 154.
- [14] G. D. Kribs and A. Martin,
Enhanced di-Higgs Production through Light Colored Scalars,
Phys.Rev.D86 (2012) 095023.
- [15] Nathaniel Craig, Jamison Galloway, Scott Thomas,
Searching for Signs of the Second Higgs Doublet,
arXiv: 1305.2424 [hep-ph].
- [16] Y. Tang,
Implications of LHC Searches for Massive Graviton,
JHEP 1208 (2012) 078.
- [17] K. Cheung,
Phenomenology of radion in Randall-Sundrum scenario,
Phys.Rev. D63 (2001) 056007.
- [18] TE-EPC-LPC in LHC,
<http://te-epc-lpc.web.cern.ch/te-epc-lpc/machines/lhc/general.stm>
- [19] ATLAS EXPERIMENT Multimedia,
<http://www.atlas.ch/photos/index.html>.
- [20] Atlas Technical Paper List Of Figures,
<https://twiki.cern.ch/twiki/bin/view/AtlasPublic/AtlasTechnicalPaperListOfFigures>.
- [21] ATLAS Collaboration, G. Aad et al.,
The ATLAS Experiment at the CERN Large Hadron Collider,
JINST 3 (2008) S08003.
- [22] Yamamoto, A. et al.
Progress in ATLAS central solenoid magnet,
Nucl.Instrum.Meth. A584 (2008) 53-74.
- [23] J. Alwall et al.,
MadGraph 5: Going Beyond,
JHEP 1106 (2011) 128.
- [24] T. Plehn, M. Spira and P. Zerwas,
Pair production of neutral Higgs particles in gluon-gluon collisions,
Nucl. Phys. B479 (1996) 46.
- [25] R. Frederix et al.,
Higgs pair production at the LHC with NLO and parton-shower effects,
Phys. Lett. B732 (2014) 142.
- [26] B. Hespel and E. Vryonidou,
Higgs Pair Production,
url: <http://cp3.irmp.ucl.ac.be/projects/madgraph/wiki/HiggsPairProduction>.

-
- [27] M. Grazzini and H. Sargsyan,
Heavy-quark mass effects in Higgs boson production at the LHC,
JHEP 1309 (2013) 129.
- [28] D. de Florian et al.,
Higgs boson production at the LHC: transverse momentum resummation effects in the $H \rightarrow 2\gamma$, $H \rightarrow WW \rightarrow l\nu l'\nu'$ and $H \rightarrow ZZ \rightarrow 4l$ decay modes,
JHEP 1206 (2012) 132.
- [29] H.-L. Lai et al.,
New parton distributions for collider physics,
Phys. Rev. D82 (2010) 074024.
- [30] J. Pumplin et al.,
New Generation of Parton Distributions with Uncertainties from Global QCD Analysis,
JHEP 0207 (2002) 012.
- [31] ATLAS Collaboration,
Search for the Standard Model Higgs boson in the $H \rightarrow \tau\tau$ decay mode with 4.7 fb^{-1} of ATLAS data at 7 TeV,
ATLAS-CONF-2012-014.
- [32] K. Nagano,
Algorithms, performance, and development of the ATLAS High-level Trigger,
ATL-DAQ-PROC-2014-001. <http://cds.cern.ch/record/1643488>.
- [33] K. Nagano,
Algorithms, performance, and development of the ATLAS High-level Trigger,
ATLAS-DAQ-SLIDE-2013-893. <http://cds.cern.ch/record/1632445>.
- [34] ATLAS Collaboration,
Electron Performance measurements with the ATLAS detector using the 2010 LHC proton-proton collision data,
Eur. Phys. J.C72 (2012) 1909.
- [35] ATLAS Collaboration,
Improved electron reconstruction in ATLAS using the Gaussian Sum Filter-based model for bremsstrahlung,
ATLAS-CONF-2012-047.
- [36] R. Fruehwirth,
Application of Kalman filtering to track and vertex fitting,
Nucl.Instrum. Meth. (1987) 444-450.
- [37] ATLAS Collaboration, Electron reconstruction and identification efficiency measurements with the ATLAS detector using the 2011 LHC proton-proton collision data, Eur. Phys. J.C74 (2014) 2941.
- [38] ATLAS Collaboration,
Electron efficiency measurements with the ATLAS detector using the 2012 LHC proton-proton collision data,
ATLAS-CONF-2014-032.
- [39] ATLAS Collaboration,
Global Sequential Calibration (GSC) at ATLAS,
Eur. Phys. J. C74 (2014) 3071.

- [40] ATLAS Collaboration,
Stefanos Leontsinis, Performance of the muon identification and reconstruction with the ATLAS detector,
EPJ Web Conf. 95 (2015) 05009.
- [41] ATLAS Collaboration,
Measurement of the muon reconstruction performance of the ATLAS detector using 2011 and 2012 LHC protonproton collision data,
Eur. Phys. J. C74 (2014) 3130.
- [42] ATLAS Collaboration,
Identification and energy calibration of hadronically decaying tau leptons with the ATLAS experiment in pp collisions at $\sqrt{s}=8$ TeV,
Eur. Phys. J. C75 (2015) 303.
- [43] ATLAS Collaboration,
Jet energy measurement with the ATLAS detector in proton-proton collisions at $\sqrt{s} = 7$ TeV,
Eur. Phys. J. C73 (2013) 2304.
- [44] M. Cacciari, G. P. Salam, and G. Soyez,
The anti-kt jet clustering algorithm,
JHEP 04 (2008) 063.
- [45] M. Cacciari, G. P. Salam, and G. Soyez,
FastJet user manual,
Eur. Phys. J. C 72 (2012) 1896.
- [46] ATLAS Collaboration,
Monte Carlo Calibration and Combination of In-situ Measurements of Jet Energy Scale, Jet Energy Resolution and Jet Mass in ATLAS,
ATLAS-CONF-2015-037.
- [47] ATLAS Collaboration,
Jet energy measurement and its systematic uncertainty in proton-proton collisions at $\sqrt{s} = 7$ TeV with the ATLAS detector,
Eur. Phys. J., C75 (2015) 17.
- [48] ATLAS Collaboration,
ATLAS Collaboration, Jet global sequential corrections with the ATLAS detector in proton-proton collisions at $\sqrt{s} = 8$ TeV,
ATLAS-CONF-2015-002.
- [49] ATLAS Collaboration,
Data-driven determination of the energy scale and resolution of jets reconstructed in the ATLAS calorimeters using dijet and multijet events at $\sqrt{s}=8$ TeV,
ATLAS-CONF-2015-017.
- [50] ATLAS Collaboration,
Calibration of the performance of b-tagging for c and light-flavour jets in the 2012 ATLAS data,
ATLAS-CONF-2014-046.
- [51] ATLAS Collaboration,
Calibration of b-tagging using dileptonic top pair events in a combinatorial likelihood approach with the ATLAS experiment
ATLAS-CONF-2014-004.

-
- [52] ATLAS Collaboration
Performance of Impact Parameter-Based b-tagging Algorithms with the ATLAS Detector using Proton-Proton Collisions at $\sqrt{s} = 7$ TeV
ATLASCONF-2010-091.
- [53] ATLAS Collaboration,
Performance of the ATLAS Secondary Vertex b-tagging Algorithm in 7 TeV Collision Data,
ATLAS-CONF-2010-042.
- [54] ATLAS Collaboration,
Expected Performance of ATLAS Detector, Trigger and Physics,
CERN-OPEN-2008-020.
- [55] G. Piacquadio and C. Weiser,
A new inclusive secondary vertex algorithm for b-jet tagging in ATLAS,
J.Phys.Conf.Ser. 119 (2008) 032032.
- [56] A. Elagin, P. Murat, A. Pranko, and A. Safonov,
A New Mass Reconstruction Technique for Resonances Decaying to di-tau,
Nucl.Instrum.Meth. A654 (2011) 481-489.
- [57] ATLAS Collaboration,
Presentation in Jet/MET working group,
<https://indico.cern.ch/getFile.py/access?contribId=0&resId=0&materialId=slides&confId=16124>.
- [58] ATLAS Collaboration, G. Aad et al.,
The ATLAS Experiment at the CERN Large Hadron Collider,
JINST 3 (2008) S08003.
- [59] ATLAS Collaboration, G. Aad et al.,
Performance of the ATLAS muon trigger in pp collisions at $\sqrt{s}=8$ TeV,
Eur. Phys. J. C75 (2015) 120.
- [60] ATLAS Collaboration,
Data-Quality Requirements and Event Cleaning for Jets and Missing Transverse Energy Reconst ruction with the ATLAS Detector in Proton-Proton Collisions at a Center-of-Mass Energy of $\sqrt{s} = 7$ TeV,
ATLAS-CONF-2010-038.
- [61] ATLAS Collaboration,
Search for the Standard Model Higgs boson in $H \rightarrow \tau\tau$ decays in proton-proton collisions with the ATLAS detector,
ATLAS-CONF-2012-160.
- [62] ATLAS and CMS Collaboration,
Combined Standard Model Higgs boson searches with up to 2.3 fb^{-1} of pp collisions at $\sqrt{s}=7$ TeV at the LHC,
ATLAS-CONF-2011-157.
- [63] I. W. Stewart and F. J. Tackmann,
Theory Uncertainties for Higgs and Other Searches Using Jet Bins,
Phys. Rev. D85 (2012) 034011.

- [64] ATLAS Collaboration,
Determination of the tau energy scale and the associated systematic uncertainty in proton-proton collisions at $\sqrt{s} = 8$ TeV with the ATLAS detector at the LHC in 2012, ATLAS-CONF-2013-044.
- [65] E. G. G. Cowan, K. Cranmer and O. Vitells,
Asymptotic formulae for likelihood-based tests of new physics,
Eur. Phys. J. C73 (2013) 2501
- [66] D. de Florian and J. Mazzitelli,
Higgs Boson Pair Production at Next-to-Next-to-Leading Order in QCD,
Phys. Rev. Lett. 111 (2013) 201801.
- [67] ATLAS Collaboration,
Searches for Higgs boson pair production in the $hh \rightarrow bb\tau\tau, \gamma\gamma WW^*, \gamma\gamma bb, bbbb$ channels with the ATLAS detector,
Phys. Rev. D 92, (2015) 092004.
- [68] ATLAS Collaboration,
Search for Higgs Boson Pair Production in the $\gamma\gamma b\bar{b}$ Final State Using pp Collision Data at $\sqrt{s} = 8$ TeV from the ATLAS Detector
Phys. Rev. Lett. 114 (2015) 081802.
- [69] ATLAS Collaboration,
Search for Higgs boson pair production in the $b\bar{b}b\bar{b}$ final state from pp collisions at $\sqrt{s} = 8$ TeV with the ATLAS detector
Eur. Phys. J. C75 (2015) 412.
- [70] A. Djouadi et al.,
The post-Higgs MSSM scenario: habemus MSSM?,
Eur. Phys. J. C73 (2013) 2650.
- [71] A. Djouadi et al.,
Fully covering the MSSM Higgs sector at the LHC,
JHEP 06 (2015) 168.
- [72] A. Djouadi et al.,
Fully covering the MSSM Higgs sector at the LHC,
JHEP 06 (2015) 168.
- [73] ATLAS Collaboration,
Performance of the ATLAS Secondary Vertex b-tagging Algorithm in 7 TeV Collision Data, ATLAS-CONF-2010-042.